



**HAL**  
open science

# Understanding thermal transport in advanced nanophononic structures for energy applications

Mohammad Hadi

► **To cite this version:**

Mohammad Hadi. Understanding thermal transport in advanced nanophononic structures for energy applications. Physics [physics]. Université de Lyon, 2022. English. NNT : 2022LYSE1045 . tel-04544733

**HAL Id: tel-04544733**

**<https://theses.hal.science/tel-04544733>**

Submitted on 13 Apr 2024

**HAL** is a multi-disciplinary open access archive for the deposit and dissemination of scientific research documents, whether they are published or not. The documents may come from teaching and research institutions in France or abroad, or from public or private research centers.

L'archive ouverte pluridisciplinaire **HAL**, est destinée au dépôt et à la diffusion de documents scientifiques de niveau recherche, publiés ou non, émanant des établissements d'enseignement et de recherche français ou étrangers, des laboratoires publics ou privés.



Université Claude Bernard



Lyon 1

N° d'ordre NNT : 2022LYSE1045

**THÈSE de DOCTORAT DE L'UNIVERSITÉ DE LYON**

Opérée au sein de :

**l'Université Claude Bernard Lyon 1**

**Ecole Doctorale ED 34**  
Matériaux

**Spécialité de doctorat : Physique de la matière condensée**

**Discipline : Physique**

Soutenue publiquement le 14/03/2022, par :

**Mohammad Hadi**

---

**Understanding Thermal Transport in  
Advanced Nanophononic Structures for  
Energy Applications**

---

Devant le jury composé de :

**BOURGEOIS Olivier**

Directeur de Recherche CNRS , INP, Institut Néel

**ZARDO Ilaria**

Professeur, Département de Physique, Université de Basel

**BENCIVENGA Filippo**

Chercheur, FERMI FEL, Elettra-Sincrotrone Trieste S.C.p.A.

**DEL FATTI Natalia**

Professeur, Institut Lumière Matière, Université Lyon 1

**PAILHÈS Stéphane**

Chargé de Recherche CNRS, Institut Lumière Matière, CNRS

**GIORDANO Valentina**

Chargé de Recherche CNRS, Institut Lumière Matière, CNRS

**Rapporteur**

**Rapporteuse**

**Examineur**

**Présidente**

**Directeur de thèse**

**Co-Directrice de thèse**

# Abstract

## Understanding Thermal Transport in Advanced Nanophononic Structures for Energy Applications

The hazardous effects of pollution have many aspects such as health effects and environmental changes. The main source of pollution is the emission of toxic gases from energy sources like fuel and coal [1]. Numerous fields of research attempt to tackle the addressed problems. We are here interested in photocatalysis as a promising way for producing a green source of energy [2]. In this thesis, we investigate the concept of nanostructured materials for the optimisation of thermal energy distribution in order to thermally boost the photo-induced processes. This process, taking place at the interface between optics (photons) and thermics (phonons), belongs to the field of phoxonics. To this aim, in the framework of an "Idex Lyon Breakthrough" project called IPPON, "Incoherent light and Phonon management in micro-nanopatterned materials for efficient depollution and artificial Photocatalysis", we have investigated thermal transport in nanostructured amorphous SiN thin films, by means of pump-probe techniques to measure thermal conductivity and understand the microscopic mechanisms below thermal transport in such materials.

As a first research axis, we report the study of the effect of the temperature deposition on the thermal conductivity in amorphous SiN<sub>x</sub> films of thicknesses between 200 and 500 nm, as measured by the thermoreflectance technique with temperatures up to 773 K. Surprisingly, for all deposition temperatures between 300 and 573 K, thermal conductivity exhibits a steep decrease above 473 K, decreasing by more than 30% down to a minimum around 673 K, before increasing back to values comparable with the room temperature one. This behavior, observed only for a first heating of the sample, is associated to an irreversible modification of the thin film, and may be related to a partial desorption of the hydrogen trapped in a-SiN<sub>x</sub> during the deposition. A second research axis has been to investigate directly the quasiparticle responsible for heat transport, the phonon, in order to understand the effect of nanostructuration on its individual properties (energy and lifetime). The study shows that the reduction of the phonon lifetime in the nanostructured material as compared to the uniform ma-

terial can be ascribed to the increase of the phonon scattering from the interfaces. Our work shows that the phonon lifetime reduction strongly depends on phonon wavelength, as related to the typical nanostructure lengthscale. As such, depending on phonon wavelength, the ratio between the lifetime in the nanostructured material and the uniform one ranges between 10 to 60%.

# Résumé

## Comprendre le transport thermique dans des structures nano-phoniques pour des applications dans le domaine de l'Energie

La réduction de la pollution est un des grands défis de notre siècle pour notre société et pour l'environnement. La principale source de pollution est l'émission de substances toxiques gazeuses provenant de sources d'énergie fossiles [1]. Les procédés photocatalytiques offrent des solutions alternatives pour la dépollution, le stockage et la production d'énergie en minimisant l'empreinte écologique [2]. Dans cette thèse, nous étudions l'intérêt de la nanostructuration de la matière pour optimiser l'activation thermique des processus photo-induits. Cette nanostructuration étant déjà optimisée pour les processus photoniques, l'objectif est de concevoir la nano-structure à l'interface entre l'optique (photons) et la thermique (phonons), on parle alors de phoxonique. Pour cela, dans le cadre d'un projet "IDEXLYON Scientific Breakthrough" nommé "IPPON:Incoherent light and Phonon management in micro-nanopatterned materials for efficient depollution and artificial PhOtosyNthesis.", nous avons travaillé sur l'étude de la thermique dans des substrats de SiN nano-structurés via des approches pompe-sonde pour mesurer la conductivité thermique et comprendre les mécanismes microscopiques de transport de la chaleur.

Le premier axe du travail de thèse a été l'étude de l'effet de la température de dépôt sur la dépendance en température de la conductivité thermique de films de SiN<sub>x</sub> amorphe d'épaisseurs comprises entre 200 et 500 nm. Étonnamment, la conductivité thermique présente une forte diminution en chauffant au-dessus de 473 K, diminuant de plus de 30% jusqu'à un minimum autour de 673 K, avant de retrouver des valeurs comparables à la température ambiante. Ce comportement, observé uniquement pour un premier cycle de chauffage de l'échantillon, est associé à une modification irréversible du film mince, et a été relié à une désorption partielle de l'hydrogène piégé dans a-SiN<sub>x</sub> lors du dépôt. Le second axe du travail est dédié à l'étude microscopique de la propagation des particules élémentaires du transport thermique, les phonons, dans les membranes de SiNx amorphe nanostructurées. L'objectif est d'étudier l'effet de la nano-structuration sur la propagation des phonons en fonction de leurs propriétés individuelles (longueur d'onde

et énergie). L'étude montre que la réduction de la durée de vie des phonons dans le matériau nanostructuré dépend fortement de la longueur d'onde des phonons au regard des dimensions caractéristiques de la nanostructure. Ainsi, le rapport des durées de vie des phonons entre le matériau nanostructuré et le matériau uniforme varie de 10 à 60% en fonction de la longueur d'onde.

# Contents

<b>Abstract</b>	<b>ii</b>
<b>Résumé</b>	<b>iv</b>
<b>1 Introduction</b>	<b>1</b>
1.1 Phononics and Photonics (Phoxonics)	2
1.1.1 Phonons Overview	2
1.1.2 Phoxonics: Basics	3
1.1.3 Nanostructuring in Photocatalytic System	4
1.2 Phonons in Nanostructured Materials	5
1.2.1 Nanocomposite Materials for Thermal Management	6
1.2.2 The Effect of Size Reduction: Guided Waves in Thin Film and Membranes	11
1.2.3 Phonons in Phononic Crystals	16
<b>2 Experimental Methods</b>	<b>19</b>
2.1 Thin Film Laser Flash Technique	19
2.1.1 Technique Principle Description	19
2.1.2 Experimental Apparatus	20
2.1.3 Model of The Experiment	26
2.2 Extreme Ultraviolet Transient Grating Spectroscopy	30
2.2.1 Overview about Transient Grating	30
2.2.2 Timer Beamline	32
<b>3 Silicon Nitride (IPPON)</b>	<b>37</b>
3.1 Samples	38
3.2 Thermal Study of Amorphous Silicon Nitride thin films	38
3.2.1 Effect of the Annealing Temperature on the Physical Properties of $\text{SiN}_x$	39
3.2.2 Room Temperature Measurement	40
3.2.3 High Temperature Measurement	42
3.2.4 Low Temperature Measurement	50

<b>4</b>	<b>Phonon Dynamics in Amorphous Silicon Nitride</b>	<b>53</b>
4.1	Samples . . . . .	53
4.2	Phonon Dynamics in a Homogeneous Amorphous SiN <sub>x</sub> Thin Film	54
4.2.1	PECVD SiN <sub>x</sub> in Reflection Geometry . . . . .	54
4.2.2	Suspended LPCVD SiN <sub>x</sub> Membranes . . . . .	55
4.2.3	Analysis . . . . .	66
4.3	Phonon Dynamics in Nanostructured Material . . . . .	70
4.3.1	Phonon Wavelength at 55 nm . . . . .	71
4.3.2	Phonon Wavelength at 84 nm . . . . .	74
4.3.3	Phonon Wavelength at 106 nm . . . . .	77
4.3.4	Analysis . . . . .	80
<b>5</b>	<b>Conclusions and Perspectives</b>	<b>84</b>
<b>A</b>	<b>Background Image Code</b>	<b>86</b>
	<b>Bibliography</b>	<b>89</b>

# Chapter 1

## Introduction

Pollution is the most important issue facing our planet as it has serious effects on many aspects such as health and environment. The main cause of pollution is using sources of energy like fuel and coal for cars and power plants since they emit toxic gases when burning such as carbon dioxide [1]. These toxic gases have hazardous effects on the environment that lead to climate change, temperature rise, floods due to ice melting in the poles, desertification, and health problems, etc [3,4]. Green sources of energy are essential to decrease pollution, a reason for which research on this topic has become quite active. In an attempt to solve this problem, a lot of research has been focused on photocatalysis. In addition, this is an environmentally friendly process as it can take place using solar light, however it has a low efficiency since only 4-5% of the UV range (below 400nm) is actually used [5-7]. It is a process where light can activate a semiconductor and allow it to become a catalyst in a reaction. An advantage of this process is that it can be performed at room temperature, and requires no oxidative agent other than the air oxygen to totally mineralize pollution. Photocatalysis is presented as a promising way in producing a green source of energy [5]. Photocatalytic systems appear as promising for reducing air [7] and water [8] pollution. Titanium Oxide ( $\text{TiO}_2$ ) as a low cost material appeared as a promising semiconductor material for Photocatalysis due to stability after catalytic cycles, and most active for photon excitation energies in the UV range [2]. The main challenge of this system is to increase its efficiency which can be accomplished by the nanostructuring of the material [9]. The idea of the nanostructuring is evaluated as the ability to focus the electromagnetic field in order to enhance the photocatalytic efficiency [10,11]. Still, nanostructuring also has a role in determining thermal transport, which, on its turn, can affect catalysis efficiency. The photo-catalysis reactions mostly depends on the Arrhenius law, i.e. strongly on the temperature [12]. As such, a promising way would be to design micro and nanostructured materials which lead to trapping and confinement of incoherent light. The nanostructured materials is expected to enhance local temperature rise through phonon confinement which leads to improve the yield of the photocatalysis. Studying phonon dynamics [13]

in nanostructured material is fundamental to understand the thermal transport and possibly simultaneously optimize light trapping, local optical amplification, and the thermal trap to boost the photocatalysis efficiency. We focus on the study of thermal transport in nanostructured materials which can be used in catalysis devices, but will turn out to be useful for other, more thermal management related, applications.

The key parameter for understanding thermal management in materials is the thermal conductivity of the material. The total thermal conductivity is the summation of two parts: the electronic,  $\kappa_{electron}$ , proportional to the electrical conductivity, and the phononic,  $\kappa_{phonon}$ , related to atomic vibrations [14]. In this thesis work, as the material of study is insulating, we are concerned only with the phononic contribution. We will investigate the heat carriers, the phonons, for understanding the macroscopic thermal transport properties in nanocomposites for photocatalysis application.

This PhD is a part of a research line which aims to implement in the conception of these nanostructures the optimisation of the thermal energy distribution in order to thermally boost the photo-induced processes. This new concept is at the basis of the new field of research at the interface between optics and thermics making the elementary particles of light, the photons, and heat, the phonons, meet which defines the phoxonics. This concept is at the core of a collaborative project, "Incoherent light and Phonon management in micro-nanopatterned materials for efficient depollution and artificial PhOtosyNthesis" (IPPON), funded by IDEX Lyon. The introduction is divided into the following sections,

-Section (1.1): Description of phonons and photons properties related to the IPPON project

-Section (1.2): Phonon in nanostructured materials

## 1.1 Phononics and Photonics (Phoxonics)

### 1.1.1 Phonons Overview

The lattice vibrations of a solid are represented by phonons. A phonon is a plane wave that has a wavevector,  $\mathbf{k}$ , a vibrational frequency,  $\omega(\mathbf{k})$ , and a polarization, which can be either longitudinal ( $\vec{e}_L$ ) or transverse ( $\vec{e}_T$ ) depending if the atoms' vibration direction is parallel or perpendicular to the wave propagation [15]. The relation that covers the variation of the phonon frequency vs. wavevector is called the phonon dispersion relation. It contains two kinds of phonons: acoustic and optic. The acoustic and optical branches are characterized by zero frequency and finite frequency at zero wave vector, respectively. The motion of the phonon in the material is affected by different properties in the material which can scatter the phonon. There are several sources of phonon scattering such as phonon-phonon scattering (non-resistive normal and resistive

Umklapp processes), electron-phonon scattering, scattering from point defects, from grain boundaries and from interfaces [16]. Understanding the scattering mechanisms in the material gives a deep understanding about different properties of the material such as the thermal conductivity.

### 1.1.2 Phoxonics: Basics

Photoelastic (PE) and moving interface (MI) effects are the two mechanisms for photon-phonon interaction. In both of these effects, a local variation of the dielectric permittivity induced by the present acoustic strain is the reason for this interaction. However, PE effects are due to photoelastic parameters (Pockels effect [17]) at the level of the bulk of each material, while MI effects are due to the motion of interfaces during acoustic vibrations and thus take place at the level of boundaries of two materials [18,19]. Perturbation theory is the first method used to calculate the OM (OptoMechanic) strength interaction [20]. The total OM coupling rate is the summation of the photoelastic and moving interface rates [21,22]. Historically, at the beginning, phoxonics was developed for optomechanic applications. Given that the frequency of the phonon is several orders of magnitude below the photon frequency, the frequency of the photonic mode is calculated at successive instants of an acoustic period assuming the acoustic mode strain profile is frozen at these times.

In the IPPON project, the main aim is to optimize both photon and phonon through the same nanostructuration. The IPPON sample is a thin film with periodic nanostructuration with different periodicity deposited on a substrate with low refractive index as shown in figures (1.1.a) and (1.1.b). We expect a localization of the light in the pores based on the simulation of the electric field in the nanostructure, as shown in figure (1.1.c), which shows trapping of light inside the holes which increases the collected current in the visible range spectrum. On the other hand, photons have wave-vectors much smaller than thermal phonons (the ones which dominate the heat transport at room temperature). Thermal phonons have short wavelengths but they propagate their energies over long distances. Such distance is called the mean free path: the travelled distance between two scattering events. Through nanostructuration, the mean free path can be reduced, thus impacting not only photons but also phonons. The expected impact depends on phonon wavelength with respect to the nanostructure lengthscale, as has been investigated in Luo et al. [13]. In particular this Finite Element Modeling study on a 2D nanostructured material reports a possible localization of the vibrational energy between pores depending on phonon wavelength, as shown in figure (1.1.d). Such localization could lead to a local temperature enhancement and thus have a beneficial effect on photocatalysis. The main objective of the IPPON project is to design micro-nanostructures that enhance the local temperature increase through phonon confinement, and the trapping of the incoherent light.

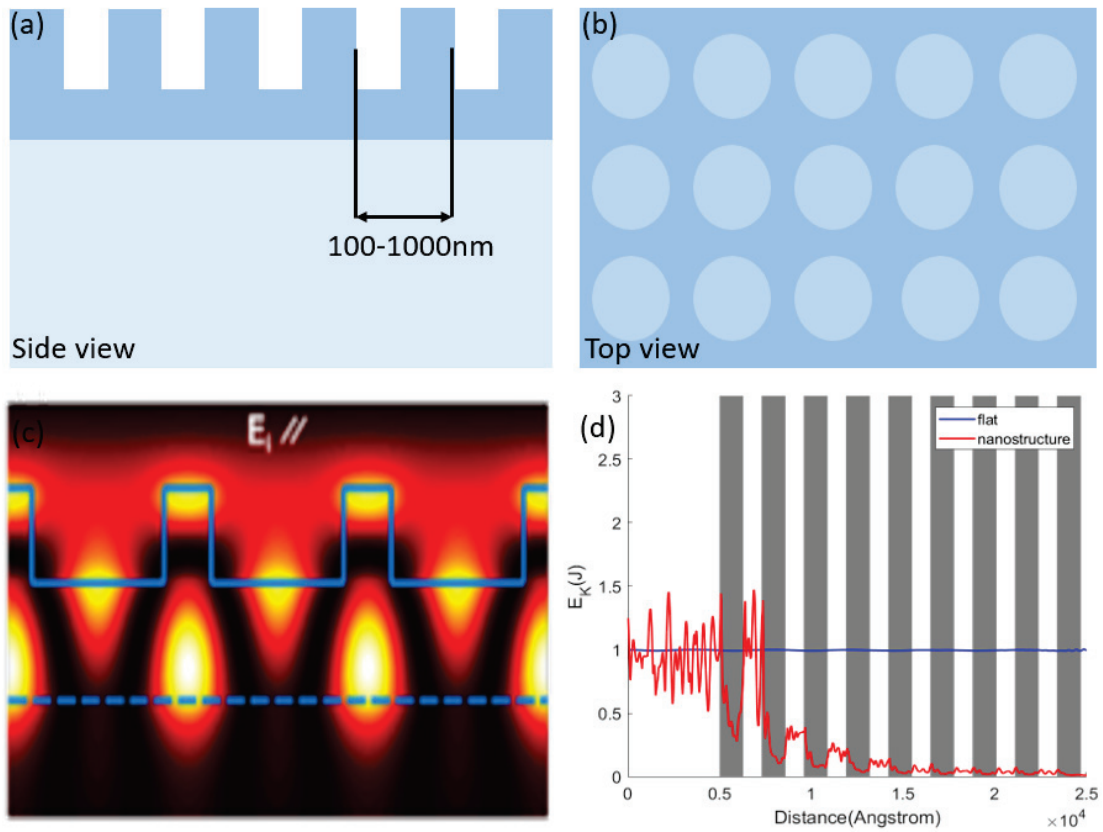


**Figure 1.1:** a) Side view of the IPPON nanostructuring system on a sample with low refractive index. b) Top view of the IPPON nanostructuring system, the change of color in the hole zone is just for clarification. c) Simulation of the electric field distribution for the IPPON nanostructure. d) FEM modeling of the propagation of a phonon wave packet with wavelength 100 nm in a uniform (blue) and nanostructured (red) sample (Grey regions correspond to the pores positions) done by Haoming LUO.

### 1.1.3 Nanostructuring in Photocatalytic System

Micro-nanophotonics that include photonic crystals or metasurfaces provide control of light-matter interaction like ultra-low laser emission or giant optical nonlinearities. It operates based on patterns with feature size that ranges from 100 nm to 1  $\mu\text{m}$  [11]. Combining optical media and micro-nanophotonic structures has been achieved recently for non coherent light (solar light) as compared to previous coherent light (lasers). An example of this application is achieved by increasing the photon path by a factor of 10 in the red and infrared and consequently increasing the current by 50 % due to light trapping in solar cells [23, 24]. The main challenge currently faced is to fabricate large area micro/nanopatterns with the simultaneous optimization of optical, thermal and charge transfer properties [25].

The activation energies of active media being used in photocatalysis span over one order of magnitude only. Since a higher yield in photocatalysis for a specific light intensity requires a lower activation energy of the media used, and the activation energy implies a strong temperature dependence on the photocatalysis efficiency, then a local increase of the temperature would present a solution to allow for an increased yield despite a significant part of light being lost in the local heating process. This yield could depend exponentially rather than linearly on the light intensity in the case of Hydrogen production for an example.

Nanostructuring could be a method to obtain this [26,27]. Molecular dynamics simulations show a decrease in the thermal conductivity (by orders of magnitude) of nanoporous phononic silicon with a periodic organization. These simulations predict a localization of high energy phonons in the space between the pores while a phononic band gap exists in the GHz frequency range for a nanophononic crystals with typical dimensions comparable to the ones foreseen. In this project, more recent simulations show evidence filtering of high energy phonons in the THz range in nanophononic systems [28]. The ultimate goal is to understand the effect of the nanostructuring on phonon dynamics in order to identify the best nanostructure able to combine the optimization of light trapping, local optical amplification, and the thermal trap for dramatically enhancing the photocatalysis efficiency.

## 1.2 Phonons in Nanostructured Materials

The lattice thermal conductivity is expressed by integrating in energy the spectral phononic thermal conductivity [16,29],

$$\kappa_{phonon}(T) = \frac{1}{3} \int_0^{\omega_{max}} C_v(\omega, T) v_g^2(\omega, T) \tau(\omega, T) g(\omega, T) d\omega \quad (1.1)$$

Where  $C_v$  is the phonon specific heat,  $v_g$  is the phonon group velocity,  $\tau$  is the phonon lifetime,  $g$  is the phonon density of states (DOS), and  $\omega$  is the vibrational frequency. The group velocity is defined as  $v_g(\omega) = \frac{\partial \omega}{\partial k}$ , which means it is the local slope of the dispersion relation,  $\omega(k)$ . Phonon specific heat and phonon group velocity can be calculated from the phonon's  $\omega(k)$ . Phonon mean free path is the distance traveled by the phonon before being scattered, and the travel time needed before scattering is the phonon lifetime. The phonon lifetime is accessible by measuring the phonon attenuation,  $\Gamma$ , ( $\Gamma = 2\hbar/\tau$ ) [30,31]. As previously mentioned, several are the source of scattering for phonons such as phonon-phonon scattering (Normal and Umklapp process), grain boundary scattering, impurity scattering, and boundary scattering, which may reduce the phonon lifetime. A characteristic lifetime ( $\tau_i$ ) is associated to each scattering process, which generally depends on phonon energy and possibly on the temperature. The total phonon lifetime is given by Matthiessen's rule as,

$$\tau_{total}^{-1} = \sum_i \tau_i^{-1} \quad (1.2)$$

Where  $i$  passes through the different scattering processes appearing in the system.

### 1.2.1 Nanocomposite Materials for Thermal Management

When a material of nanometric size is embedded inside a material of different type, we are in front of a nanocomposites material. This type of materials introduce phonon scattering at the interfaces between the two materials at the nanoscale with its typical lifetime and thus phonon mean free path. Nanocomposite materials have attracted recent studies because they exhibit a strong reduction or enhancement of the thermal conductivity depending on the bulk materials composing them [32, 33]. One example is reported in figure (1.2), where thermal conductivity of a nanocomposite made of hexagonal nanometer boron nitride(nBN), embedded in PolyPhenylene Sulfide(PPS), is reported as a function of percentage mass fraction of nBN/PPS system [34, 35].

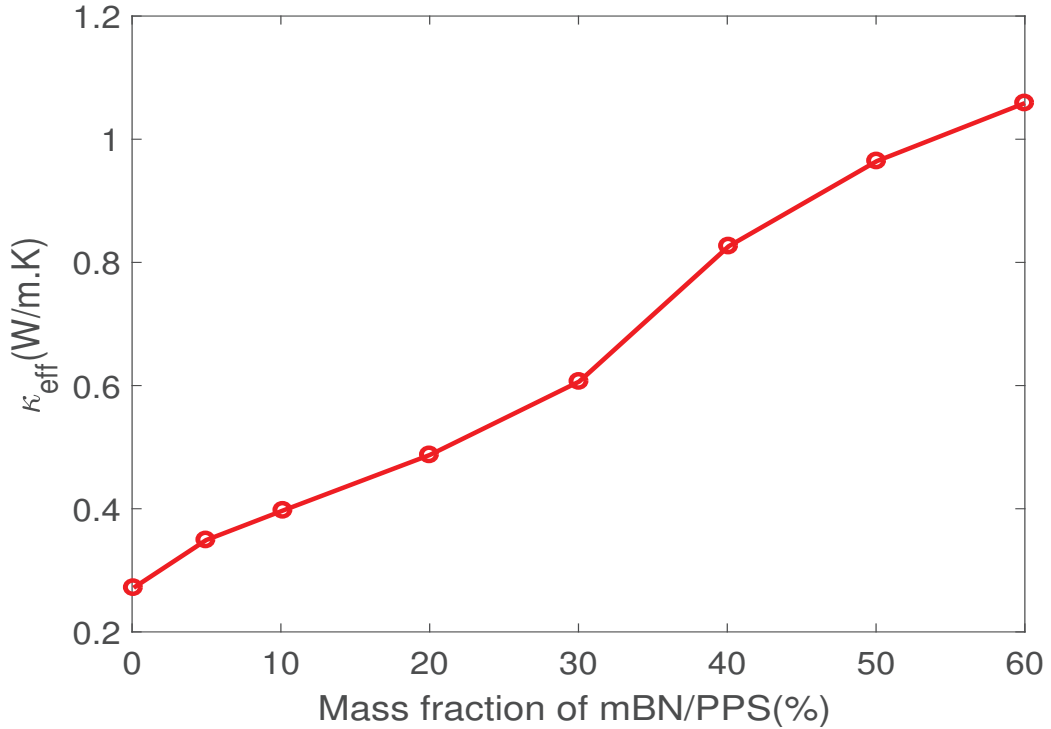


**Figure 1.2:** The data has been taken from this article [36]. The thermal conductivity of the nBN/PPS nanocomposites as a function of the percentage mass fraction of nBN/PPS nanocomposite.

Thermal behavior of macro-composites is usually described using the effective medium approach (EMA) which predicts the effective thermal conductivity of the system starting from the thermal properties of the components [37]. In the case of spherical nanoparticles of diameter  $d$  with a volume nanoparticle density  $n = 1/a^3$ , the general EMA for effective thermal conductivity of the composite ( $\kappa_e$ ) is given by [37]

$$\kappa_e = \kappa_h \times \frac{\kappa_p(1 + 2\xi) + 2\kappa_h + 2\varphi[\kappa_p(1 - \xi) - \kappa_h]}{\kappa_p(1 + 2\xi) + 2\kappa_h - \varphi[\kappa_p(1 - \xi) - \kappa_h]} \quad (1.3)$$

Where  $\kappa_h$  is the thermal conductivity of the host material,  $\kappa_p$  is the thermal conductivity of a particle, and  $\varphi$  is the volume fraction of the particle inclusions, defined for spherical particles as

$$\varphi = \frac{(4/3)\pi(d/2)^3}{a^3} = \frac{\pi d^3}{6a^3} \quad (1.4)$$

Finally,  $\xi$  is a dimensionless parameter defined as follows

$$\xi = \frac{\kappa_h R}{d/2} \quad (1.5)$$

Where  $R$  is the thermal boundary resistance between the two materials. However, despite its success for macro-composites, this approach fails in explaining the behavior in nanocomposites when the phonon mean free path (MFP) is comparable to the size of the inclusion [38]. Minnich introduced a modified form of EMA for nanocomposites [39] which accounts for the size effects of inclusions. He uses the concept of interface density ( $\Phi$ ), which is the ratio of the surface area of the inclusion to the volume of a cube that encloses one inclusion. In the case of spherical nanoparticles, it is given by

$$\Phi = \frac{4\pi(d/2)^2}{a^3} = \frac{6\varphi}{d} \quad (1.6)$$

The interface density is taken into account in the phonon MFP, affecting the effective thermal conductivity. In nanocomposites, a phonon encounters  $N = \pi d^2 L n / 4$  inclusions corresponding thus to  $N$  collisions travelling a distance  $L$  in average. The traveled distance divided by the number of inclusions is the MFP due to the collision ( $\Lambda_{coll}$ ) of the phonon with the inclusions

$$\Lambda_{coll} = \frac{L}{N} = \frac{L}{\pi d^2 L n / 4} = \frac{4a^3}{\pi d^2} = \frac{2d}{3\varphi} \quad (1.7)$$

The collision MFP can be related to the interface density by the following

$$\Lambda_{coll} = \frac{4}{\Phi} \quad (1.8)$$

The effective MFP of the host material ( $\Lambda_{eff,h}$ ) is dependent on the bulk MFP of the host ( $\Lambda_{bulk,h}$ ) and collision MFP according to the Mathiessen's rule such that

$$\frac{1}{\Lambda_{eff,h}} = \frac{1}{\Lambda_{bulk,h}} + \frac{1}{\Lambda_{coll}} = \frac{1}{\Lambda_{bulk,h}} + \frac{\Phi}{4} \quad (1.9)$$

The effective MFP of the inclusion phase ( $\Lambda_{eff,p}$ ) is a function of the bulk MFP of the inclusion and a characteristic length of the inclusion. In the case of spherical inclusion, this characteristic length is the diameter  $d$ . Using Mathiessen's rule, the  $\Lambda_{eff,p}$  is given as follows

$$\frac{1}{\Lambda_{eff,p}} = \frac{1}{\Lambda_{bulk,p}} + \frac{1}{d} \quad (1.10)$$

The thermal conductivity of the host and the particle phase in equation (1.3) is related to the MFP through the kinetic theory of phonon gas as following

$$\kappa = \frac{1}{3} C v \Lambda \quad (1.11)$$

Where  $C$  is the specific heat and  $v$  is the phonon group velocity. The EMA approach of the thermal conductivity has the following form

$$\frac{\kappa_{eff}(\Phi, d)}{\kappa_h} = \frac{\kappa_p(d)(1 + 2\xi(\Phi, d)) + 2\kappa_h(\Phi) + 2\varphi[\kappa_p(d)(1 - \xi(\Phi, d)) - \kappa_h(\Phi)]}{\kappa_p(d)(1 + 2\xi(\Phi, d)) + 2\kappa_h(\Phi) - \varphi[\kappa_p(d)(1 - \xi(\Phi, d)) - \kappa_h(\Phi)]} \quad (1.12)$$

Where  $\Phi$  can be found from equation (1.6), and the host thermal conductivity and particle thermal conductivity have the following forms based on the modified approach for the phonon MFP

$$\kappa_h = \frac{1}{3} C_h v_h \frac{1}{(1/\Lambda_{bulk,h}) + (\Phi/4)} \quad (1.13)$$

$$\kappa_p = \frac{1}{3} C_p v_p \frac{1}{(1/\Lambda_{bulk,p}) + (1/d)} \quad (1.14)$$

The agreement of the modified EMA with the measured thermal conductivity of SiGe nanocomposites with Si nanoparticles embedded in a Ge host is shown in figure (1.3.a). However, this model fails in explaining the thermal conductivity in some system of spherical crystalline GaN nanoinclusions embedded in an amorphous SiO<sub>2</sub> matrix as shown in figure (1.3.b), the blue dotted and the blue dashed are the EMA approach with and without thermal boundary resistance. The EMA in both cases don't match with the molecular dynamics simulations. The stronger increase in effective thermal conductivity of the system with respect to the volume fraction can be understood as the result of a percolation through

the inclusions. The model of the percolation EMA is given by the following equation [40]

$$\varphi \frac{\kappa_p^{\frac{1}{t}} - \kappa_e^{\frac{1}{t}}}{\kappa_p^{\frac{1}{t}} + A\kappa_e^{\frac{1}{t}}} + (1 - \varphi) \frac{\kappa_h^{\frac{1}{t}} - \kappa_e^{\frac{1}{t}}}{\kappa_h^{\frac{1}{t}} + A\kappa_e^{\frac{1}{t}}} = 0 \quad (1.15)$$

Where  $t$  is a parameter representing the asymmetry of the microstructure in terms of the connection between the grains,  $A$  is the ratio of the actual percolation threshold  $\varphi_c$  (the particle in the host), through the following equation  $A = (1 - \varphi_c)/\varphi_c$ . The fit of this model is the green dash-dot line in figure (1.3.b), this fit gives good results only at small volume fraction. This suggests that the effective volume fraction is bigger than the real one. This problem can be solved by fitting the volume fraction with the data which is the green dash line in figure (1.3.b), in this fit the volume fraction is doubled. This indicates that there is an enhancement of thermal conductivity with respect to what standard EMA theories can predict, and has been suggested that phonon tunneling between inclusions takes place. The failure of the EMA can be understood from recent theoretical works, directly looking to the effect of the nanoinclusions on phonons [41]. The effects on dynamics are non trivial, and their effect on thermal transport depends on the nature of the most perturbed phonons [13, 41].

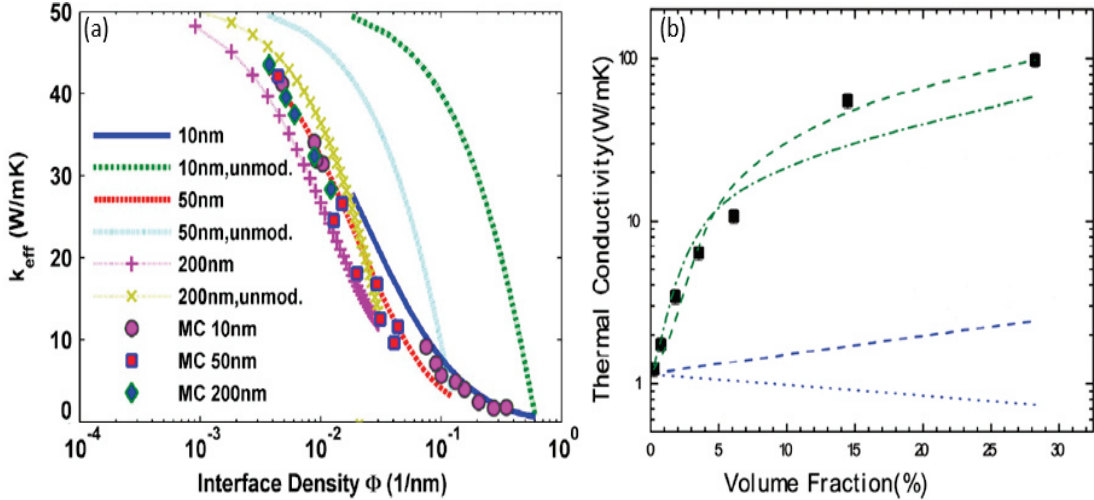


**Figure 1.3:** a) This figure is adapted from this article [39]. Effective thermal conductivity of a SiGe nanocomposite with spherical inclusions calculated by the modified and unmodified EMA formulations, along with data from Monte Carlo simulations [39, 42]. b) This figure is adapted from this article [33]. Black points are computed by molecular dynamics simulations, the blue dotted line and the blue dashed line are calculated using the EMA model with and without thermal boundary resistance ( $\alpha=0$ ) respectively, and green curves are calculated using EMA with percolation thermal conductivity as a function of volume fraction (dash-dot for a normal set of parameters and dash for two times volume fraction) [33].

Yang et al. [26] found that the thermal conductivity of Si phononic crystals with spherical pores depends on the porosity of the material, where the thermal conductivity of the material decreases as the porosity increase . This can be understood from the calculation of the participation ratio  $P$  [43] which is a quantitative description of phonon modes localization in the material, the value of  $P$  is between 0 and 1. In a system with more localized phonon modes the value of  $P$  is smaller, the value of  $P = 1$  means that all atoms participate in the motion. In the case of a Si phononic crystal with spherical pores, the values of  $P$  are much smaller than those of bulk Si, which means that phonon modes in Si phononic crystals are likely localized. This gives an explanation of the thermal conductivity behavior in this system.

Luo et al. [13] conducted Molecular Dynamics (MD) simulations for a two dimensional silicon-based amorphous matrix with embedded crystalline circular inclusions with different rigidities. By investigating the time dependence of energy transport, they could identify different phonon regimes: propagative, diffusive, localized or mixed. They could then build a frequency dependent phase diagram, as shown in figure (1.4). For large rigidity contrasts and for high frequencies, it is more pronounced the departure from the propagative regime. This actual behavior is due to the presence of several phenomena in the system such as scattering at matrix/inclusion interfaces, waves interference, waves reflection on curved surfaces inducing billiard motion, gallery modes along the interfaces, or acoustic resonances of the inclusions.

Tlili et al. [41] investigated a microscopic picture of phonon dynamics with the macroscopic thermal conductivity calculation of nanocomposites made of crystalline nanoinclusions Si embedded in an amorphous matrix of Si. The thermal conductivity at room temperature increases with the volume fraction of the crystalline inclusions, due to the addition of a better conductor material and a negligible thermal boundary resistance at the inclusion-matrix interface. This behaviour can be well described by the EMA model [39]. Looking directly to phonons, it is found that nanostructuring enhances phonon scattering and reduces phonon mean free path, anticipating the propagative regime to diffusive regime crossover. This leads to a decrease in the number of modes available for propagative thermal transport, and it narrows the phase space of propagative phonons. However, the effect of such stronger attenuation on the macroscopic thermal conductivity depends on the relative weight of propagative and diffusive contribution to the thermal transport in the matrix material [41].

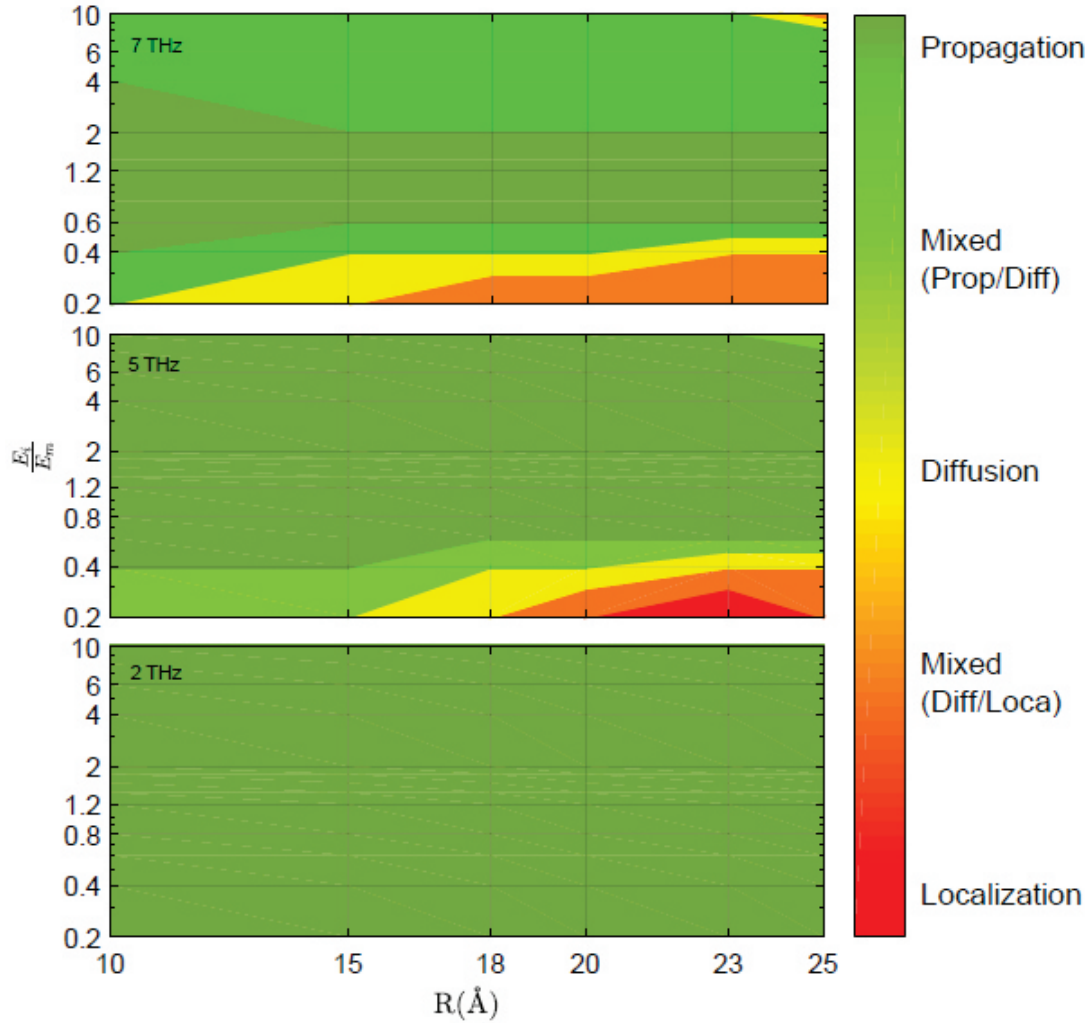


**Figure 1.4:** This figure is taken from this article [13]. Visualization of the different dynamical regimes of the Wave Packets (propagative, diffusive, localized), as a function of the radius  $R$  of the inclusions and of the relative rigidity  $E_i/E_m$  ( $E_m$ : Young's modulus) for frequencies  $\omega$  ranging from 2 to 7 THz.

### 1.2.2 The Effect of Size Reduction: Guided Waves in Thin Film and Membranes

The following sections are distributed as following, the first section gives an overview about guided waves, and the other two sections study the guided waves in free membrane and thin film deposited on a substrate [44].

## Guided Waves

The equation of motion that governs particle motion  $u_i$  in a direction  $i$  ( $i = x, y, \text{ or } z$ ) in the material is given as,

$$\rho \frac{\partial^2 u_i}{\partial t^2} = \frac{\partial}{\partial x_j} \sigma_{ij} \quad (1.16)$$

Where  $\rho$  is the density, and  $\sigma_{ij}$  is the stress ( $i$  is the component of the force per unit area acting on  $j$  face). According to Hooke's law the stress can be written as,

$$\sigma_{ij} = \sum_{\alpha\beta} C_{ij\alpha\beta} \epsilon_{\alpha\beta} \quad (1.17)$$

Where  $C_{ij\alpha\beta}$  is the elastic constant tensor, and  $\epsilon_{\alpha\beta}$  is the strain. Substituting equation (1.17) in equation (1.16) leads to the equation of motion as,

$$\rho \frac{\partial^2 u_i}{\partial t^2} = \frac{\partial}{\partial x_j} \sum_{\alpha\beta} C_{ij\alpha\beta} \epsilon_{\alpha\beta} \quad (1.18)$$

For a plane wave solution of form  $u_i(\mathbf{r}, t) = U_i \exp(-i\mathbf{k}\cdot\mathbf{r} + i\omega t)$  ( $\omega$  is the frequency of the wave and  $\mathbf{k}$  is the wave vector), we can obtain the Christoffel equation as,

$$C_{ijkl} k_k U_l k_j - \rho \omega^2 U_i = 0 \quad (1.19)$$

The wave solution in a material is obtained by solving equation (1.19) which depends on the nature of the material, dimensions, surface conditions, and interface conditions. The continuity conditions at the surface or interface for the velocity field  $v_i$  and the stress ( $\sigma_i$ ) between two media 1 and 2 are given as,

$$\mathbf{v}_1 = \mathbf{v}_2 \quad (1.20)$$

$$\sigma_1 \cdot \mathbf{n} = \sigma_2 \cdot \mathbf{n} \quad (1.21)$$

Where  $\mathbf{n}$  is the normal vector at the interface between the two media. We are interested in understanding the guided wave in material which is the superposition of the bulk waves respecting the boundary conditions of the material of the system. The multiple reflections from boundaries engender guided acoustic waves travelling parallel to the surface. This is only possible when the wave realizes constructive interference with its reflection every time. This leads to waves given by the superposition of a standing wave perpendicular to the surface and a propagating wave parallel to the surface, where the wave vectors are defined by the conditions for constructive interference.

The systems under study in this Phd thesis are free membranes (plate with free boundary) and thin film deposited on a substrate. In the following sections, we will give an overview about guided waves in these type of materials.

### Modes in Free Membranes

In the case of the membrane as shown in figure (1.5.a), there are different types of waves, the shear horizontal wave propagates in the  $y$ - $z$  plane and it is polarization along  $x$ , also called Love waves. The longitudinal wave propagates in the  $y$ - $z$  plane and the polarization along the direction of propagation as shown in figure (1.5.b)), and the shear vertical wave propagates in the  $y$ - $z$  plane and the polarization perpendicular to the direction of propagation as shown in figure (1.5.c)). The shear vertical wave when combined with the longitudinal wave forms waves called Lamb waves since these types of waves can't appear separately.

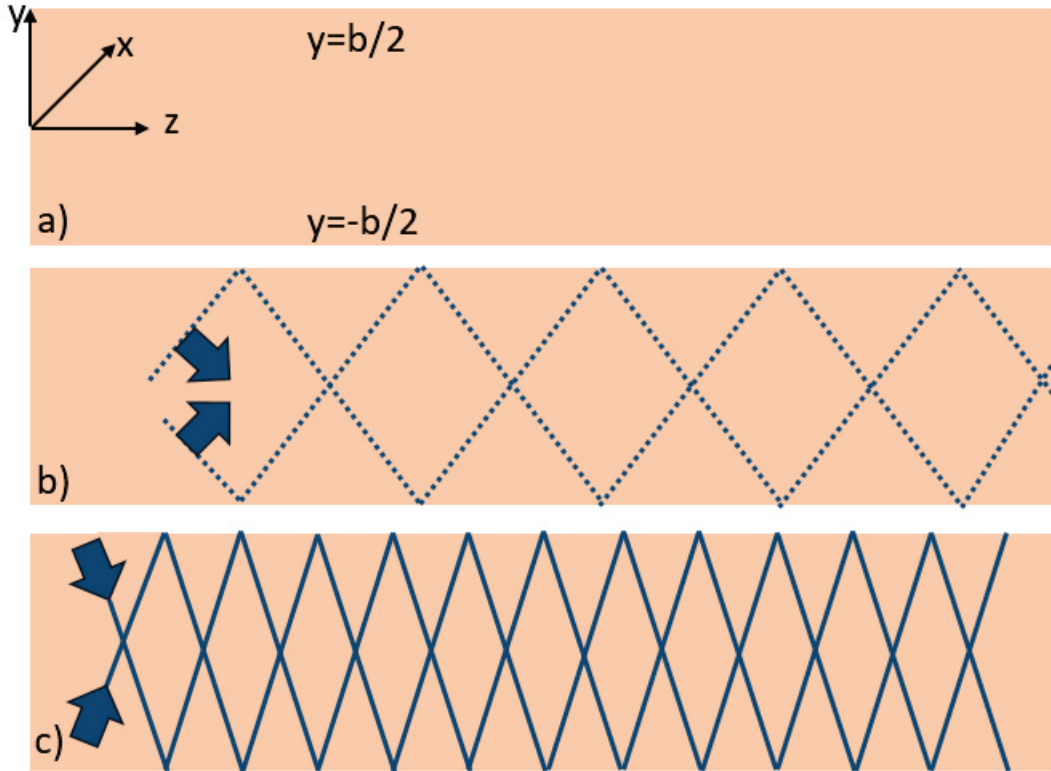


**Figure 1.5:** a) Schematic diagram of the membrane with thickness  $b$ . b) Schematic diagram of the propagation of the longitudinal wave where the thick vector is the direction of polarization. c) Schematic diagram of the propagation of the vertically polarized shear wave where the thick vector is the direction of polarization

The reduction of dimensionality imposes boundary conditions which affect phonon propagation [44]. The dispersion relation of energy ( $\omega$ ) as a function of the

wavevector ( $k$ ) of an isotropic plate with a free boundary, with thickness  $b$  due to a shear horizontal mode is given as,

$$k^2 = \left(\frac{\omega}{V_s}\right)^2 - \left(\frac{n\pi}{b}\right)^2 \quad (1.22)$$

Where  $n=0,1,2,3, \dots$ , and  $V_s$  is the shear sound velocity. We can see in the limit of large  $b$  (bulk material) that the dispersion is linear. As an example, the dispersion relation of amorphous  $\text{Si}_3\text{N}_4$  suspended membrane with different thicknesses of 5nm and 200nm is shown in figure (1.6).

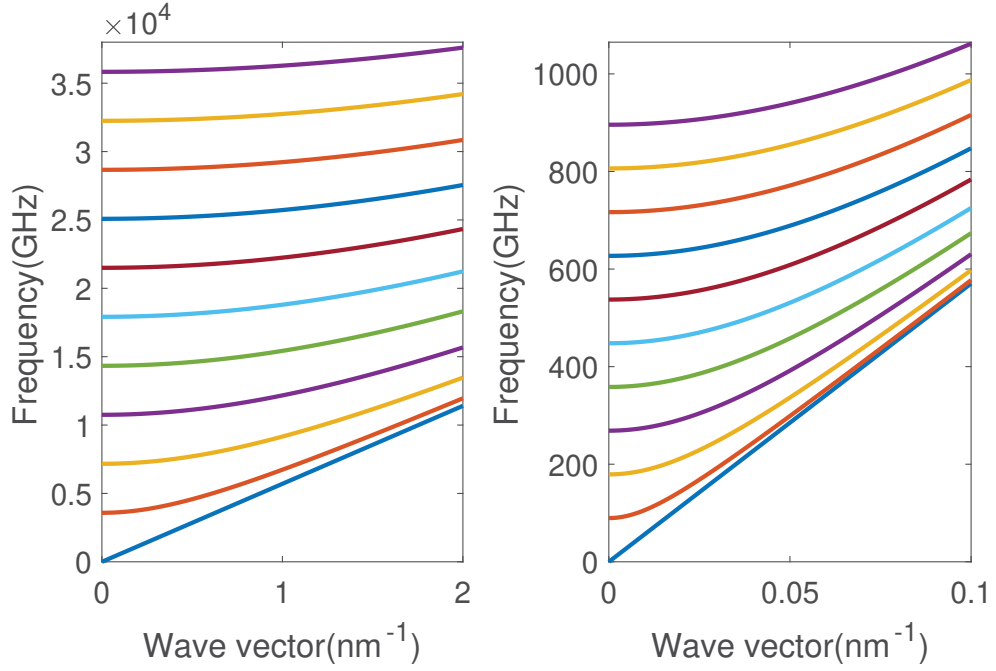


**Figure 1.6:** Dispersion relation of suspended membrane of  $\text{Si}_3\text{N}_4$  of 5nm (left) and 200nm (right) calculated using equation (1.22), the lowest curve is for  $n=0$  (zeroth order), and the other curves are in the ascending order where the highest curve is for  $n=10$ .

In a plate with a free boundary, the vertical shear wave and longitudinal wave cannot exist individually, but they are coupled and give rise to Lamb waves. The solution for the Lamb waves can be either symmetric or antisymmetric with respect to the reflection from the boundary of the plate.

$$\frac{\tan(k_{ts}b/2)}{\tan(k_{tl}b/2)} = -\frac{4k^2k_{tl}k_{ts}}{(k_{ts}^2 - k^2)^2} \quad (1.23)$$

And in the antisymmetric case:

$$\frac{\tan(k_{ts}b/2)}{\tan(k_{tl}b/2)} = -\frac{(k_{ts}^2 - k^2)^2}{4k^2k_{tl}k_{ts}} \quad (1.24)$$

The dispersion law for longitudinal and shear components will thus be

$$\omega = V_l \sqrt{k_{tl}^2 + k^2} \quad (1.25)$$

$$\omega = V_s \sqrt{k_{ts}^2 + k^2} \quad (1.26)$$

Where  $V_l$  and  $V_s$  are the longitudinal velocity and shear velocity, respectively. In the symmetric modes, the boundaries of the plate periodically dilate and contract, these modes are called dilatational ( $L$ ). The antisymmetric modes are called flexural ( $F$ ) because of the periodic flexing motion of the boundaries. In the limit of large  $kb$ , the  $F_1$  and  $L_1$  fundamental modes become exactly degenerate, and they form a surface wave called Rayleigh surface wave. The amplitude of the Rayleigh wave decreases with the depth in the material, so that atomic motion is localized near the surface, and the particle motion of this wave is elliptically polarized in the plane perpendicular to the surface in the direction of the propagation. Remembering the definition of the Poisson's ratio [45, 46]:

$$\sigma = \frac{1 - 2(V_s/V_l)^2}{2(1 - (V_s/V_l)^2)} \quad (1.27)$$

It has been shown that the Rayleigh surface wave velocity  $V_R$  for  $\sigma \in [0, 0.5]$  can be approximated by,

$$\frac{V_R}{V_s} \sim \frac{0.87 + 1.12\sigma}{1 + \sigma} \quad (1.28)$$

To understand thermal transport in thin membranes, it is important to investigate these waves as well, which carry heat parallel to the surface and can be strongly affected by a nanostructuring of the kind investigated in this thesis [47, 48].

### Modes in Thin Films

In the following, we will discuss the guided waves of a thin film on a substrate. In this case, part of the wave is reflected from the interface and the other part of the wave is transmitted to the substrate. First kind of waves seen in this material are called Love waves where they are shear waves with a polarization parallel to the boundary between the thin film and the substrate. These waves are reduced to shear horizontal waves discussed in the membrane in the case of the mass density of the substrate reduced to zero [44]. Depending if the wavevector perpendicular to the surface in the substrate  $k'_{ts}$  is imaginary or real, the wave will be confined in the thin film or be transmitted in the substrate. In this latter case it will carry energy away from the thin film. For this reason it will be called a leaky wave and has imaginary  $k'_{ts}$  as,

$$k'_{ts} = -i\alpha'_{ts} \quad (1.29)$$

Where the transverse decay constant in the substrate is  $\alpha'_{ts}$ . The dispersion relation in the thin film is given as,

$$\omega = V_s \sqrt{k_{ts}^2 + \beta^2} \quad (1.30)$$

$$\omega = V'_s \sqrt{\beta^2 - \alpha'^2_{ts}} \quad (1.31)$$

Where  $V_s$  and  $V'_s$  are the shear velocity in the thin film and substrate, respectively,  $k_{ts}$  is the transverse component of the wave vector in the thin film,  $\beta$  is the wavevector parallel to the surface, common to both thin film and substrate. The condition that relates the dispersion relation between the two media which is based on the interface and surface conditions is given as,

$$\tan(k_{ts}b) = \frac{V'^2_s \rho'_s \alpha'_{ts}}{V_s^2 \rho_s k_{ts}} \quad (1.32)$$

Where  $\rho'_s$  and  $\rho_s$  are the density of the thin film and the substrate, respectively. Similar considerations hold for the generalized lamb waves. However in this case the solution of wave vectors is much more complex.

### 1.2.3 Phonons in Phononic Crystals

In a material with periodic nanostructuration, a strong modification of the phonon dispersion relation is expected due to the change of the periodicity, it emerges from band folding and band splitting due to the increase of the periodicity length [49]. The phonon dispersion relation in a uniform system is defined in the Brillouin zone, the periodicity of the system is most probably in the atomic distance. However, in a system with periodic nanostructuration the periodicity distance usually increases, the Brillouin zone in a periodic nanostructuration system decreases. This leads to modification of the dispersion relation where the band folds to the narrow region of the Brillouin zone due to the nanostructuration, and forbidden energy regions gaps for which phonons cannot propagate, cannot exist, which make them interesting for realizing filters. The phonon propagation is affected by the diffusion from the interfaces introduced by the nanostructuration and the present existence of the different mechanisms such as diffusion from interfaces, reflection from interfaces and coherent interference, which can lead to phonon localization (constructive interference) or depletion (destructive interference). The coherent effects appear only in phononic crystals, while the diffusion appears in disordered random nanocomposites as well. Still, for coherent effects to exist, an almost specular reflection needs to exist. The coherent phonon regime is reached when the specularly parameter is above 0.5, the specularly parameter ( $p$ ) of the material is given by the following equation,

$$p = \exp\left(-\frac{16\pi^3\Sigma^2}{\lambda^2}\right) \quad (1.33)$$

Where  $\lambda$  is the phonon wave length, and  $\Sigma$  is the modified roughness due to the disorder of the holes is dependent on the disorder of the system ( $\epsilon$ ) and the surface roughness of the material ( $R$ ) as follows,

$$\Sigma = \sqrt{R^2 + (\epsilon/2)^2} \quad (1.34)$$

The frequency of the maximum coherent phonon (MCP) based on equation (1.35) is given by the following equation,

$$\omega(R) = \sqrt{\frac{-\ln(p)}{16\pi^3}} \cdot \frac{v_L}{\Sigma} \quad (1.35)$$

Where  $v_L$  is the longitudinal speed of sound. The coherent effects will affect thermal transport only if the phonons dominating heat transport are coherent, i.e. the specular parameter is close to 1. This allows for reflection on the critical role of roughness with respect to the phonon wavelength: at room temperature, phonon wavelengths are sub-nm, thus the roughness should also be sub-nm. Only the very advanced material processing methods allowing for such a low roughness allow for building phononic crystals for thermal control. The modification of the phonons due to surface nanostructuring is studied in different systems.

Wagner et al. [50] investigated the effect of order/disorder in phononic crystals on the phononic properties. Three systems of Si membranes are examined in this study, these are 250 nm Si membranes with 1 nm surface roughness, Si membranes with 2D ordered holes of 175 nm hole diameter and pitch of 300 nm with 7 nm hole wall roughness, and disordered systems of holes with maximum displacement of 22.5 nm. The coherent acoustic phonon dynamics of this system is inspected using time-resolved femtosecond pump-probe spectroscopy to measure zone-center phonon dynamics in the time domain. The effect of order/disordered is clearly seen, the coherent frequency range is reduced in the disordered system. The effect of the holes is observed in the phonon dispersion relation due to change in the periodicity of the material arising from band folding. The effect of order and disorder on acoustic phonon spectrum between systems is discovered that phonon with frequency above 20 GHz cannot be detected. The study of the phonon coherence of the material is extremely important where the roughness of the material is a key parameter of this study especially on the materials with nanostructured surface.

Moreover, Iskandar et al. measured the heat capacity over 3-300 K temperature range of a set of Si samples with surface nanostructuring which have truncated cone-like Si structures [51]. In this systems, the low frequency phonon density of states is calculated from the heat capacity measurement. The low frequency density of state does not change in a material with truncated cone-like structures

of small height and broad apex. It enhances in periodically arranged cone-like structures with sharp apexes, but it is weakened in periodically arranged pillar-like structures and tall truncated cone-like structures. The flatness of the low frequency acoustic branch enhances the low frequency density of state, and the enhancement of the phonon modes frequencies reduces the low frequency density of state.

# Chapter 2

## Experimental Methods

In this work, the measurement of the thermal conductivity in thin films is performed using the thin film laser flash technique (TFLFA), and measurement of phonons is performed by Extreme Ultraviolet Transient Grating (EUV-TG) technique using Free Electron Lasers (FELs). By directly studying the heat carriers, the phonons, a better understanding of the macroscopic thermal transport properties can be achieved. In the following sections (2.1) and (2.2), we will describe the TFLFA and EUV-TG experiments, respectively.

### 2.1 Thin Film Laser Flash Technique

The TFLFA setup used in this thesis is a commercial equipment provided by Linseis for measuring the thermal conductivity of thin films. We will describe, in section (2.1.2), the experimental technique, and, in section (2.1.3), the theoretical model allowing to interpret the measurements.

#### 2.1.1 Technique Principle Description

The surface of the sample is heated by a pulsed pump laser beam with pulse width in the ns range. Its reflectivity as a function of time is measured using a continuous probe laser beam and a time resolved detector. The reflectivity depends on the surface temperature. By measuring the reflectivity as a function of time, we thus measure the time dependence of the temperature in the surface layer. Its cooling down, or thermal relaxation, is due to the heat flux propagating into all layers of the stacking, so the time dependence of its temperature will depend on the thermal properties of the different layers, among which is the sample. The measured signal of reflectivity is a function of physical intrinsic parameters thermal conductivity ( $\kappa$ ), heat capacity ( $C$ ), density ( $\rho$ ), thickness ( $d$ ) of each layer, and thermal resistance at each interface. It is fitted with the Cahill model adapted to time domain measurements [52,53] described in section (2.1.3),

where all the parameters should be known except for the thermal conductivity of the layer of interest and the thermal resistances are assumed to be negligible. The following paragraph provides a description of the general procedure of the measurement and shows the metrology study that I have done in order to test the impact of the different instrumental and sample parameters on the measurement.

### 2.1.2 Experimental Apparatus

The sample used in our experiment, as shown in figure (2.1), is a thin film on a substrate, coated with a thin layer of 5 nm of chromium (Cr), and 100-200 nm of gold (Au) on top of the Cr layer. The Cr layer is a diffusion barrier for avoiding Au diffusion within the sample at high temperature. The pump/probe laser wavelengths have been chosen to maximize and minimize respectively the Au absorption and the reflectivity derivative with respect to temperature is called the thermorefectance ( $TR$ ) coefficient,

$$TR = \frac{1}{R} \frac{dR}{dT} \quad (2.1)$$

Where  $R$  is the reflectivity. Both are reported in figure (2.2) as a function of the pump and probe wavelength.

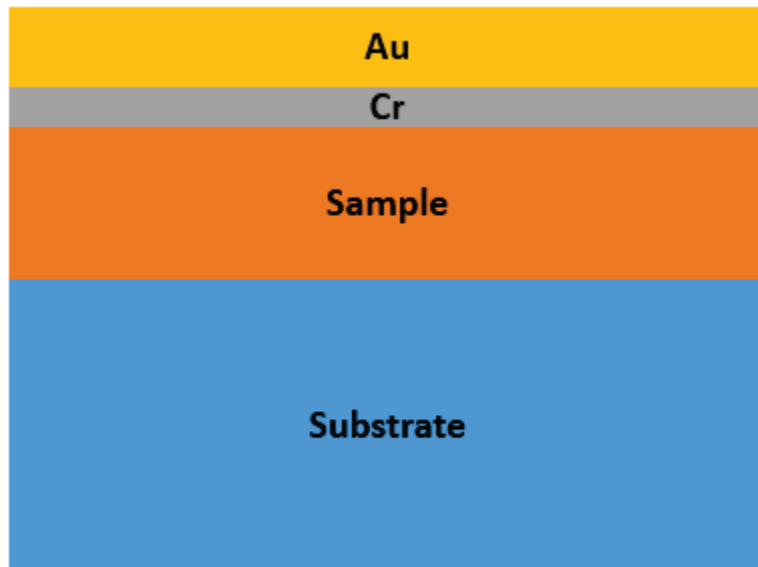


**Figure 2.1:** This sketch shows the typical sample geometry in TFLFA experiment. The Cr layer is a barrier of Au diffusion into the sample. Typically a metallic coating is added on the sample, here Au. The temperature dependence of its reflectivity and its physical properties (thermal conductivity, thickness, specific heat, density) are well known.

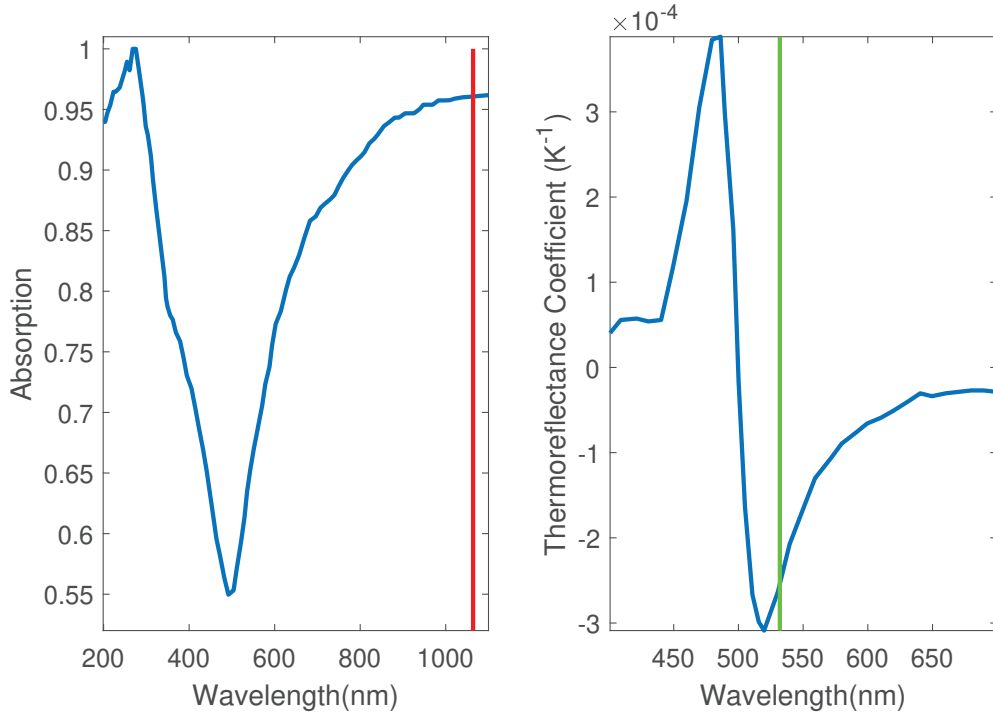


**Figure 2.2:** a) The absorption of gold vs pump wavelength as reported in [54], the red line is the wavelength of our pump beam (1064 nm). b) The thermoreflectance coefficient of Gold vs probe wavelength as reported in [55], the green vertical line is the wavelength of our probe beam (532 nm).

### Optimization of the Measurement

The TFLFA technique is schematized in figure (2.3). The probe laser beam is a green laser with wavelength 532 nm, 3.8  $\mu\text{W}$  power on the sample, diameter  $0.7 \pm 0.07$  mm, and divergence  $< 1.3$  mrad. The pump laser beam is in the infrared with wavelength of 1064 nm, diameter 3.5 mm, pulse width 8 nsec, 10 Hz repetition rate, and 2.8 mW pulse power on the sample. The sample holder can host samples with a diameter in the range 12.7-25.4 mm. The sample chamber is a cryo-furnace able to span a temperature range from  $-90$   $^{\circ}\text{C}$  to  $500$   $^{\circ}\text{C}$ . The photo-diode detector is time-resolved with an active area of 0.8 mm, the photo-diode converts light into electric signal. The bandwidth of the photo-diode is 400 MHz, and the spectral response is in the range 320-1000 nm. The signal is extracted with an acquisition card at a frequency of 2.5 GHz, the measured signal is the intensity of the reflected beam as a function of time.

**Reference Sample** For testing the system, we have used as reference sample a thin film of 504 nm of Silica ( $\text{SiO}_2$ ) deposited on a Silicon (Si) substrate coated with 4 nm of Cr and 190 nm of Au. Silica thermal conductivity has been largely

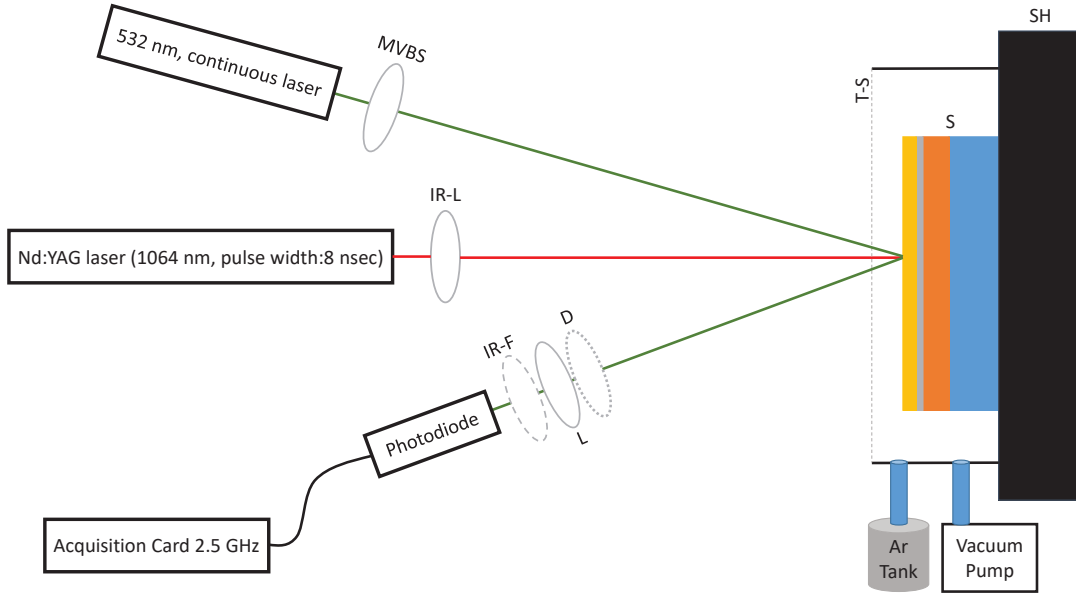


**Figure 2.3:** This figure shows the sketch of the thermoreflectance measurement. MVBS= Mounted Variable Beam Splitter, IR-L= Infrared Lens, IR-F= Infrared Filter, L: Lens, D: Diaphragm, SH= Sample Holder, S= Sample, and T-S= Transparent Surface.

investigated in the literature, and measured with a variety of techniques. The thermal conductivity of a  $\text{SiO}_2$  film of thickness 190 nm measured by  $3\omega$  method is 1.14 W/m.K [56], and it is 0.96 W/m.K for 533 nm thickness measured by frequency domain photoreflectance microscopy [57].

**System Alignment** There is a difficulty in aligning the two beams since the pump beam is in the infrared range. For this reason, another laser pointer of red color is used along the path of the pump beam to insure correct alignment, as shown in figure (2.4). The first question arising is about the reliability of the alignment made by looking to the visual superposition of red pointer laser and probe beam. The criticality of the pump/probe alignment is tested on a thin film of Silica on Silicon substrate by slightly changing the position of the pump beam in different directions and measuring the thermal conductivity at each position. The average value of thermal conductivity in different directions is  $0.91 \pm 0.03$  W/m.K. The measurement has a good agreement with the literature [57]. Since these measurements in different directions produced no significant variation beyond the error bar in the thermal conductivity, we conclude that the alignment of the two lasers made by eye on using the red pointer laser and the probe laser is satisfactory for a good measurement.

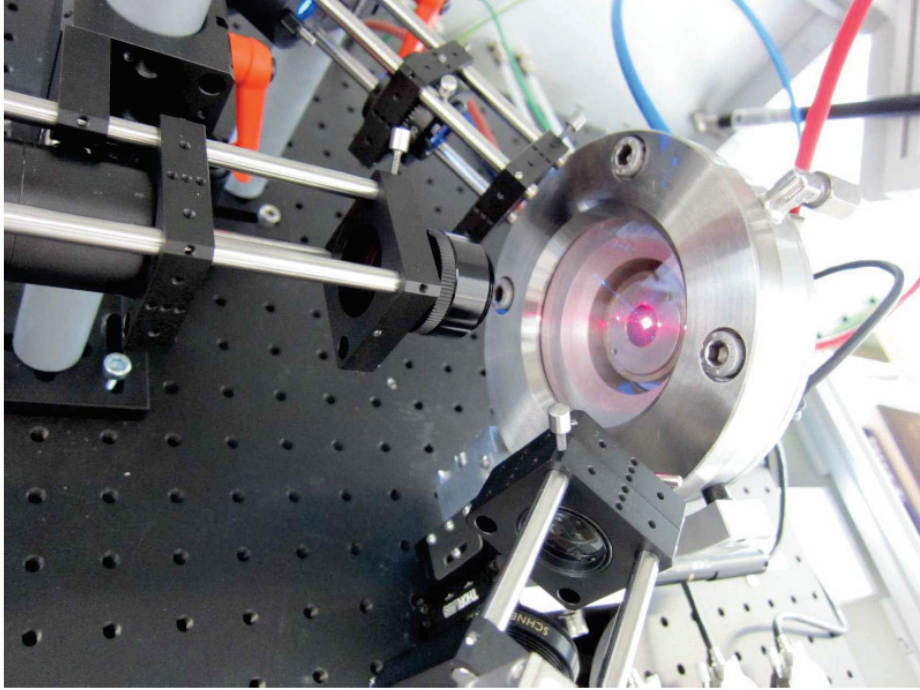


**Figure 2.4:** Image showing the alignment of the probe beam with the red laser pointer of the pump beam.

**Sensitivity Study** The shape of the heat relaxation depends on the thickness and thermal conductivity of all layers in the stacking. To visualize the effect of a given parameter ( $\Sigma$ ) on the reflectivity signal in time, we determined the sensitivity ( $S$ ) [58] which is the derivative of the logarithmic of the signal with respect to the given parameter ( $\Sigma$ ) and reads as:

$$S_{\Sigma} = \frac{\partial \log R}{\partial \log \Sigma} = \frac{\Sigma}{R} \frac{\partial R}{\partial \Sigma} \quad (2.2)$$

Where  $R$  in our case is the reflectivity from the surface of the sample, which depends on the thermal properties and thickness of the different layers as formulated in section (2.1.3). We can do the simulation of the sensitivity of the signal to the thermal conductivity, density, heat capacity, and thickness of each layer of the sample stacking as a function of time where the model of the reflectivity is discussed in section (2.1.3). This simulation helps us to choose the correct time window for fitting the signal and to study the sensitivity of the thermoreflectance signal to each layer for optimizing the stacking. The time window of the experiment is the time when the reflectivity signal starts to vanish. The sensitivity of the signal to the thermal conductivity of the thin film should be higher than the sensitivity to the substrate in the time window of the experiment for an accurate measurement of thermal conductivity of the thin film. An example is shown in

figure (2.5), for a 504 nm thick SiO<sub>2</sub> sample on a Silicon (Si) substrate. In this study the sensitivity to the thin film is much higher than the sensitivity to the substrate in the time window of the experiment around 2  $\mu$ s, so it is expected to have accurate measurement of the thermal conductivity of the thin film.

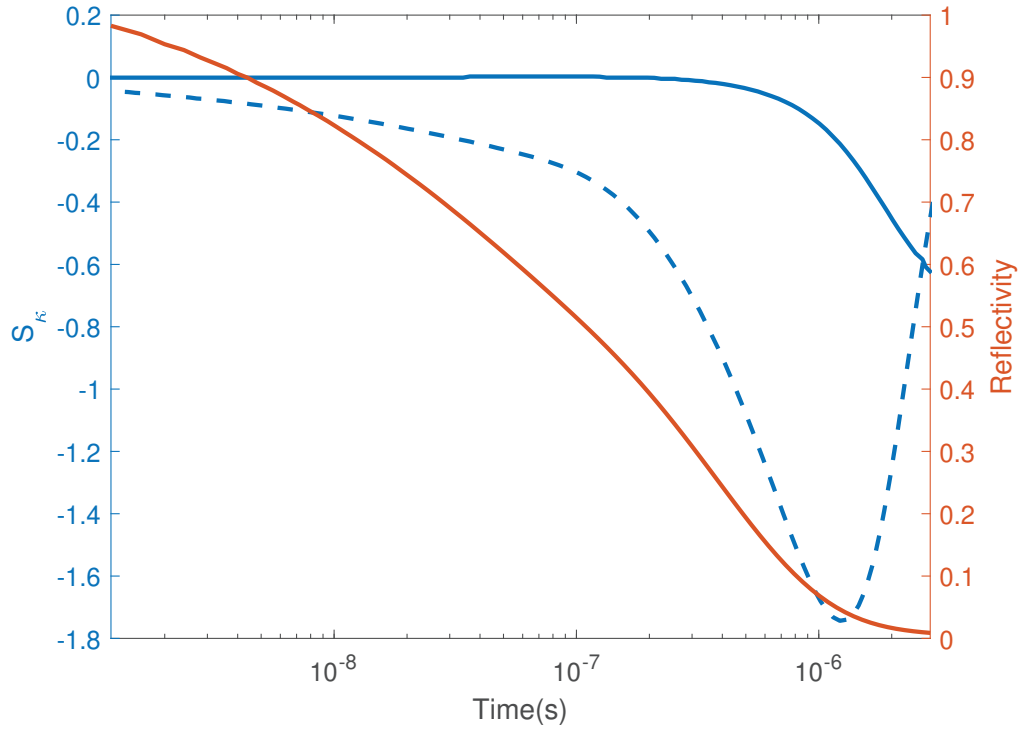


**Figure 2.5:** Example of sensitivity (left axes) curves to the thermal conductivity ( $\kappa$ ), and the time dependence of the reflectivity (right axes), as modelled using the given stacking and materials parameters for the sample described in Reference Sample. The blue solid line is the sensitivity of the measurement to the substrate thermal conductivity and the blue dashed lined is the sensitivity of the measurement to the thin film thermal conductivity.

This sensitivity study is essential for understanding the results and the correct time window for fitting the results. We tested the thermal conductivity measurement on a thin film of Silica described in section Reference Sample, as shown in figure (2.6). As previously said, we obtained on the reference sample a value of  $0.91 \pm 0.03$  W/m.K in good agreement with literature  $0.96 \pm 0.09$  W/m.K [57] confirming that the thermal conductivity measurement is accurate.

**Pump and Probe Beams Power** The next step in the experimental measurement is to test all instrumental parameters that could affect the measurement. This test helps us acquiring a clear image on how to operate this experiment

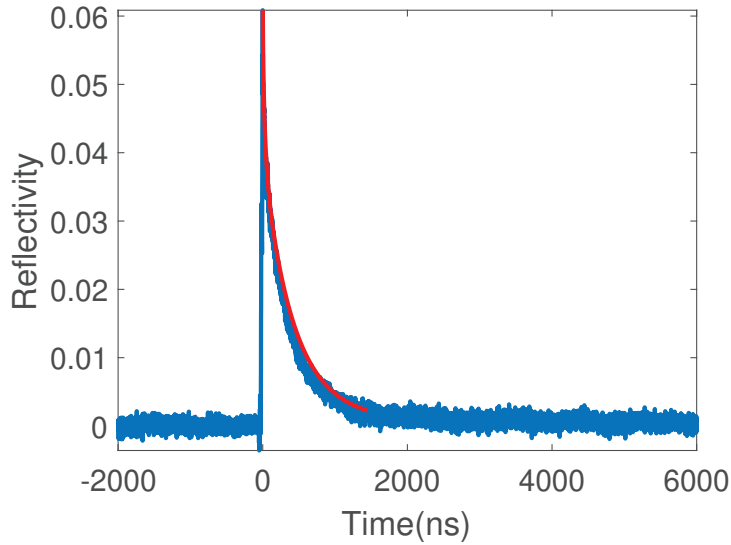


**Figure 2.6:** Example of a time resolved measurement of the reflectivity at the surface of a stacking Au/Cr/SiO<sub>2</sub>/Si(substrate) described in section [Reference Sample](#). The surface has been heated by the pump laser at  $t=0$ . The fit (red line) and the measured data (blue line) of 504 nm of SiO<sub>2</sub> on Si substrate.

properly. The maximum power pulse of the pump beam is 120 mJ. We varied the power of the pump beam impinging onto the sample to obtain a good signal and to avoid burning the Au layer. We have two ways to tune the power impinging onto the sample: the load voltage of the pump laser (drive) and a filter to attenuate it (attenuator). The larger the drive and attenuator value the higher the power impinging onto the sample. We scan the drive in the range 60-80% and attenuator in the range 10-65%. For example, the sample starts to burn at drive 60% attenuator 65%, and drive 80% attenuator 40%. The probe beam power is 25 mW, it is adjusted using the mounted variable beam splitter to have a signal around 850 mV on the photodiode detector which avoids saturation..

**Fitting the Data** The input parameters of this code is the thickness, heat capacity, density, and thermal conductivity of each layer of the sample stacking. In the code, each layer of the stacking is inserted in the right order with the thermal properties and thickness. The convergence of the fitted thermal conductivity of the thin film is investigated as a function of the input parameters. The sensitivity of the result to the precision with which we know these parameters can be easily tested by changing them within their uncertainty. In the [Reference Sample](#), the variation of the thickness of the thin film by 10% (50 nm) changes the thermal conductivity by 10% (0.1 W/m.K), the sensitivity will be different depending on the property investigated but as well on the material and the full stacking.

**High and Low Temperature Measurement.** As mentioned, the sample chamber is a cryo-furnace able to go from -90 °C to 500 °C. For the high temperature operation, the chamber is connected to a vacuum pump and an Argon gas tank. Before heating, the chamber is first pumped, then filled with Ar gas. This procedure is repeated three times. The chamber is full of Ar gas upon start of heating, the main reason of this procedure is to avoid oxidation at the surface at high temperature. In the range below room temperature, the sample chamber is connected to a liquid Nitrogen. If the system is used in the cooling mode, the chamber is evacuated using the same procedure during heating but at the end of the procedure, upon cooling, the chamber is left under vacuum. This procedure prevents from the formation of water condensation at the surface of the sample at low temperature.

### 2.1.3 Model of The Experiment

In order to fit the experimental data we use the code associated to the commercial setup, which is based on the Cahill model [52]. From fitting this model we can extract the thermal conductivity of the thin film. In the section **Reflectivity of the Probe Beam**, I will give a general description of the reflectivity of the probe beam. The reflectivity of the probe beam has a direct dependence on the temperature of the surface of the sample. This temperature distribution for a layered structure is estimated using the Feldman [53] algorithm for multilayers as discussed in section **Layered Structure Model**.

#### Reflectivity of the Probe Beam

The thermoreflectance or laser flash technique is based on the measurement of the surface temperature of the sample by measuring the reflectivity of the probe beam. Measuring the reflectivity of the sample gives us insight about the heat propagation in the sample based on the heat conduction equation [59]. The photodiode detector measures the change of reflectivity as a function of time  $t$ . In general, the reflectivity variation due to a temperature change  $R(t)$  is given as [52],

$$R(t) = \Delta R_M(t) \exp(i2\pi ft) \quad (2.3)$$

Where  $f$  is the frequency adjusted according to the time window of the experiment,  $M = 10 * \tau / \min(|t_{exp}|)$ ,  $\tau$  is the repetition rate of the heating beam, and  $t_{exp}$  is the time window of the experiment, and  $\Delta R_M(t)$  is the reflectivity change at time 0, i.e. at the arrival of the pump beam. The real part and the imaginary part of  $\Delta R_M(t)$  are given as,

$$\begin{aligned}
Re[\Delta R_M(t)] &= \frac{dR}{dT} \sum_{m=-M}^M (\Delta T(m/\tau + f) + \Delta T(m/\tau - f) \exp(i2\pi mt/\tau)) \\
Im[\Delta R_M(t)] &= -i \frac{dR}{dT} \sum_{m=-M}^M (\Delta T(m/\tau + f) - \Delta T(m/\tau - f) \exp(i2\pi mt/\tau))
\end{aligned} \tag{2.4}$$

Where  $\Delta T$  is the surface temperature variation. The convergence of this model is very low. This problem can be solved according to Cahill [52] by multiplying equation (2.4) with a Gaussian artificial decay  $\exp(-\pi(f/f_{max}))$ . Precise and smooth reproduction of the experimental results was found by choosing  $f_{max} = 10/\min(|t_{exp}|)$  [52].

### Layered Structure Model

In this section, we will discuss the solution of the anisotropic heat diffusion equation for a system with N-layers, as shown in figure (2.7), in cylindrical coordinates [60]. Each layer is characterized by its thickness ( $L_n$ ), volumetric specific heat ( $C_n$ ), thermal conductivity in radial direction ( $\kappa_{r,n}$ ), and thermal conductivity in  $z$  direction ( $\kappa_{z,n}$ ). The heat diffusion equation of layer  $n$  follows Fourier's law of heat conduction [52, 61, 62],

$$C_n \frac{\partial T_n}{\partial t} = \frac{\eta_n \kappa_{z,n}}{r} \frac{\partial}{\partial r} \left( r \frac{\partial T_n}{\partial r} \right) + \kappa_{z,n} \frac{\partial^2 T_n}{\partial z^2} \tag{2.5}$$

Where  $\eta_n = \kappa_{r,n}/\kappa_{z,n}$  is the anisotropic parameter of thermal conductivity. We apply Hankel transform to equation (2.5) for variable  $r$  and Fourier transform for time variable  $t$  [63]. The Hankel transform of a generic function  $f(r)$  is given by the following formula [63],

$$f(k) = 2\pi \int_0^\infty f(r) J_0(2\pi kr) r dr \tag{2.6}$$

Where  $k$  is the Hankel transform variable, and  $J_0$  is the zeroth order Bessel function.  $J_0$  is defined as,

$$J_0(x) = \frac{1}{2\pi} \int_0^{2\pi} e^{-ix \cos \beta} d\beta \tag{2.7}$$

After the two transformations, equation (2.5) is transformed in:

$$\frac{\partial^2 \Theta_n}{\partial z^2} = \lambda_n^2 \Theta \tag{2.8}$$

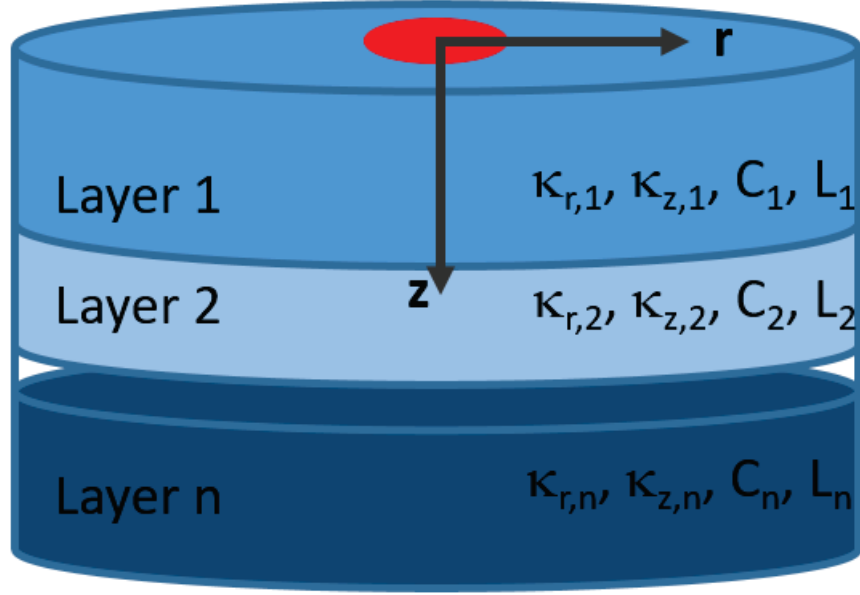


**Figure 2.7:** This figure is adapted from this article [62]. System with  $n$  layers where each layer is characterized by its thickness ( $L_n$ ), volumetric specific heat ( $C_n$ ), thermal conductivity in radial direction ( $\kappa_{r,n}$ ), and thermal conductivity in  $z$  direction ( $\kappa_{z,n}$ ). The red spot is to show the heating beam on the surface of the sample.

Where  $\Theta$  is the temperature in frequency domain, and  $\lambda_n^2 = 4\pi^2 k^2 \eta_n + i\omega C_n / \kappa_{z,n}$  with  $\omega$  is the angular frequency, and  $k$  is the Hankel variable. The general solution of equation (2.8) is the following,

$$\Theta_n = B_n^+ \exp(\lambda_n z) + B_n^- \exp(-\lambda_n z) \quad (2.9)$$

Where  $B_n^+$  and  $B_n^-$  are complex constants to be determined based on the boundary conditions: the continuity of temperature and the continuity of heat flux ( $Q_n = -\kappa_{z,n}(d\Theta_n/dz)$ ) at the boundary between two consecutive layers. These coefficients corresponds to the terms in the negative and positive directions for the solution of the  $N$ -layer heat conduction equation. The boundary conditions are applied between two consecutive layers  $n$  and  $n + 1$ . The continuity of temperature condition leads to,

$$B_n^+ \exp(\lambda_n L_n) + B_n^- \exp(-\lambda_n L_n) = B_{n+1}^+ \exp(\lambda_{n+1} L_n) + B_{n+1}^- \exp(-\lambda_{n+1} L_n) \quad (2.10)$$

And the continuity of heat flux leads to,

$$\gamma_n (-B_n^+ \exp(\lambda_n L_n) + B_n^- \exp(-\lambda_n L_n)) = \gamma_{n+1} (-B_{n+1}^+ \exp(\lambda_{n+1} L_n) + B_{n+1}^- \exp(-\lambda_{n+1} L_n)) \quad (2.11)$$

Where  $\gamma_n = K_{z,n}\lambda_n$ ,  $B_n^+$  and  $B_n^-$  can be found for all layered geometry using the algorithm described by Feldmann [53]. In this algorithm these variables are written in the matrix notation from equations (2.10) and (2.11) as follows,

$$\begin{pmatrix} B^+ \\ B^- \end{pmatrix}_n = \frac{1}{2\gamma_n} \begin{pmatrix} \exp(-\lambda_n L_n) & 0 \\ 0 & \exp(\lambda_n L_n) \end{pmatrix} \begin{pmatrix} \gamma_n + \gamma_{n+1} & \gamma_n - \gamma_{n+1} \\ \gamma_n - \gamma_{n+1} & \gamma_n + \gamma_{n+1} \end{pmatrix} \begin{pmatrix} B^+ \\ B^- \end{pmatrix}_{n+1} \quad (2.12)$$

The main purpose of this model is to study the temperature response on the surface of the sample due to the applied heat flux. This can be described using the Green function ( $\hat{G}$ ), which gives the ratio between temperature response and heat flux at the surface.

$$\hat{G}(k, \omega) = \frac{\Theta_{n=1, z=0}}{Q_{n=1, z=0}} = \frac{1}{\gamma_1} \left( \frac{B_1^- + B_1^+}{B_1^- - B_1^+} \right) \quad (2.13)$$

At rates comparable to the modulation frequency, heat can't reach the other side of the bottom layer, thus  $B_n^+ = 0$  and  $B_n^- = 1$  for the final layer, and we can find  $B_1^+$  and  $B_1^-$  iteratively from equation (2.12) [52].

**Heating Beam** The surface of the sample is heated by a pump laser beam with a Gaussian distribution of intensity  $p(r)$ ,  $r$  is the surface coordinate, the  $1/e^2$  radius of the pump beam is  $w_0$ .

$$p(r) = \frac{2A}{\pi w_0^2} \exp(-2r^2/w_0^2) \quad (2.14)$$

where  $A$  is the power of the pump beam at frequency  $\omega$ , and the  $\int_{-\infty}^{+\infty} p(r) = A$ . The aligned laser beams have cylindrical symmetry. The Hankel transform simplifies the convolution the solution of the heat diffusion equation with the distributions of the laser intensities [63, 64]. The Hankel transform of  $p(r)$  is given by the following formula,

$$P(k) = A \exp(-\pi^2 k^2 w_0^2 / 2) \quad (2.15)$$

**Temperature Oscillations at the Surface** The temperature distribution at the surface will be related to the pump beam power distribution and the heat flux, so it should be function of  $P(k)$  and  $\hat{G}(k)$ . In other words, the distribution of temperature oscillations at the surface  $O(r)$  is the inverse Hankel transform of the product  $G(k)$  and  $P(k)$ .

$$O(r) = 2\pi \int_0^\infty P(k) \hat{G}(k) J_0(2\pi kr) k dk \quad (2.16)$$

The change in reflectivity is measured by a probe laser beam. It also has a Gaussian distribution of intensity,  $w_1$  is the radius of the probe beam, and  $A_1$

is its power. The probe beam measures a weighted average of the temperature distribution  $\Delta T$ ,

$$\begin{aligned}\Delta T &= \frac{4A_1}{w_1^2} \int_0^\infty O(r) \exp(-2r^2/w_1^2) r dr \\ &= \frac{4 * 2\pi A A_1}{w_1^2} \int_0^\infty \hat{G}(k) \exp(-\pi^2 k^2 w_0^2 / 2) k dk \int_0^\infty J_0(2\pi k r) \exp(-2r^2/w_1^2) r dr\end{aligned}\tag{2.17}$$

$$\Delta T(\omega) = 2\pi A A_1 \int_0^\infty \hat{G}(k, \omega) \exp(-\pi^2 k^2 (w_0^2 + w_1^2) / 2) k dk\tag{2.18}$$

The  $\frac{4A_1}{w_1^2}$  comes from the weighted average function it is the inverse of the integral of the Gaussian function, and the upper limit of the integral can be changed to  $2/(w_0^2 + w_1^2)^{\frac{1}{2}}$ , without a significant loss of accuracy [52].

The experimentally measured signal is the real part of equation (2.3),  $R(t)_{exp} = Re(R(t))$ . The thermal conductivity can be found by fitting this model to the measured data. In our experiment, for a single pulse of heating beam and continuous probe beam, the frequency should be adjusted according to the time window of our experimental measurement. In the Linseis software that we use the chosen frequency is 10 KHz in the model which corresponds to 100  $\mu s$  time window, and the used time window of the measurement is around 2  $\mu s$ , as shown in figure (2.6). The model calculations should be sufficiently accurate.

## 2.2 Extreme Ultraviolet Transient Grating Spectroscopy

### 2.2.1 Overview about Transient Grating

Four Wave Mixing (FWM) technique is based on the third order non-linear optics response. In general, the three electromagnetic fields beams are different in wavevectors ( $k_i$ ) and frequencies ( $\omega_i$ ). The beams interact with each other to produce a fourth output field, as shown in figure (2.8) [65–67].

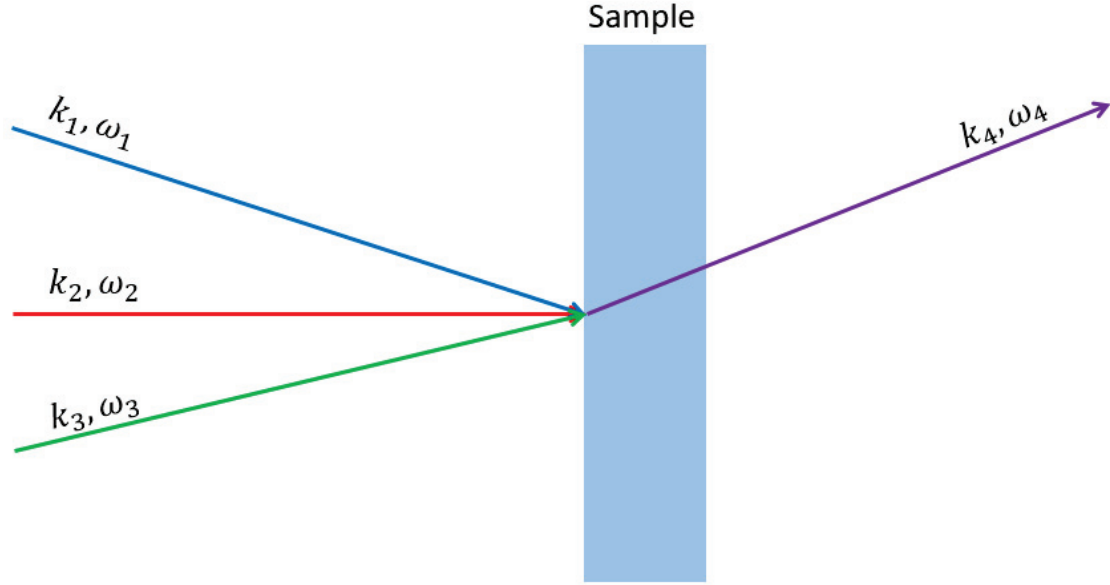


**Figure 2.8:** This figure is adapted from this thesis [68] a) Schematic representation of a general FWM process. Three input pulses with frequencies  $\omega_1, \omega_2, \omega_3$  and wavevectors  $k_1, k_2, k_3$  interact with a sample and generate a fourth signal field ( $\omega_4, k_4$ ).

A peculiar case of the FWM is the Transient Grating (TG) technique [69, 70]. In this technique, as shown in figure (2.9), the two incident fields  $k_1$  and  $k_2$ , overlapping in time and space, are incident on the sample with an angle  $2\theta$ . The frequencies of the fields  $\omega_1$  and  $\omega_2$  are equal. Interference pattern of wave vector  $Q = k_1 - k_2$  is formed by the two pulses, which are called pump beams with wavelength  $\lambda$ . The following equation gives the periodicity  $L_{TG}$  of the interference pattern, which is also called the transient grating,

$$L_{TG} = \frac{\lambda}{2 \sin\left(\frac{2\theta}{2}\right)} \quad (2.19)$$

The generated interference pattern modulates spatially with the same periodicity  $L_{TG}$  some material properties such as the density, temperature, etc. If the optical properties depend on such modulated properties, the stationary wave generated in the sample will be equivalent to a diffraction grating for the third incident field, the probe beam ( $k_{pr}$ ). The probe beam diffracts through the sample as shown in figure (2.9). The diffracted signal field has the following wavevector,

$$k_{out} = k_{pr} \pm m(k_1 - k_2) = k_{pr} \pm mQ \quad (2.20)$$

Where  $|k_{pr}| = |k_{out}|$ ,  $|k_1| = |k_2|$ , and the wave vector  $Q = 2\pi/L_{TG}$ .  $m$  is the order of diffraction. The temporal decay of the TG excitation is measured by changing the delay time  $\tau$  between the pump beams and the probe beam. The dynamics of

the excited process is carried by this time resolved signal, at a lengthscale given by  $L_{TG}$ .

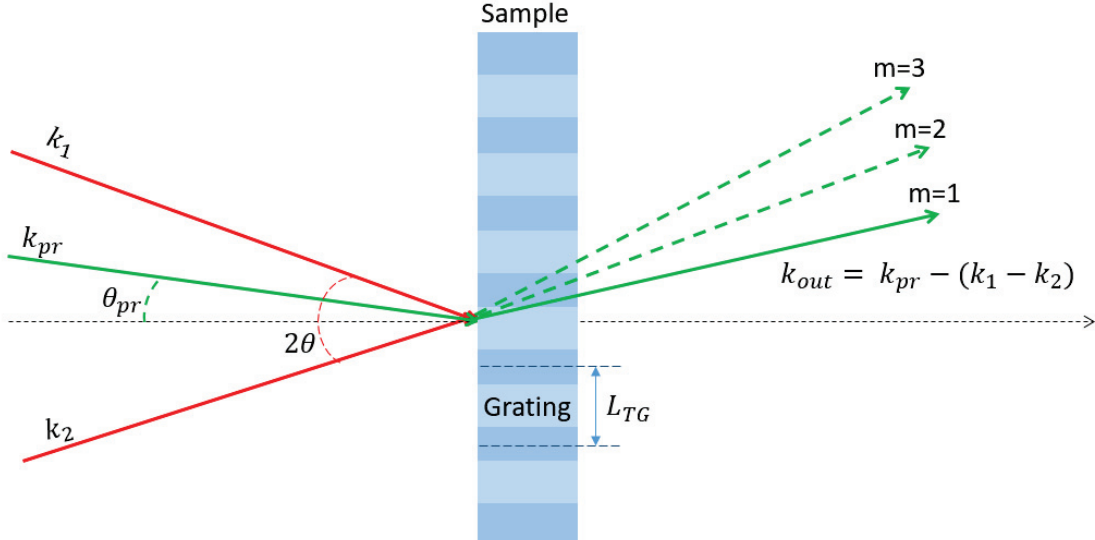


**Figure 2.9:** This figure is adapted from this thesis [68]. Scheme of a TG experiment. Two input pulses ( $k_1$  and  $k_2$ ) are overlapped on the sample, with a crossing angle  $2\theta$ , and create a transient grating with spatial periodicity  $L_{TG}$ . A third pulse ( $k_{pr}$ ), time delayed by  $\tau$ , is diffracted and results in a FWM signal emitted along  $k_{out}$ . The dashed green arrows represent higher diffraction orders ( $m > 1$ ).

## 2.2.2 Timer Beamline

TG experiments are offered in different labs with using ultra-fast lasers with different wavelengths, generating usually TG with wavelengths in the micron to sub-micron range. In our project, smaller wavelengths are achieved in TG using Free Electron laser (FEL). The used technique is at the Timer beamline of FERMI FEL in Trieste with wavelengths in the extreme ultra-violet range. This technique allows to probe phonon wavelengths in the 20-200 nm range, giving access to phonons with wavelength comparable with the nanostructuration lengthscale of this thesis work [71].

The Extreme Ultra Violet Transient Grating (EUV-TG) technique involves crossing two short FEL pump pulses, with pulse duration 150 fs and beam spot size around 100  $\mu m$ , to create a sinusoidal interference pattern which when absorbed by the sample induces a sinusoidal response [71–74]. Absorption of the pump can give raise to several mechanisms which create a transient grating [75]:

- The absorption of the pump beams in the sample causes a change in the electronic distribution of the material under study due to the temperature increase and thermal induced strain. This mechanism is called deformation potential mechanism [76].

- In non-centro symmetric materials, strain and macroscopic electric field are coupled. The pump absorption changes the electric field, inducing then a strain which is spatially modulated. This is called the Piezoelectric mechanism [77, 78].
- The electrostriction mechanism appears in transparent media. The electric field of the incident laser beam polarizes the medium which makes a deformation in the orbitals [75, 79].
- The thermoelasticity mechanism involves both temperature and elasticity of the material [75, 80]. The heating of the system comes from direct interaction with the incident pump beams. The energy excites the electrons and is then transferred to the phonons in the system. Acoustic phonons are emitted when the hot carriers interact with the phonon toward lower energy levels.

### Thermal Transient Grating

In the EUV-TG, we are interested in creating Thermal Transient Grating (TTG) in the system to measure acoustic phonons, i.e. when light is absorbed, the sinusoidal response is a temperature profile, and upon thermal expansion, an acoustic phonon is generated. This TTG is probed by a FEL beam, as a function of the delay time between the pump beams and the probe beam to measure its time decay. The probe beam is diffracted from the interference pattern, and the delay time can be changed in a time range of several hundreds of picosecond. The excitation pulse exerted by the TG changes the dielectric constant of the material. The intensity of the measured signal is proportional to the square of this change. This function can be known by solving the dynamical equation of the active modes in the system depending on the microscopic mechanisms. In our case it is the thermal response of the material [81–83]. Thus, the measured signal, for a specific periodicity  $L_{TG}$ , in EUV-TG is the intensity as a function of delay time between the pump beams and probe beam which has the following form,

$$I_{signal} \sim [A_{th} \exp(-\Delta t / \tau_{th}) + \sum_i A_i \exp(-\Delta t / \tau_i) \cos(2\pi\nu_i \Delta t)]^2 \quad (2.21)$$

Where  $A_{th}$  is the amplitude of thermal relaxation,  $\tau_{th}$  is the thermal decay time at the probed lengthscale,  $A_i$  is the phonon amplitude,  $\tau_i$  is the phonon life time, and  $\nu_i$  is the phonon frequency, the sum runs over all possible excited phonons. Figure (2.10) shows an experimental measurement of the TG in a suspended membrane of amorphous Silicon Nitride with 55 nm thickness at  $L_{TG} = 106$  nm. We can notice from this figure an oscillation superposed to a decaying intensity. The former is the phonon, the latter the thermal relaxation.

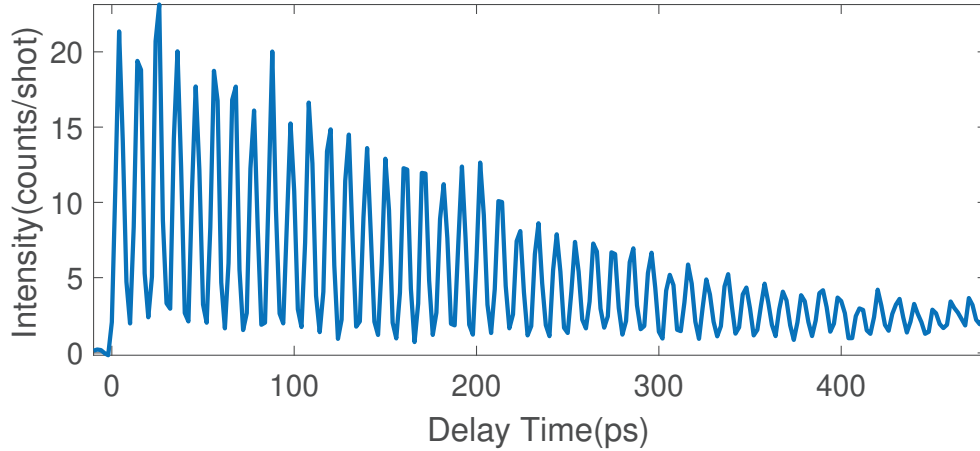


**Figure 2.10:** An example of transient grating signal measured as function of delay time between the pump and probe beams. The measured sample is a suspended membrane of amorphous Silicon Nitride with 55 nm thickness at  $L_{TG} = 106nm$ .

**Alignment and Optimization of the Signal** This experiment as shown in figure (2.11) requires alignment of three different beams to obtain a TG signal. On each sample there is a small phosphorus tape to align the beams. First there is the space and time alignment of the two pump beams, then the alignment of the sample, to be in the focal plane of the pumps and of the probe, to meet the grating within the sample. Phosphorus is used to be sure that the beams are on the same focal plane as the sample. When the fluorescence of the phosphorus is maximized, then we move on the sample to check the signal. In case a TG signal is observed, the intensity of the beams should be managed. A radiation damage can cause a permanent grating but as well the disappearance of all signal. For this reason, we check that the signal disappears if we measure at negative delay times and reappears again at positive delay times. In the negative delay time, we only have probe beam, an existence of a signal means that it is a permanent grating not a transient grating. In order to avoid radiation damage, we need to reduce the incoming intensity of the beams using filters and gas chambers in order to find the best compromise between signal to noise ratio and no-damage.

**Data Collection** Diffraction image is collected using a 2D detector. The experimental signal is analyzed by choosing a specific region around the TG signal (ROI), as shown in figure (2.11.c). At each delay time the intensity within the ROI is integrated giving the signal. Regularly, we collect background images, i.e. without pump nor probe, which are used to subtract the background from the signal as a function of time. The closest-in-time background image is used for every experimental point. At the same time these background images allow us to check if ever a permanent grating appears, which would show up in an increasing

background intensity.

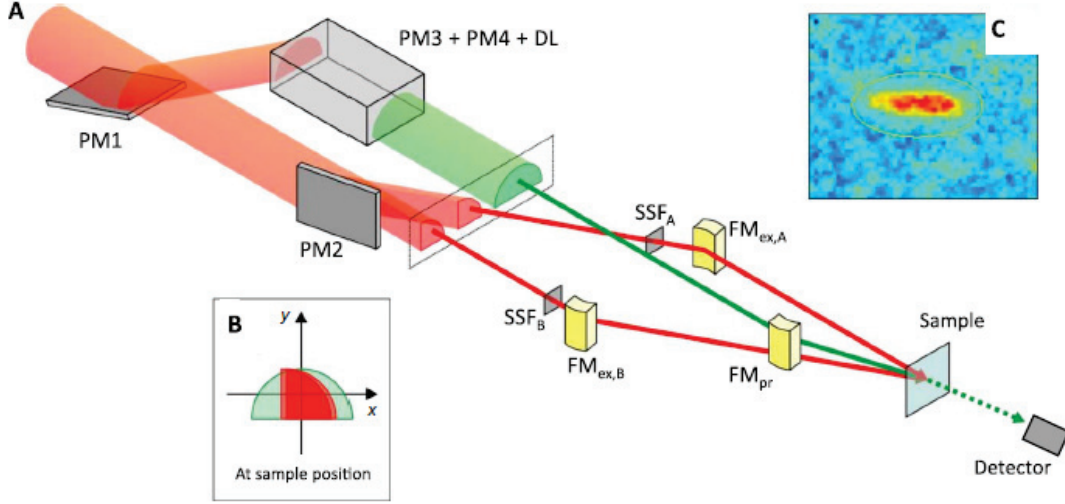


**Figure 2.11:** Experimental setup adapted from article [71] a) Scheme of the beamline layout. PM = plane mirror, DL = delay line, SSF = solid-state filter, FM = focusing mirror. b) Sketch of the splitted beams, overlapped at the sample position. c) Example of the signal recorded by the detector.

**Data Integration for Weak Signal** During my PhD I performed 3 EUV-TG experiments, both in reflection and transmission geometry. In the former case, the signal turned out to be very weak, and of the same order of magnitude as the background. I developed an improved background estimation and subtraction procedure, optimized for very weak signals. Using directly the CCD image of the signal, I extrapolated the background within the ROI using the intensity values out of the ROI and their spatial dependence along rows and columns of the CCD. The method works reasonably well. A copy of this code is shown in the appendix [A](#).

**Data Analysis** The procedure described in this section is a general method for the analysis [71] of the measured transient grating signal as a function of delay time, as shown in figure (2.10). The first step is to fit the data with an exponential decay of form  $A \exp(-\Delta t/B)$ , the main aim of this fit is to have an idea about the thermal decay time, and to subtract the fitted data from the mode to have a transient grating signal that mostly describe the phonon dynamics in the system. The fitted values  $A$  and  $B$  are related to amplitude of thermal relaxation ( $A_{th}$ ) and the thermal decay time ( $\tau_{th}$ ) described in equation (2.21) as following  $A = A_{th}^2$  and  $B = -\tau_{th}/2$ . The fitted model is subtracted from the transient grating signal, then a Fourier transform is performed to the subtracted data to quantify the different modes in the system. In the investigation of the phonon dynamics

in the material, the transient grating signal is fitted to equation (2.21) where the number of modes in the equation is quantified from the Fourier transform, the initial guess of the thermal amplitude and thermal relaxation times is clarified from the fitting of the data to the thermal decay, and the phonon frequency from the Fourier transform. The main aim of this fit is to investigate the phonon life time and phonon frequency in the system under study.

## Chapter 3

# Silicon Nitride (IPPON)

Amorphous silicon nitride ( $\text{a-SiN}_x$ , with  $0 < x < 1.33$ ) thin films are suitable for applications in a very large panoply of technologies due to their appealing physical, chemical, structural, optical and electrical properties. It is largely used as gate insulators in thin film transistors [84–86], and dielectric stacks of integrated circuits, as passivation or capping layers [87]. This material has become an important alternative to silicon in integrated nonlinear optical applications such as waveguides [88], and it is at the focus of research for photonic architectures in energy harvesting applications [89]. Tuning the nitrogen content allows one to tune its properties, and specifically its band gap, so that  $\text{a-SiN}_x$  thin film is a very attractive material with manageable vibrational, electrical and optical properties [90–93].

Still, the very same variability of these properties represents a technical challenge, as it strongly depends on the growth technique used and the resulting film morphology, texture, and chemical composition, which are not always perfectly mastered. The growth of  $\text{a-SiN}_x$  thin films can be made with different techniques and conditions which lead to quite different materials, with a large variability in properties such as density, elastic moduli, intrinsic stress and thermal conductivity. Among such techniques, the one of choice for the preparation of  $\text{SiN}_x$  for electronic and optic devices is the Plasma Enhanced Chemical Vapor Deposition (PECVD), which has the advantage of growing the material at low temperature. Here as well, however, the choice of the growth parameters, such as the deposition temperature, the radio-frequency, and the plasma pressure, can dramatically affect the properties of the deposited film [94, 95]. Such large variability comes not only from the morphology or the exact Si:N ratio, but as well from an often uncontrolled content of hydrogen, which is bounded to both Si and N. Indeed, it has been reported that hydrogen is almost always present and its content and relative amount of the two types of bonds significantly affect the structural, electrical and mechanical properties of the thin film [96, 97]. A panoramic of the different physical properties of  $\text{SiN}_x$ , depending on the growth technique, can be found in two recent reviews from Kaloyeros et al. [98, 99].

In our project, in order to evidence the effect of the nanostructuration on thermal transport in amorphous SiN thin film, it is primordial to first investigate the thermal conductivity in a homogeneous, non nanostructured, sample. The first thermal conductivity measurements of the amorphous SiN<sub>x</sub> thin film as a function of temperature have led to unexpected results which have motivated us to perform deeper investigations. Thus, in this chapter, we present a detailed study of the thermal conductivity in amorphous SiN<sub>x</sub> as a function of temperature and for different deposition temperature.

### 3.1 Samples

Amorphous SiN<sub>x</sub> materials have been deposited by Plasma Enhanced Chemical Vapor Deposition (PECVD) on Silicon substrate using a 200 mm OXFORD Plasmalab 80+ PECVD system. SiH<sub>4</sub> 4% in He, NH<sub>3</sub>, Ar and N<sub>2</sub> were used as reactive gases plasma mixture. Plasma gases were adjusted with SiH<sub>4</sub>/He = 80 sccm, Ar = 200 sccm, NH<sub>3</sub> = 10 sccm and N<sub>2</sub> = 600 sccm. 13.56 MHz RF power was held at 70 W under a pressure of 1.2 Torr. Temperature of deposition was varied from 298 K to 573 K. Pre-conditioning of the deposition chamber was operated during 5 minutes before each introduction of sample. The samples were prepared by our colleagues at the Institute of Nanotechnology of Lyon (INL) in the context of the IPPON project.

### 3.2 Thermal Study of Amorphous Silicon Nitride thin films

In this thesis work, we are interested to thermal transport properties and vibrational dynamics of PECVD SiN. Here we give a brief overview of previous studies of thermal conductivity of a-SiN depending on the growth technique. Thermal conductivity of amorphous silicon nitride (a-SiN<sub>x</sub>, with  $0 < x < 1.33$ ) is strongly dependent on the growth method and the thickness [100]. This dependence has been studied throughout the years by different groups. CVD SiN thermal conductivity was found to decrease with temperature between 300 and 523K, with a room temperature value between 0.04 and 1.6 W/mK, depending on the film thickness (0.06-8.5  $\mu\text{m}$ ) [101]. Zhang et al measured the thermal conductivity of free standing LPCVD SiN, which turned out to be quite larger, between 9 and 13 W/mK. In contradiction with these results, 1.4 and 0.6  $\mu\text{m}$  thin films have showed higher values of conductivity corresponding to 9 and 13 W/m.K, respectively [10]. In-plane thermal conductivity has been reported to be  $4.9 \pm 0.7$  W/m.K for 1.5  $\mu\text{m}$  thinfilm [102, 103], and 2.8 W/m.K for 100 nm thin film [104]. Finally, Lee et al. measured the thermal conductivity of a-SiN<sub>x</sub> of density 2.2 g/cm<sup>3</sup>, grown by PECVD at 573 K, from 78 K up to 400 K by  $3\omega$  method finding that it is of

only about 0.7 W/mK at room temperature and increases with temperature [56]. PECVD appears then to be the growth technique which guarantees the lowest thermal conductivity, which is indeed of interest for many applications.

### 3.2.1 Effect of the Annealing Temperature on the Physical Properties of $\text{SiN}_x$

Different properties of the silicon nitride thin film can be irreversibly modified by annealing of the thin film. Hughey et al. [105] have measured the film stress during thermal cycling of amorphous Silicon Nitride thin film on Si and InP substrates as shown in figure (3.1). The films are grown by PECVD at 120 °C and 320 °C. In the range 28-300 °C, samples on different substrates show reversible change of stress during cooling. However, when heating exceeds 300 °C, an irreversible change of the thin film stress appears. Hughey et al. [105] understood that it is related to a chemical reaction of hydrogen bonded molecules (Si-H or N-H) to form molecular hydrogen (Si-Si or Si-N). They also observed a significant decrease of hydrogen level from (17-20 %) to (1.5-2 %) after annealing [105].

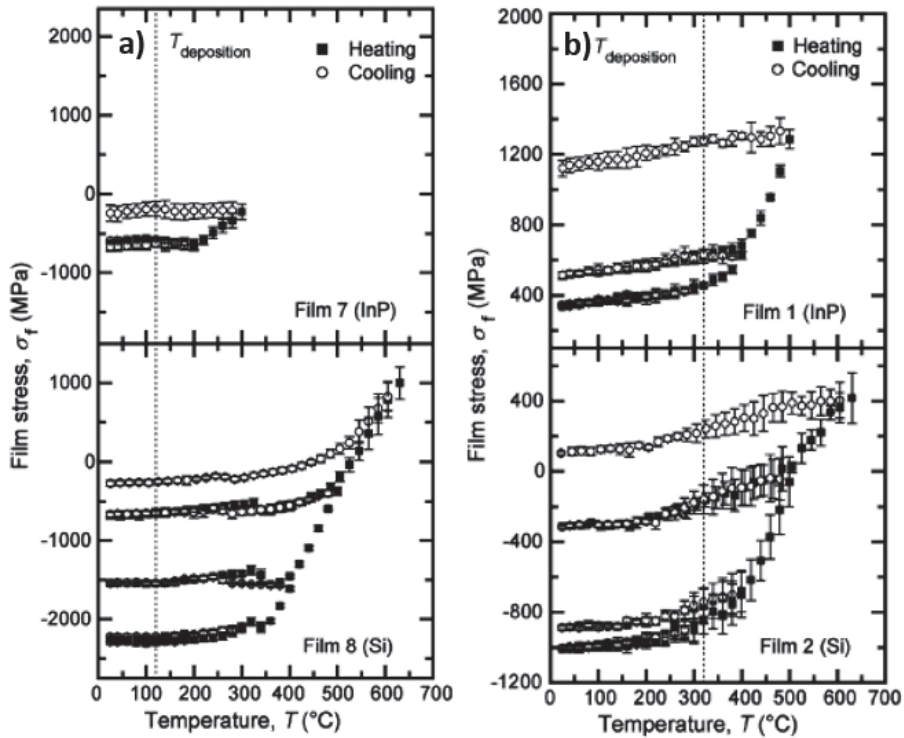


**Figure 3.1:** This figure is taken from Hughey et al. [105]. a) and b) The film stress measurement during thermal cycling for Silicon nitride thin films grown on Si and InP substrate by PECVD at different growth temperature 120 °C and 320 °C, respectively [105]. The growth temperature is indicated by a vertical dotted line.

Maeda et al. observed the variation of the absorption coefficient of Si-H and N-H bonds measured by FTIR (Fourier Transform Infrared Spectroscopy), as shown in figure (3.2.a), as a function of the annealing temperature [106]. The absorption coefficient of Si-H increased in the range of 400-500 °C and that of N-H decreased in the same range of temperature. The previously mentioned increase is due to the formation of new Si-H bonds from the broken N-H bonds showing that the N-H bond is weaker than the Si-H bond [106,107]. They also studied the variation of the FTIR absorption coefficient of each bond as a function of the annealing time at different annealing temperatures as shown in figures (3.2.b) and (3.2.c), evidencing that there is a slow kinetics in the bond evolution.

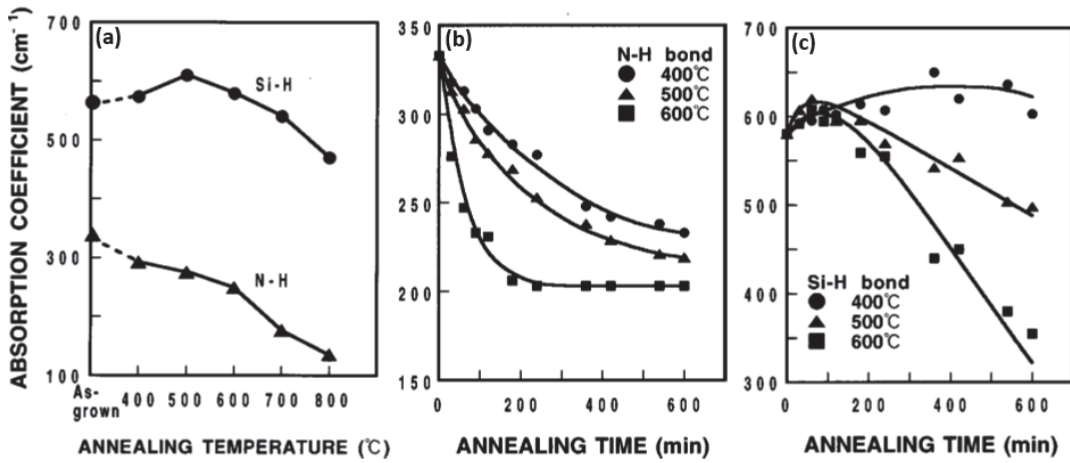


**Figure 3.2:** This figure is taken from Maeda et al. [106] a) The variation of the FTIR absorption coefficient of Si-H and N-H bonds as a function of the annealing temperature. b) and c) The variation of the FTIR absorption coefficient of Si-H and N-H bonds, respectively, as a function of the annealing time at different annealing temperatures [106].

### 3.2.2 Room Temperature Measurement

The thermal conductivity of the thin film is measured by fitting the experimental data to Cahill model [52], the fitting parameter is the thermal conductivity of the thin film. Measured samples of a-SiN<sub>x</sub> have different thicknesses (200, 292, and 501 nm) on either Silicon or Silica substrate. The thermal conductivity at room temperature has been measured at five different positions on the sample. The final value, reported in table (3.1), is the average of the 5 measurements, the error is their standard deviation. There is a good agreement between literature values [56] and measured ones for the silicon substrate with different thicknesses and the Silica substrate with 501 nm thickness only. The experimental thermal conductivity measurement confirms the sensitivity study of the thermal conductivity of a-SiN<sub>x</sub> on Silica substrate. As shown in figure (3.3), in the case of Silica

substrate, the sensitivity peak to the thermal conductivity of a 200 nm a-SiN<sub>x</sub> thinfilm strongly overlaps with the sensitivity peak to the thermal conductivity of the Silica substrate, but this latter, in the case of thinfilm of 500 nm of a-SiN<sub>x</sub>, is shifted at longer times. This allows to find a time window where the signal is dominated by the thermal relaxation of a-SiN<sub>x</sub>. This is why for 200 nm and 292 nm the estimation is not reliable, while it is for 501 nm thickness. In the case of Silicon substrate, as shown in figure (3.4), the sensitivity peaks to the thermal conductivity of the Silicon substrate is shifted at longer time in the range of 200-500 nm thin film thickness of a-SiN<sub>x</sub>, this is the reason behind the accurate measurement of thermal conductivity of a-SiN<sub>x</sub> thin film on Silicon substrate.

Substrate	a-SiN <sub>x</sub> thickness (nm)	Thermal conductivity (W/m.K)
Silicon	200	0.66±0.01
Silicon	292	0.669±0.008
Silicon	501	0.68±0.02
Silica	200	0.48±0.02
Silica	292	0.46±0.03
Silica	501	0.68±0.02

**Table 3.1:** Thermal conductivity data measurement at room temperature on a-SiN<sub>x</sub> thin film samples grown by PECVD at 573 K.

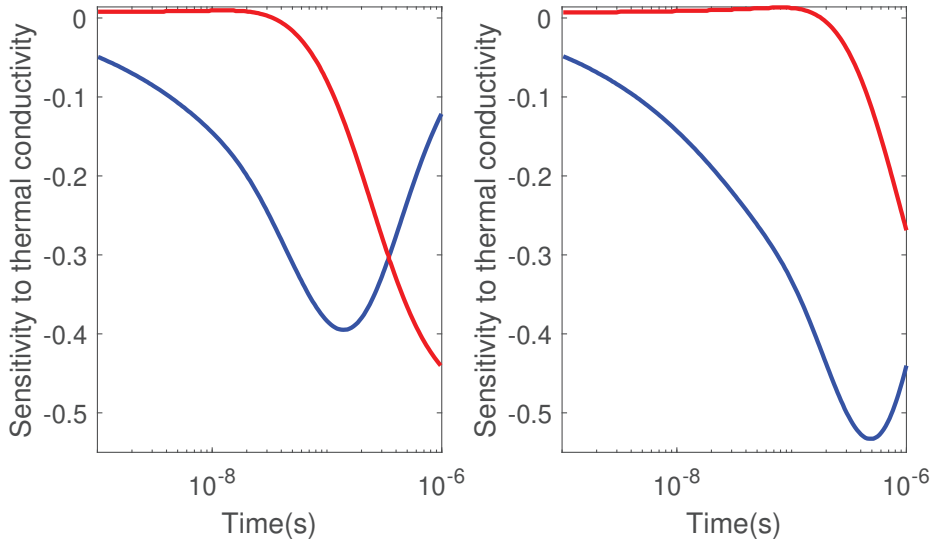


**Figure 3.3:** The sensitivity to thermal conductivity of the thin film of a-SiN<sub>x</sub> (blue line) and the substrate Silica (red line). The left figure is for 200 nm of a-SiN<sub>x</sub> and the right figure is for 500 nm of a-SiN<sub>x</sub>.

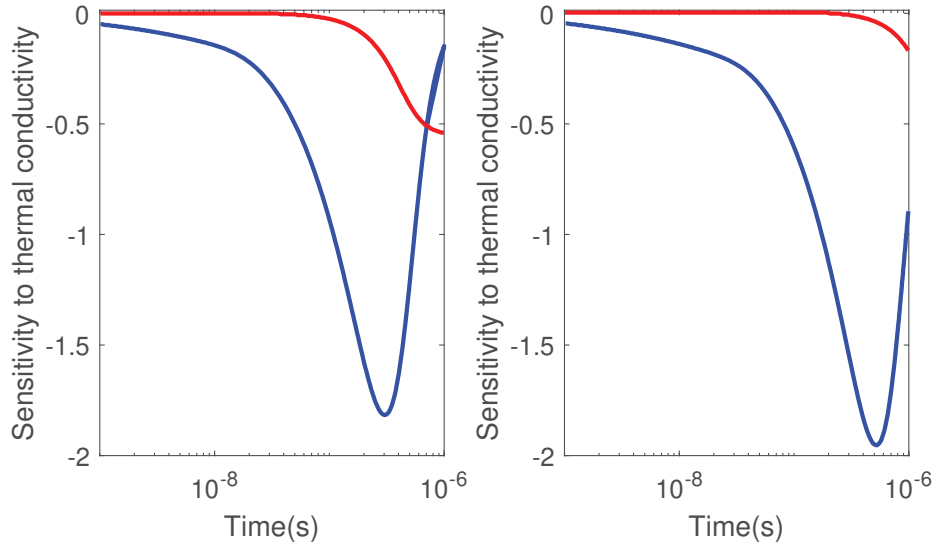


**Figure 3.4:** The sensitivity to thermal conductivity of the thin film of a-SiN<sub>x</sub> (blue line) and the substrate Si (red line). The left figure is for 200 nm of a-SiN<sub>x</sub> and the right figure is for 500 nm of a-SiN<sub>x</sub>.

### 3.2.3 High Temperature Measurement

The thermal conductivity was first measured on a sample grown at 573 K. The procedure for measuring at a high temperature is to measure in the temperature range from 300 K up to 773 K along isotherms with a step of 50 K. At each temperature step a sufficient amount of time is needed for temperature stabilization. At each temperature the measurement is performed on 8 different positions on the sample. The average and standard deviation are then calculated. The sample is cooled to room temperature, this is the first annealing. The same procedure is followed for the second annealing.

In the figure (3.5.a), the temperature dependence of the thermal conductivity is reported upon heating of a 292 nm thick SiN<sub>x</sub> sample deposited on silicon at a deposition temperature of 573 K, as representative for all measured thicknesses, the overall behavior being similar among all the films. First of all, the room temperature values,  $k_{300K} = 0.63 \pm 0.03 \text{ W.m}^{-1}\text{K}^{-1}$  (on the as-grown) and  $k_{300K} = 0.7 \pm 0.032 \text{ W.m}^{-1}\text{K}^{-1}$  (after the first annealing ramp), are consistent with the  $\sim 0.7 \text{ W.m}^{-1}\text{K}^{-1}$  reported by Lee [56] on a 252 nm PECVD SiN<sub>x</sub> film deposited at the same temperature, with  $\rho = 2.2 \text{ g/cm}^3$ . On the other hand, Lee reports an increasing thermal conductivity with temperature, which slightly flattens above 400 K. While this report should be confirmed by properly taking into account the interface thermal resistance, we can at least say that above 300 K, we don't observe an increase in thermal conductivity, but a decrease with temperature. On the first heating ramp,  $\kappa(T)$  decreases linearly upon heating from 300 K to

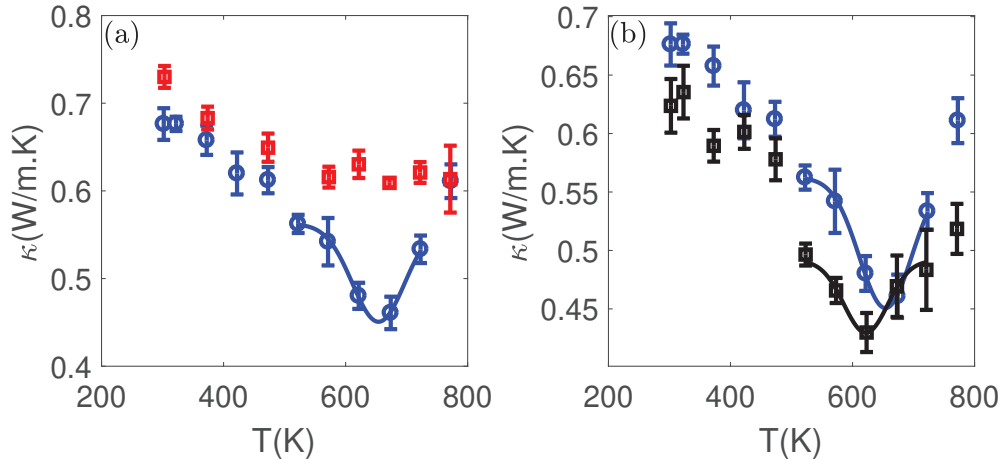


**Figure 3.5:** (a): Thermal conductivity ( $\kappa$ ) of a 292 nm thick  $\text{SiN}_x$  sample deposited on Si, reported as a function of temperature ( $T$ ) during the very first heating ramp on the as-grown sample (blue circles) and during a second heating ramp run after the very first one (red squares). (b) Thermal conductivity on 501 nm thick  $\text{SiN}_x$  deposited on Si (blue circles) and  $\text{SiO}_2$  (black filled squares), reported as a function of temperature during the very first heating ramp. All error bars correspond to the standard deviation of the distribution of values obtained from 8 different measurements at each temperature.

450 K and then drops abruptly down to a minimum of  $\sim 0.45$  W/mK at 673 K, before increasing again. This behavior is very specific to the first heating ramp indicating that it results from an irreversible modification of our sample. Upon a second annealing,  $\kappa(T)$  exhibits a linear decrease up to  $\sim 450$  K following almost the same slope as for the first heating ramp and then saturates at higher temperature. This latter behavior of  $\kappa(T)$  is then reproducible if the sample is annealed again.

The presence of this minimum is quite intriguing. A first possibility is that it is an artefact due to a non-correct account for thermal interface resistance. To rule out this hypothesis, we have performed the same study on a sample deposited on a  $\text{SiO}_2$  substrate, in order to have different interfaces at play, as well as a different contribution from the substrate to the total thermal relaxation. Due to the different stacking, a thicker  $\text{SiN}_x$  layer is needed for a reliable extraction of its thermal conductivity. We report in figure (3.5.b) the measurement of  $\kappa(T)$  on 501 nm thick samples deposited on Si and  $\text{SiO}_2$ . If for  $\text{SiN}_x$  on  $\text{SiO}_2$  the absolute value is slightly smaller, the same temperature dependence is reproduced, with a slight downshift of the minimum position, which is found at 623 K.

Once assessed that the peculiar temperature dependence is real and an intrinsic property of our PECVD  $\text{SiN}_x$ , it is interesting to see how it depends on the deposition temperature. We first report in figure (3.6) the measured room temperature thermal conductivity ( $\kappa_{300K}$ ) as a function of the deposition temperature ( $T_{dep}$ ).

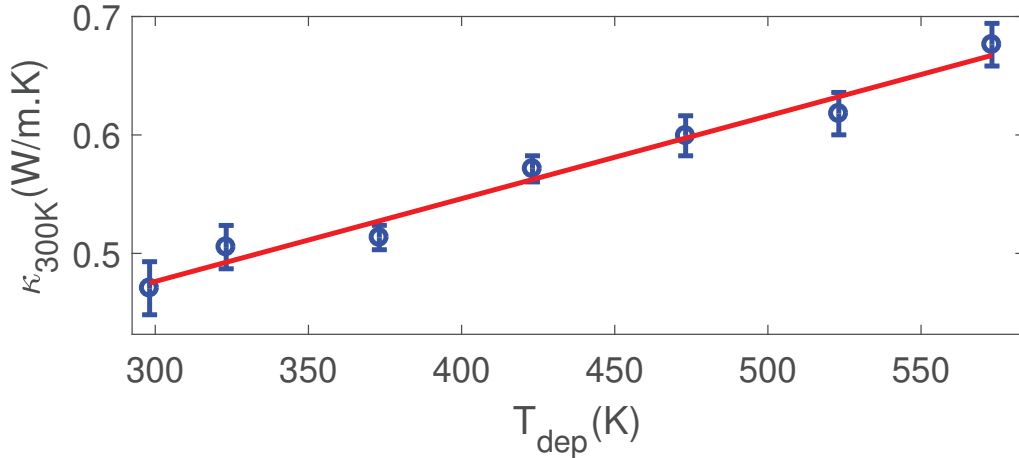


**Figure 3.6:** Room temperature thermal conductivity ( $\kappa_{300K}$ ) of  $\text{SiN}_x$  on Si grown by PECVD as a function of the deposition temperature ( $T_{dep}$ ). The error bars correspond to the standard deviation of the distribution of values obtained from 8 different measurements at each temperature. The solid black line is a linear fit.

$\kappa_{300K}$  increases with deposition temperature with a linear rate of change of  $0.27 \pm 0.02 \text{ W/m.K}^2$ . Despite this, the global temperature dependence during the first annealing is found to be the same in all samples, independently on the deposition temperature, as can be observed in figure (3.7.a), where we report  $\kappa(T)$  in all samples during the first annealing (data have been vertically shifted for optical convenience). The same curves are reported in figure (3.7.b) after normalization to the respective room temperature value.

It may be seen that in all samples  $\kappa(T)$  undergoes a first linear decrease in the 300 K - 450 K temperature range followed by a drop, a minimum and an increase at higher temperatures. The slope of the first linear decrease is found to increase with the deposition temperature by a factor as large as  $\sim 50\%$  at the highest deposition temperature, going from  $-0.39(9) \text{ mW/m K}^2$  at  $T_{dep} = 298 \text{ K}$  to  $-0.61(4) \text{ mW/m K}^2$  at  $T_{dep} = 573 \text{ K}$ . Then, starting from  $\sim 500 \text{ K}$ , a steeper decrease leads to the minimum before increasing almost up to the room temperature value. The position of the minimum weakly increases with deposition temperature from  $\sim 600 \text{ K}$  at  $T_{dep} = 298 \text{ K}$  to  $\sim 654 \text{ K}$  at  $T_{dep} = 573 \text{ K}$ , keeping its depth essentially the same for all samples (see figure 3.7.(b)). In all cases the minimum disappears for further annealings.

Our results indicate that the presence of the minimum does not depend on the microstructure of our PECVD  $\text{SiN}_x$ , nor the specific density and elastic constants, which depend on the deposition temperature. It is the result of an irreversible process which is thermally activated at about the same temperature for all samples, around 500 K. The question arises whether the measured values at each temperature are equilibrium values or whether they would evolve, if given time enough.

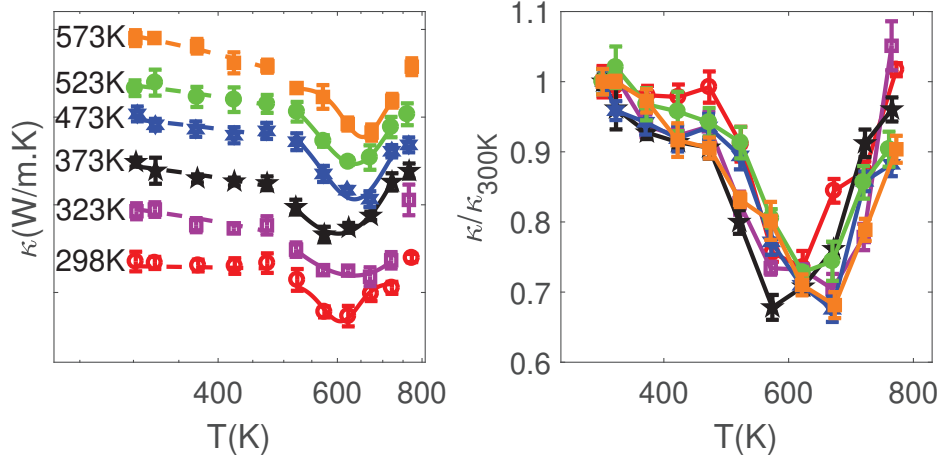


**Figure 3.7:** (a) Thermal conductivity ( $\kappa(T)$ ) as a function of temperature ( $T$ ) during the very first heating ramp of samples deposited on Si at different temperatures. The deposition temperature is indicated next to each curve. Dashed lines follow the linear decrease in the first temperature range, solid lines mark the shape of the minimum (b) The same curves in (a) are here reported after normalization to the room temperature value. The color/symbol legend is the same as in (a). The error bars correspond to the standard deviation of the distribution of values obtained from 8 different measurements at each temperature.

In other words: once we are in the minimum, does the system need additional thermal energy to get out of it, or does it indefinitely remain there? In order to answer this question, we have heated a  $\text{SiN}_x$  sample grown at  $T_{dep} = 573$  K up to the position of the minimum, 673 K, and we have followed the time evolution of its thermal conductivity at 20 min time steps. We report these data in figure (3.8). It may be seen that thermal conductivity increases in time, relaxing back to the equilibrium value, which corresponds to the one which can be found during a second annealing. 100 minutes are needed for the full relaxation, and then the thermal conductivity remains constant for the next 300 minutes, indicating that no other process is active at this temperature. The relaxation time constant can be estimated by fitting the data to an exponential function, and it results in  $\tau = 70 \pm 10$  min. It is worth noticing here that the existence of kinetics active on the 20 minutes time scale may explain the little modifications of the minimum shape and position through the different samples, as we did not use the same thermalisation time in all samples.

## Discussion

First of all, we shall comment on the dependence of the room temperature thermal conductivity on the deposition temperature. The observed increase can be due to a smaller porosity of  $\text{SiN}_x$  when deposited at higher temperatures, as reported in

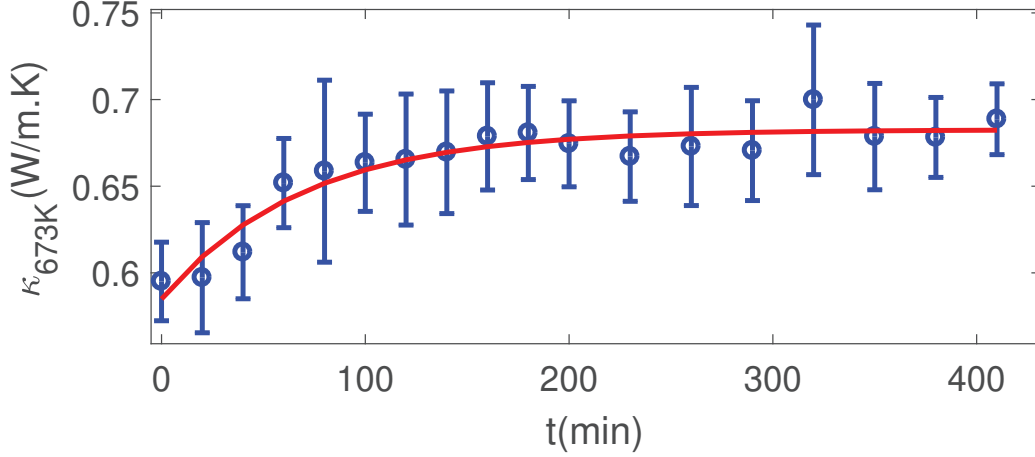


**Figure 3.8:** The measured thermal conductivity of  $\text{SiN}_x$  on Si grown by PECVD at 523K heated to 673K as a function of time. The red line is the fit of the data to an exponential function. The error bars correspond to the standard deviation of the distribution of values obtained from 8 different measurements at each temperature.

the literature [108, 109], so that we can model our material as effectively composed of  $\text{SiN}_x$  and micropores [108]. The effective medium theory allows to estimate the expected thermal conductivity of a porous medium from the zeros of the function

$$(1 - x) \frac{k_1 - k_e}{k_1 + 2k_e} + x \frac{k_2 - k_e}{k_2 + 2k_e} = 0 \quad (3.1)$$

where  $k_1, k_2, k_e$  and  $x$  are the thermal conductivity of non porous  $\text{SiN}_x$ , pores and the effective thermal conductivity of the porous medium respectively and  $x$  is the pores volume fraction [110]. As we don't know the thermal conductivity of an equivalent non-porous  $\text{SiN}_x$ , we use  $k_1 = 0.7 \text{ W/mK}$  for estimating how much porosity should change for giving the observed thermal conductivities. For pores, we take  $k_2 = 0$ . Using the measured thermal conductivity values at room temperature, we obtain pores volume fractions ranging from 3% up to 24% from the highest to the lowest deposition temperature. Such a large change in porosity is however not compatible with the measured weak density change, which is at most 4%. This could be explained by the limitations of the model, which does not take into account the additional thermal resistance introduced by the  $\text{SiN}_x$  pore interfaces. Still such a strong difference in the porosity estimated from density and from thermal conductivity points to another origin for the large change in this latter.

As we have seen, the chemical structure evolves with the deposition temperature: oxygen content decreases and Si-N bonds increase.  $\text{SiN}_x$  being a dielectric, the main heat carriers are the atomic vibrations, whose quasi-particle is the phonon. Not only the interfaces can scatter phonons, but also the atomic defects in the Si-N network, such as oxygen and hydrogen bonds. Decreasing their content means

decreasing scattering from defects, leading thus to larger thermal conductivities. Moreover, the Si-N bond content increasing with deposition temperature, the elastic constants are expected to increase as well, due to the higher rigidity of this bond, and indeed an increase of the Young modulus by a factor of 2 has been reported in literature for deposition temperatures between 373 and 573 K [109]. From the kinetic theory for a phonon gas, the thermal conductivity reads  $k_T = \frac{1}{3}C_v vl$ , with  $C_v$  the specific heat,  $v$  the sound velocity and  $l$  the phonon mean free path. Considering that the longitudinal and transverse velocities are given by  $v_{L/T} = \sqrt{M_{L/T}/\rho}$  with  $M_{L/T}$  the longitudinal and shear elastic modulus and  $\rho$  the mass density, we expect the thermal conductivity to increase with the square root of the elastic moduli. A rough estimation using the Young moduli reported in the literature gives a change of the thermal conductivity by a factor of  $\sim 50\%$  between 373 and 573 K, which well corresponds to the observed increase.

Second, we shall comment on the unusual decrease with temperature of the thermal conductivity, independent on the deposition conditions. Actually, this is opposite to what is usually observed in amorphous materials, where thermal conductivity at high temperature increases due to the increase of the specific heat, while the phonon mean free path is almost constant at its minimum value. Our results would indicate that in our sample, at temperatures for which the specific heat has basically reached the Dulong Petit limit, the phonon mean free path decreases with temperature. It is in fact a very weak decrease, as the slope of the thermal conductivity is in the  $0.4\text{-}0.6 \cdot 10^{-3} \text{ W/mK}^2$  range for an absolute value of about  $0.7 \text{ W/mK}$ . Such behavior, absent in amorphous materials with a stable composition, could likely be related to the presence of impurities such as oxygen and hydrogen in our sample, which diffuse with temperature, causing a rearrangement of the atomic bonds in the Si-N network. Further studies are needed to confirm this hypothesis and track the origin of this unusual behaviour.

We come now to the presence of a minimum in the thermal conductivity during the first annealing, at  $\sim 673 \text{ K}$ , which disappears in the second annealing ramp in all samples, independent on deposition temperature and substrate. A possible origin of this behavior is that our amorphous  $\text{SiN}_x$  starts crystallizing at high temperature. However, the crystallization temperature in PECVD  $\text{SiN}_x$  has been reported to be much larger,  $\sim 1148 \text{ K}$  [111]. Moreover, even if some incipient crystallization were present, this should lead to an increase of the thermal conductivity, being the one of the crystalline phase about  $26 \text{ W/mK}$  [99]. A second possibility is the activation of a temperature induced structural relaxation. The higher temperature induces higher atomic mobility, which can lead to slight atomic rearrangements, responsible for the evolution of elastic and thermal properties. This is expected to have a role for temperatures larger than the deposition temperature, thus we would expect the steep decrease of the minimum to appear at lower temperatures for lower deposition temperatures. This is however not the case. Moreover, in case of structural relaxation, we would expect a monotonic and asymptotic behavior, from the unrelaxed to the more relaxed state, while

here we face a steep decrease followed by a similarly steep increase back to an unperturbed value.

In fact, the observed phenomenology resembles to a temporary thermally induced perturbation of our system: thermal transport is progressively hindered by some temperature-activated mechanism and then comes back to the unperturbed behavior when the mechanism is over. Being this phenomenon independent on deposition temperature, we cannot expect it to be related to the presence of oxygen nor the amount of Si-N bonds, which depend both on this latter. On the other hand, we also know that there is hydrogen in our sample, both bound to Si and N, and under a non-bonded molecular form, trapped within the porous structure [112], and we could not see important differences among samples deposited at different temperatures. In order to see whether hydrogen could be responsible for the minimum in the thermal conductivity, we have measured the FTIR spectrum of our  $\text{SiN}_x$  deposited at 573 K before and after the annealing, but we could find indication of only a very slight decrease of the Si-H and N-H bonds content, as shown in figure (3.9). Still, FTIR is sensitive only to bounded hydrogen, so that we cannot rule out an effect of the molecular  $\text{H}_2$ .

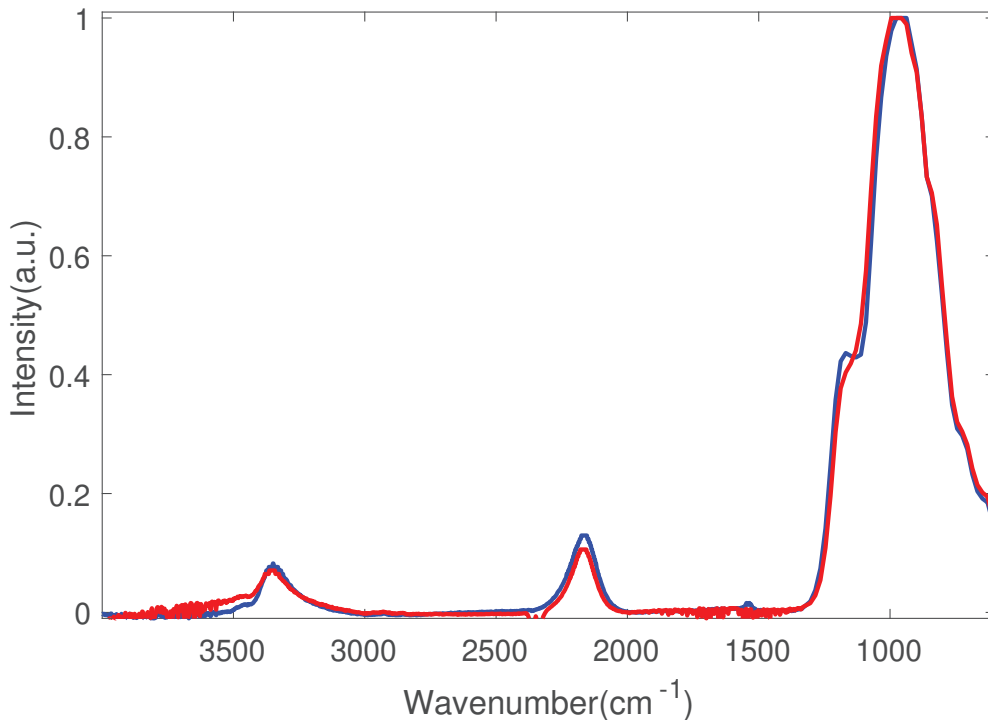


**Figure 3.9:** FTIR spectrum is reported for  $\text{SiN}_x$  before (blue line) and after (red line) for 2 hours annealing at 773 K which is corrected and normalized to their maximum intensity

An exhaustive study of the hydrogen effusivity as a function of temperature in PECVD  $\text{SiN}_x$  deposited at 673 K with different stoichiometries has been reported by Jafari et al. [112]. It is found that, starting from 673 K, the thermal energy is enough to break first the N-H bond and then, above  $\sim 973$  K, the more energetic Si-H bond, so that all hydrogen diffuses out of the sample between 673 and 1273 K. Interestingly, for N-rich compositions, a small peak appears in the hydrogen effusivity, with a maximum between 650 K and 670 K depending on the N content, accounting for about the 2-5% of the total hydrogen effusivity signal. This peak has been ascribed to the premature release of hydrogen from surface desorption of  $\text{H}_2$  molecules, non detectable by FTIR spectroscopy. The correspondence of the temperature range, as well as the similar peak shape points to the diffusion and release of molecular hydrogen as the cause of the observed minimum in the thermal conductivity. The  $\text{SiN}_x$  matrix with freely moving  $\text{H}_2$  can be assimilated to the case of a superionic material, where some atoms are characterized by a liquid-like mobility. In these latter, the active ions movement may enhance phonon scattering, due to disorder and anharmonicity, as reported in the high temperature super-ionic phase of  $\text{CuCrSe}_2$  [113]. We may expect a similar phenomenology here. In our case the large  $\text{H}_2$  mobility is limited to the temperature - or time at a given temperature - range within which all the molecular hydrogen diffuses out of the sample, thus the perturbation on thermal transport disappears once all the molecular hydrogen has left, being an irreversible process. The peak shape can be understood as due to a scattering probability proportional to the amount of mobile  $\text{H}_2$ . The fact that we find a similar shape, and more specifically depth, of the minimum throughout all samples may indicate that the quantity of mobile  $\text{H}_2$  is quite insensitive to the deposition temperature, or that there is a saturation effect.

## Conclusions

We have here reported an exhaustive investigation of the thermal conductivity of PECVD  $\text{SiN}_x$  thin films as a function of the deposition temperature, all other growing parameters being kept constants. A strong variation of the room temperature value, of a factor of almost 2, is found as a function of the deposition temperature, likely related to the increase of the Si-N bonds content, and thus a larger rigidity of the amorphous network at higher deposition temperature. Our data can explain the panoply of results on thermal conductivity reported in the literature, measured on samples grown in different conditions, and can help in aiming the best deposition temperature for the foreseen application, on the basis of the needed thermal properties. Moreover, we find that, independently on the deposition temperature, thermal conductivity weakly decreases with temperature, at odds with other reports [56], and with the usual behaviour of amorphous materials. We have tentatively ascribed such dependence to a slightly decreasing phonon mean free path with temperature, due to the presence in our samples of

oxygen and hydrogen impurities, whose diffusion can be promoted by the temperature and lead to atomic bonds reorganization. Further investigations are needed to confirm such hypothesis. Interestingly, we have observed the onset of an irreversible process at  $\sim 500$  K, leading to a minimum of the thermal conductivity at about 673 K, before it increases back to the unperturbed value. This peculiar behavior does not depend on the deposition temperature, indicating that porosity, Si-N bonds and oxygen bonds are not responsible for it. Instead, we can explain it as due to a premature release of molecular hydrogen, whose diffusivity is temperature-activated at about the same temperatures [112]. The shape of the minimum and its irreversibility can be understood in terms of an enhanced phonon scattering from mobile  $H_2$ , which is proportional to the content of this latter. Once all the mobile  $H_2$  molecules have left the sample, the process is over and the thermal conductivity comes back to the unperturbed value. Our results assess the stability of the temperature window in which the phenomenon takes place, and the important effect on the thermal conductivity, which decreases by 30%, together with its relatively long time constant ( $\sim 20$  minutes). For higher temperatures, such as Si-H and N-H bonds break down and all hydrogen diffuses out of the sample, we may expect even larger effects, as well as an irreversible absolute modification of the thermal conductivity once these point defects have been annihilated. Our findings indicate that in order to use  $SiN_x$  in electronic or optic applications, when application temperature is larger than 500 K, a preliminary annealing up to 723 K is fundamental for assuring its thermal stability. For application temperatures larger than 723 K, much higher annealing temperatures will be needed to get rid of all the bound hydrogen. Finally, we stress here the high sensitivity demonstrated by PECVD  $SiN_x$  thermal conductivity with respect to mobile hydrogen, which can open the way to its use to monitor hydrogen diffusion, and possibly to the application of PECVD  $SiN_x$  as membranes for hydrogen stocking and release.

### 3.2.4 Low Temperature Measurement

In this part, we investigated the thermal conductivity at low temperature down to 183 K, as shown in figure (3.10). The samples measured are grown by PECVD at different deposition temperatures (323 K, 373 K, 473 K, and 523 K). We report as well measurements by Lee et al. [56] on PECVD  $SiN_x$  on the temperature range from 80 K to 400 K. First of all, we notice that our data deposited at 523 K are in agreement with Lee results for a deposition temperature of 573 K and for temperatures below 250 K. For all deposition temperatures we observe a first raise with temperature up to 350 K, followed by a decreasing behavior up to our highest measured temperature. It is important to mention that the slope of the first raise is one order of magnitude larger than the slope of the decrease, as can be seen in table (3.2). As already said, this decrease is at odds with what usually reported in amorphous materials, where thermal conductivity increases

with temperature at high temperature. A maximum at low temperature is usually observed in crystals, where it is however at much lower temperatures and due to the activation of Umklapp scattering [114,115], however in amorphous materials this is not so. The presence of a maximum at about 250 K points to the existence of a scattering mechanism for phonons which activates at such temperature. We are still investigating this behavior, which could be ascribed to the instability of the stoichiometry and bond organization in our material, as highlighted in the previous section.

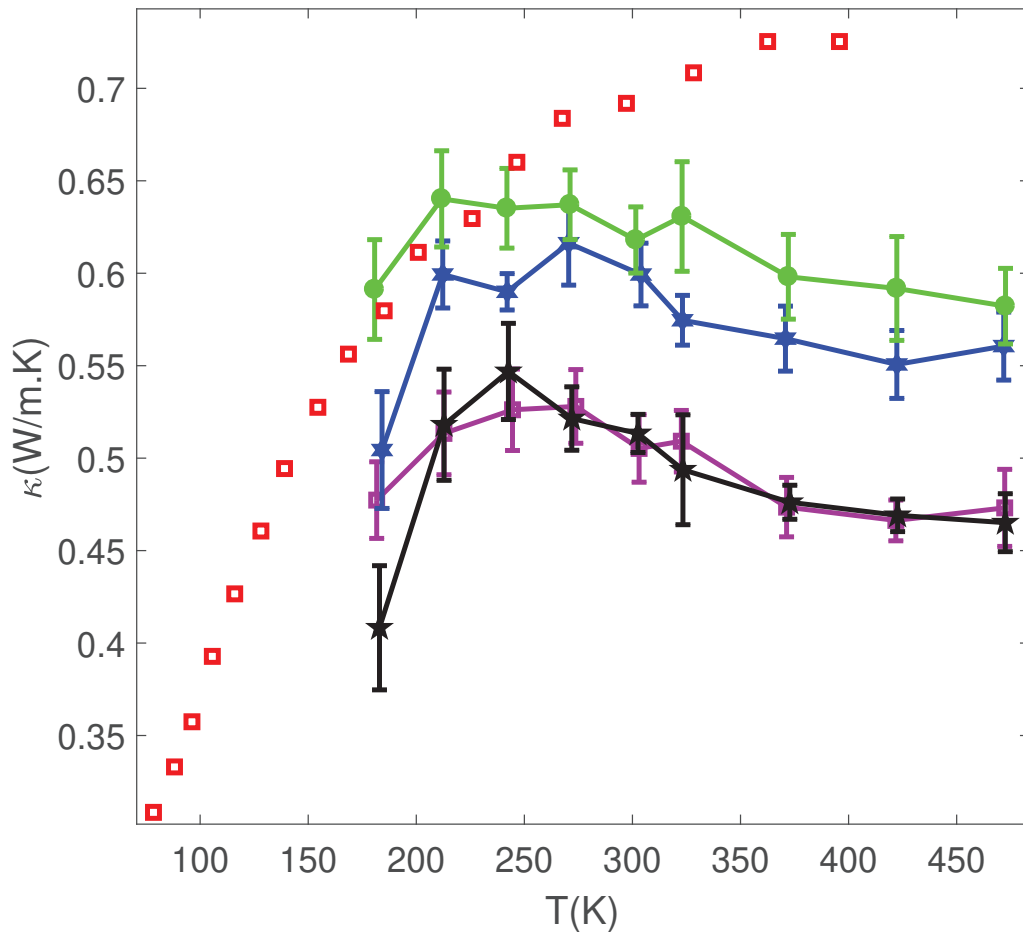


**Figure 3.10:** The low temperature thermal conductivity of  $\text{SiN}_x$  on Si grown by PECVD from 183 K up to 473 K. The different lines is for different deposition temperatures as following: purple (323 K), black (373 K), blue (473 K), and green (523 K). The error bars correspond to the standard deviation of the distribution of values obtained from 8 different measurements at each temperature. The red squares are the data taken from the thermal conductivity measurement of Lee et al. [56] of  $\text{SiN}_x$  grown by PECVD.

Sample deposition temperature (K)	Positive slope for low temperature regime (W/m.K <sup>2</sup> )	Negative slope for low temperature regime (W/m.K <sup>2</sup> )
323	0.0012	0.0003
373	0.0037	0.0003
473	0.0034	0.0002
523	0.0031	0.0003

**Table 3.2:** The relative positive slope in the low temperature regime and the relative negative slope in high temperature regime for the variation of thermal conductivity as a function of temperature for amorphous Silicon nitride grown by PECVD at different deposition temperature.

# Chapter 4

## Phonon Dynamics in Amorphous Silicon Nitride

In this study, we investigated the effect of the nanostructuration on the phonon dynamics of the system. This work is part of the IPPON project, where the main aim is to optimize both photon and phonon through the same nanostructuration. The phonon dynamics in this study is investigated using the Transient grating technique at the Free Electron Laser in Trieste at phonon wavelengths of 55, 84 and 106 nm. The following sections report phonon dynamics in a homogeneous, non nanostructured,  $\text{SiN}_x$  thin film (4.2) and in a nanostructured sample (4.3).

### 4.1 Samples

The first measured sample for transient grating is the nanostructured PECVD  $\text{SiN}_x$  from INL, on Si substrate, 200 nm thick, deposited at 300 °C with deposition parameters as in section (3.1), with young modulus 160 GPa and density 2.4 g/cm<sup>3</sup>. The TG measurements at XFEL in reflection geometry on the sample on substrate turned out to be extremely difficult, and the signal very weak. We thus tried to etch the substrate to have suspended PECVD SiN for working in transmission, but the nanostructured PECVD SiN could not be suspended. The membrane broke at every attempt.

We turned then to commercial samples, LPCVD SiN with young modulus 220 GPa and density 2.9 g/cm<sup>3</sup>, from Norcada, 55 nm thick, suspended with nanopores nanostructuration with the following specifications: pore center to pore center in X and Y direction 377 nm, pore diameter at the top surface  $149 \pm 7$  nm, pore diameter at the bottom surface  $99 \pm 7$  nm, and the average diameter of the pore 124 nm, as shown in figure (4.1). The SiN is different, with different elastic constants, but the physics will remain the same.

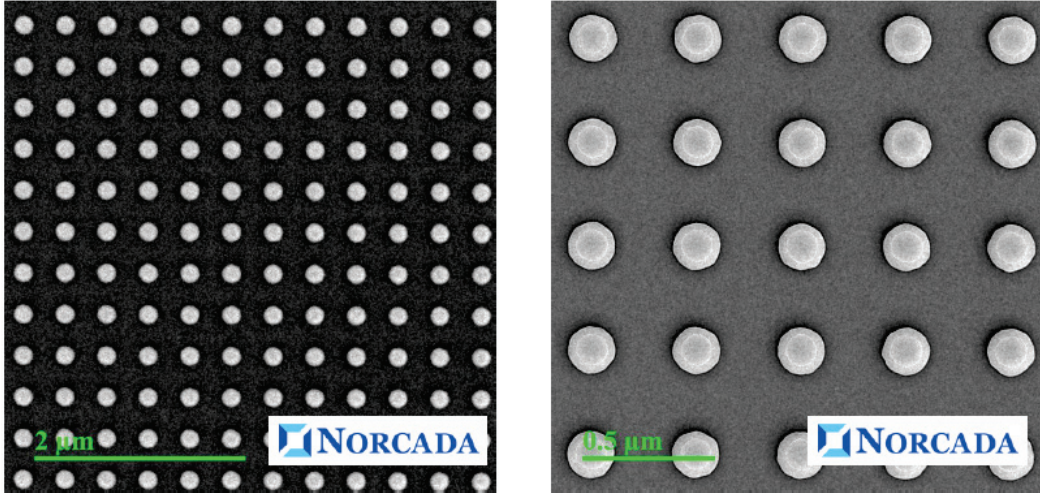


**Figure 4.1:** TEM images at different scales on left and right of the nanostructured surface with nanopores with the following specifications: pore center to pore center in X and Y direction 377 nm, pore diameter at the top surface  $149 \pm 7$  nm, pore diameter at the bottom surface  $99 \pm 7$  nm, and the average diameter of the pore 124 nm.

## 4.2 Phonon Dynamics in a Homogeneous Amorphous $\text{SiN}_x$ Thin Film

In the next sub-section, we describe first some data obtained in reflection geometry on PECVD  $\text{SiN}_x$  on silicon. The weak signal motivated us to move to suspended membranes in order to work in transmission mode. In the following sub-sections we report the results of our experiments on LPCVD homogeneous and nanostructured suspended  $\text{SiN}_x$ . First, we report the data obtained on the homogeneous sample at a phonon wavelength of 55, 84 and 106 nm. Data have been fitted using the model described in section (2.2.2), and compared with available results on LPCVD suspended  $\text{SiN}_x$  from Milloch PhD thesis [68]. Second, we present data on the nanostructured sample at the same wavelengths.

### 4.2.1 PECVD $\text{SiN}_x$ in Reflection Geometry

The first measurement of TG was performed on PECVD  $\text{SiN}_x$  on Si substrate in reflection mode, the measured signal in uniform and nanostructured sample is shown in figures (4.2.a) and (4.2.c). The measured TG signal in the nanostructured material is very weak, despite that we were working at the maximum possible fluence just below the radiation damage threshold. That's why we developed a program for a better background subtraction for weak signals. We moved to transmission mode in TG by measuring on suspended membrane LPCVD amorphous Silicon Nitride. The signal is much more intense in both homogeneous and nanostructure samples, as shown in figure (4.2.b) and (4.2.d). This is

why we went for suspended membranes, but also to have the intrinsic properties of the SiN thin films, as in the supported one the waves are leaky waves, so that phonon lifetime is ruled by the SiN-Si interface scattering.

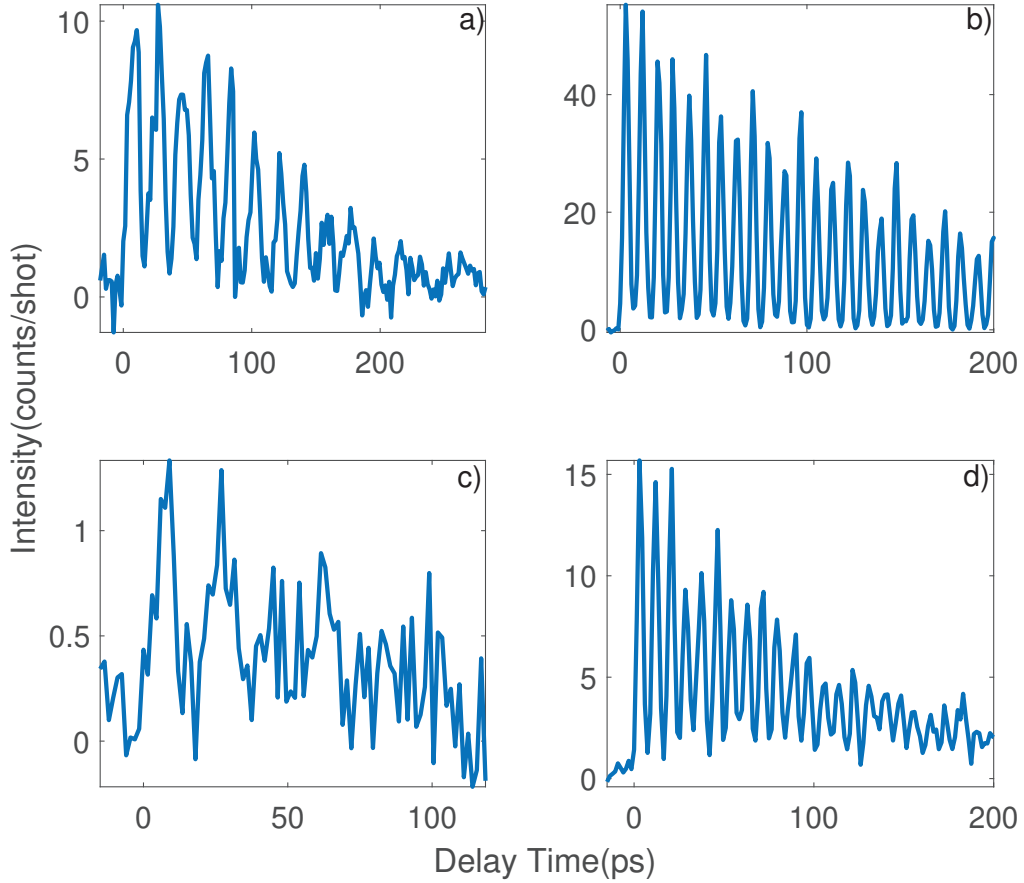


**Figure 4.2:** The measured TG signal of uniform (a) and nanostructured (c) PECVD amorphous Silicon Nitride on Silicon substrate in reflection mode at phonon wavelength of 84 nm. The measured TG signal of uniform (b) and nanostructured (d) suspended membrane LPCVD amorphous Silicon Nitride in transmission mode at phonon wavelength of 84 nm.

#### 4.2.2 Suspended LPCVD SiN<sub>x</sub> Membranes

In the following, we will discuss the measured TG at phonon wavelength of 55, 84, and 106 nm in suspended LPCVD SiN<sub>x</sub> membranes measured in transmission geometry.

## Phonon Wavelength at 55 nm

The experimental measured signal at phonon wavelength of 55 nm is shown in figure (4.3). The transient grating technique involves crossing two short FEL pump pulses (150fs) to create a sinusoidal interference pattern, which when absorbed by the sample induces a sinusoidal response. When light is absorbed, the sinusoidal response is a temperature profile, and upon thermal expansion an acoustic phonon is generated, so the TG signal is a combination of temperature profile and generated acoustic phonons where both of them have decay time as seen in equation (2.21). The first step is to fit the data to exponential decay, as shown in figure (4.3), the fitted parameters are the amplitude  $A_{55nm} = 79 \pm 4$ , and the decay time  $B_{55nm} = 76 \pm 6$  ps.

Then the the fitted exponential decay is subtracted from the TG signal as shown in figure (4.4). A Fourier transform is applied to the subtracted data, shown in figure (4.5), in order to identify the number and frequency of phonon modes which have to be included in the fitting model (see equation 2.21). We have seen six modes in the Fourier transform where the different frequency of each mode is given as A=0.0257 THz, B=0.167 THz, C=0.1929 THz, D=0.3344 THz, E=0.3601 THz and F=0.3891 THz. Some of these modes are harmonics of each other. To identify the harmonics, we have calculated the squared of equation (2.21) in the case of only 2 independent phonon modes of frequency  $f_1$  and  $f_2$ . We find that the signal should have 6 oscillating contributions with frequencies  $f_1 - f_2$ ,  $f_1$ ,  $f_2$ ,  $2 * f_1$ ,  $2 * f_2$ , and  $f_1 + f_2$ . In our case, it is A=C-B, D=2\*B, E=B+C, F=2\*C, so, at the end, we conclude that we have only two independent phonon modes with frequencies B=0.167 THz and C=0.1929 THz.

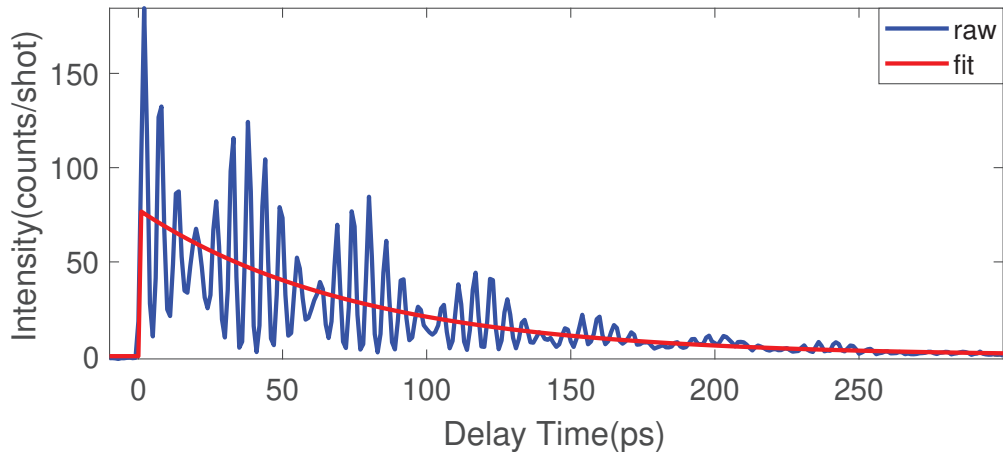


**Figure 4.3:** The blue line is the measured TG signal of amorphous Silicon Nitride at phonon wavelength of 55 nm, and the red line is the fit of the TG signal with exponential decay.

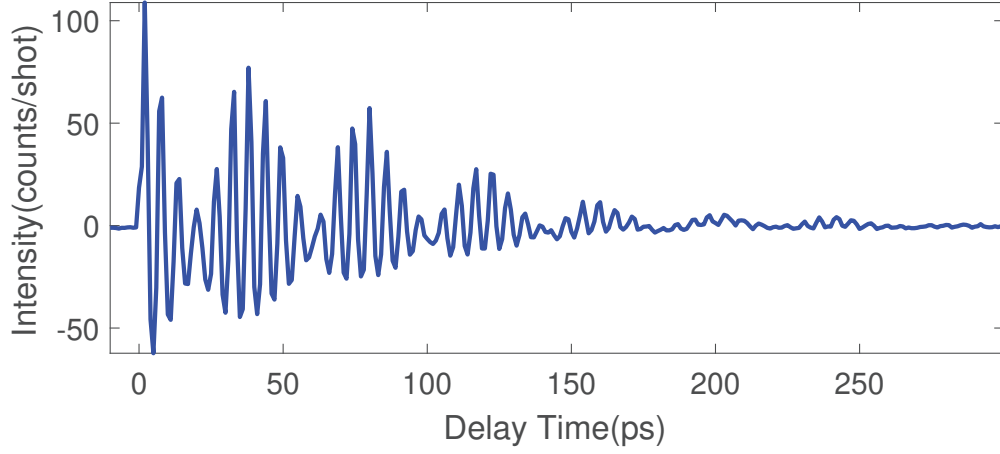


**Figure 4.4:** Pure oscillating signal as obtained after subtraction of the exponential decay from the TG signal (4.3).

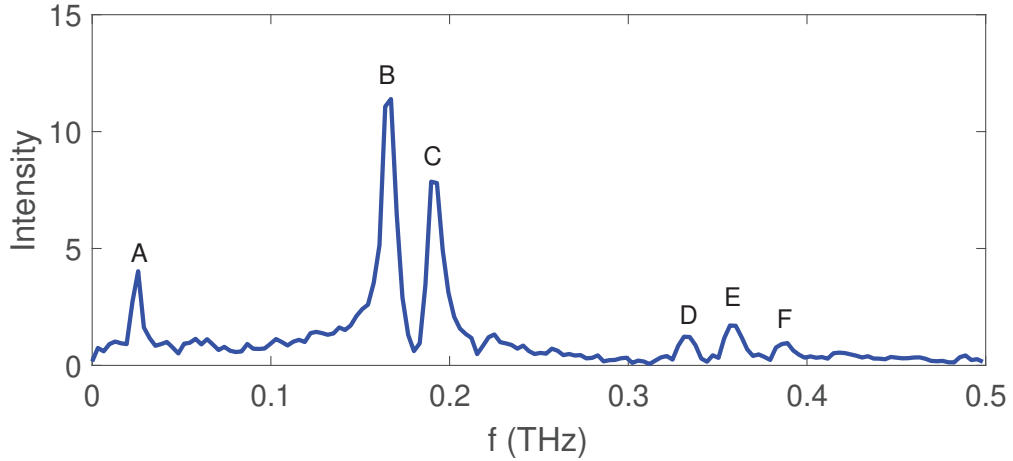


**Figure 4.5:** The Fourier transform of the subtracted data shown in figure (4.4), the peaks of the Fourier transform have the following positions A=0.0257 THz, B=0.167 THz, C=0.1929 THz, D=0.3344 THz, E=0.3601 THz and F=0.3891 THz.

The fit of the TG signal with the equation (2.21) is shown in figure (4.6.a). The fitted parameters are the thermal amplitude  $A_{th} = 7.97 \pm 0.07$ , the thermal decay  $\tau_{th} = 167 \pm 4$  ps, the first phonon amplitude  $A_1 = 2.43 \pm 0.09$ , the first phonon life time  $\tau_1 = 156 \pm 16$  ps, the first phonon frequency  $\nu_1 = 0.19117 \pm 0.00008$  THz, the second phonon amplitude  $A_2 = 3.80 \pm 0.10$ , the second phonon life time  $\tau_2 = 120 \pm 8$  ps, and the second phonon frequency  $\nu_2 = 0.16648 \pm 0.00007$  THz.

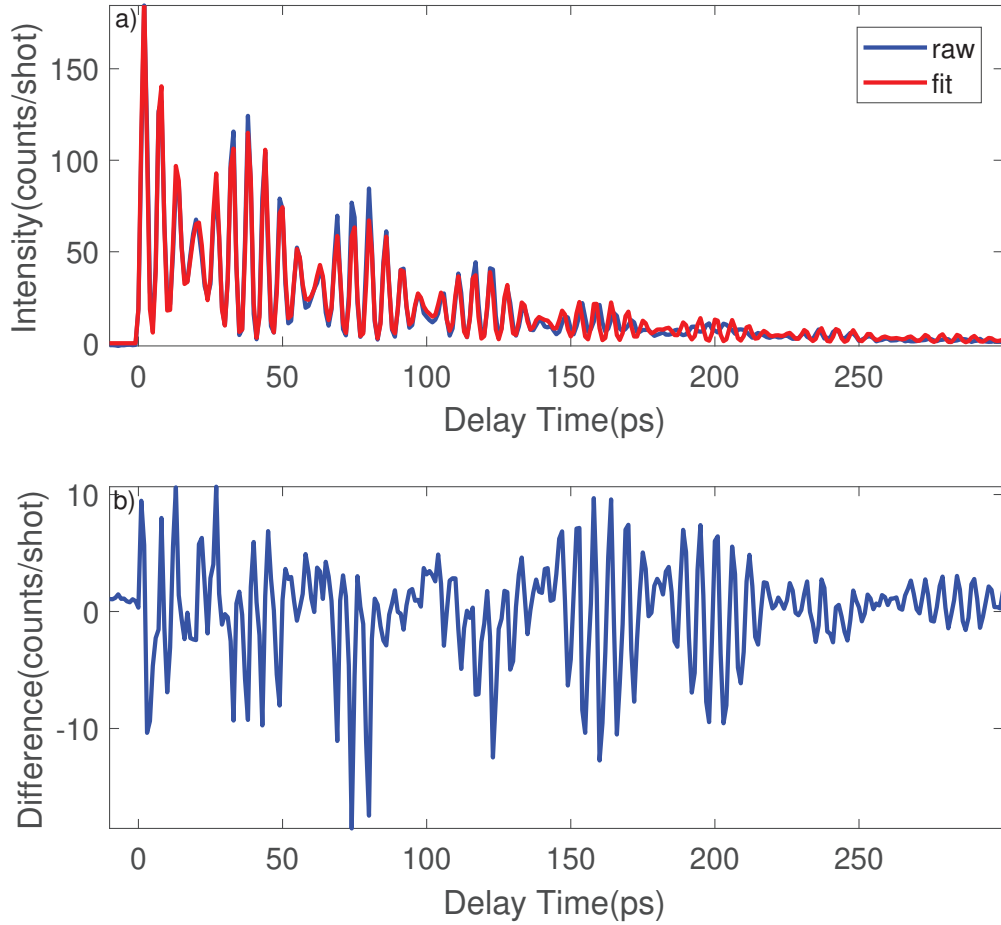


**Figure 4.6:** a) The fitting of TG signal with equation (2.21) of the homogeneous amorphous Silicon Nitride at phonon wavelength of 55 nm. b) The difference between the raw data and the fitted data.

We can see that starting from around 140 ps there is a shift between the fitting model and the data, and it is observed better in the difference between the raw data and the fitted data shown in figure (4.6.b). This was a rigid shift. The frequency of the TG signal after 140 ps is slightly shifted from the frequency of the TG signal from the beginning till 140 ps, this is clarified from the Fourier transform of the two time regions as shown in figure (4.7). The fit made using the full range has therefore a larger error in frequency, but we keep it like this, as the origin of the shift is still under investigation. We suspect it is an artefact due to a problem in the beamline setup, which was very slowly losing the time alignment between pump and probe. A calibration was done in order to correct for this disalignment, but it was not always properly working

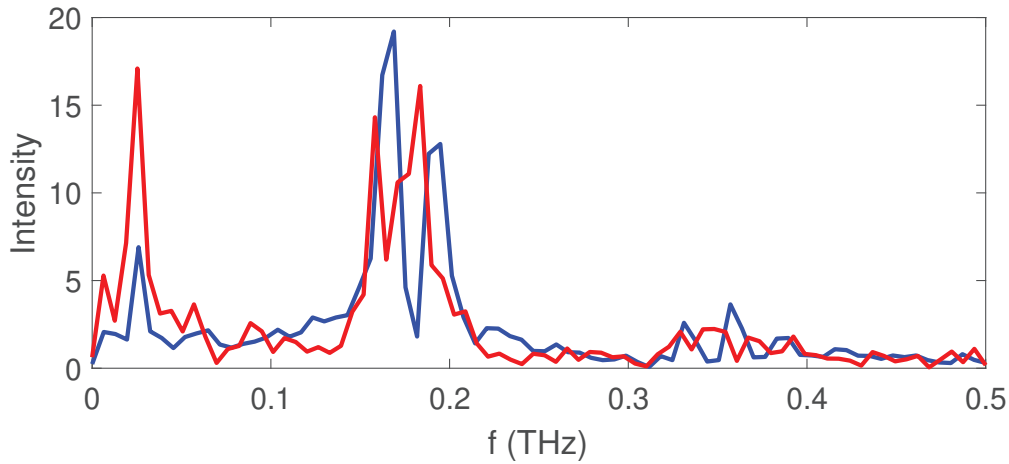


**Figure 4.7:** The blue line is the Fourier transform of the subtracted data from the beginning to 140 ps, and the red line is the Fourier transform of the subtracted data from 140 ps to the end. The intensity of the blue line is multiplied by 10 just for better comparison with the red line.

### Phonon Wavelength at 84 nm

The experimental measured signal at phonon wavelength of 84 nm is shown in figure (4.8).

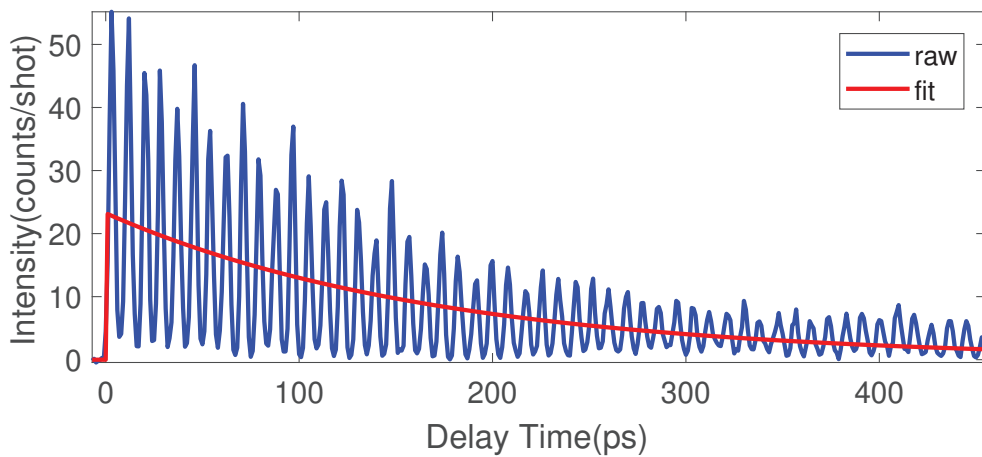


**Figure 4.8:** The blue line is the measured TG signal of uniform amorphous Silicon Nitride at phonon wavelength of 84 nm, and the red line is the fit of the TG signal with exponential decay.

We can see that the time range of this TG signal is wider than that of the TG signal at 55 nm due to a longer phonon lifetime and/or thermal relaxation decay [71]. Both time constants are expected to be longer for longer wavelengths.

We follow the same procedure described in sections (2.2.2) and (4.2.2) where the fit of the data to exponential decay give a thermal amplitude  $A_{84nm} = 23 \pm 1$ , and thermal decay time  $B_{84nm} = 172 \pm 14$  ps, and the subtracted signal is shown in figure (4.9).

A Fourier transform is applied to the subtracted data as shown in figure (4.10), from which we see three modes with frequencies A=0.1166 THz, B=0.1577 THz and C=0.2333 THz. Noticing that  $C=2*A$ , we can assume that we have again only two independent phonon modes in our system with frequencies A=0.1166 THz and B=0.1577 THz.

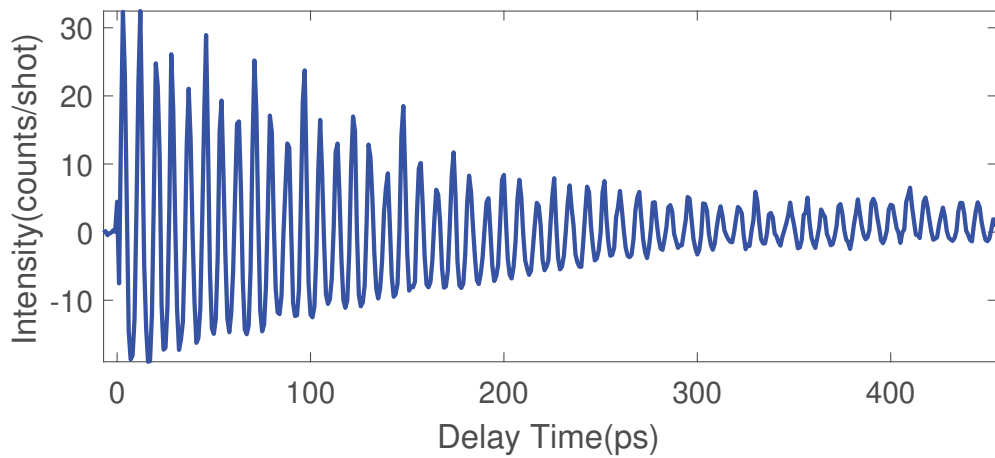


**Figure 4.9:** Pure oscillating signal as obtained after subtraction of the exponential decay from the TG signal.

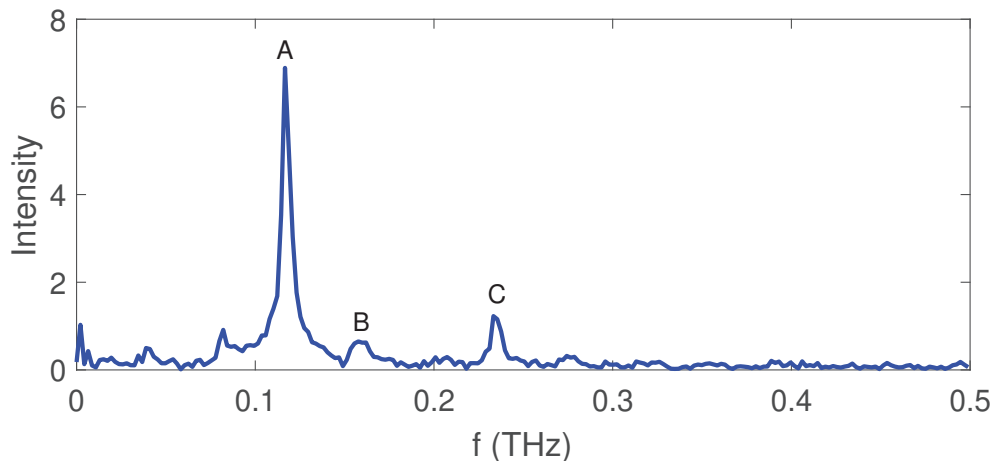


**Figure 4.10:** The Fourier transform of the subtracted data shown in figure (4.9), the peaks of the Fourier transform have the following positions A=0.1166 THz, B=0.1577 THz and C=0.2333 THz.

The fit of the TG signal with the equation (2.21) is shown in figure (4.11.a). The fitted parameters are the thermal amplitude  $A_{th} = 4.13 \pm 0.07$ , the thermal decay  $\tau_{th} = 429 \pm 20$  ps, the first phonon amplitude  $A_1 = 3.4 \pm 0.1$ , the first phonon life time  $\tau_1 = 172 \pm 10$  ps, the first phonon frequency  $\nu_1 = 0.11719 \pm 0.00005$  THz, the second phonon amplitude  $A_2 = 0.28 \pm 0.07$ , the second phonon life time  $\tau_2 = 318 \pm 223$  ps, and the second phonon frequency  $\nu_2 = 0.1571 \pm 0.0002$  THz.

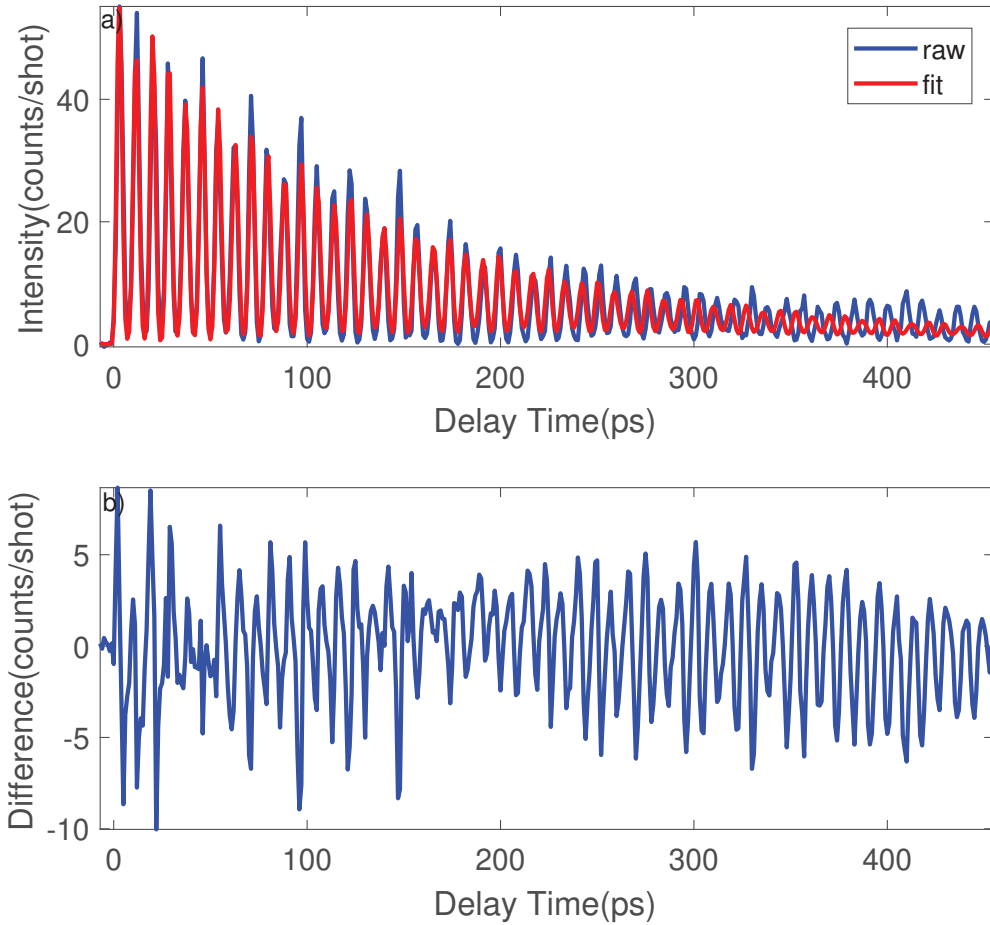


**Figure 4.11:** a) The fitting of TG signal with equation (2.21) of the uniform amorphous Silicon Nitride at phonon wavelength of 84 nm. b) The difference between the raw data and the fitted data.

As in the case of a phonon wavelength of 55nm, we notice a shift between the fitted model and the data, which, in this case, starts at about 300 ps. Opposite to the previous case, however, this does not appear as a rigid, sudden shift, but as a slowly changing frequency with time. We could indeed improve the fit by assuming a phonon frequency decreasing linearly with time. This is shown in

figure (4.12), phonon frequencies and change rate are the first phonon frequency  $\nu_1 = 0.11868 \pm 0.00005$  THz, the first phonon decreasing rate  $72 \cdot 10^{-7} \pm 2 \cdot 10^{-7}$  THz<sup>2</sup>, the second phonon frequency  $\nu_2 = 0.1597 \pm 0.0002$  THz, and the second phonon decreasing rate  $126 \cdot 10^{-7} \pm 7 \cdot 10^{-7}$  THz<sup>2</sup>. The origin of such behavior can once again be a time misalignment between pump and probe.

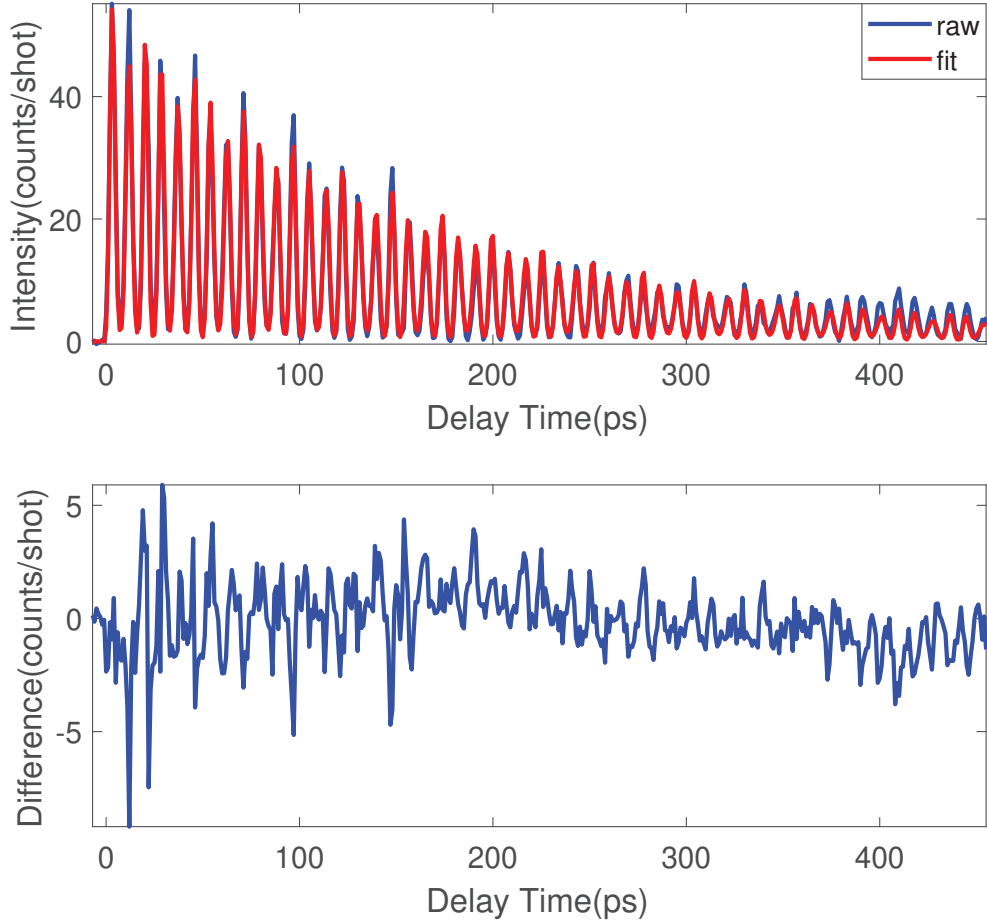


**Figure 4.12:** a) Data at phonon wavelength of 84 nm collected on the uniform amorphous Silicon Nitride, together with the fit to a model in which the phonon frequency decreases linearly with time. b) The difference between the raw data and the fitted data.

### Phonon Wavelength at 106 nm

The experimental measured signal at phonon wavelength of 106 nm is shown in figure (4.13). We follow the same procedure described in sections (2.2.2) and (4.2.2) where the fit of the data to exponential decay give a thermal amplitude

$A_{106nm} = 11.7 \pm 0.7$ , and thermal decay time  $B_{106nm} = 260 \pm 27$  ps, as shown in figure (4.13), and the subtracted signal is shown in figure (4.14).

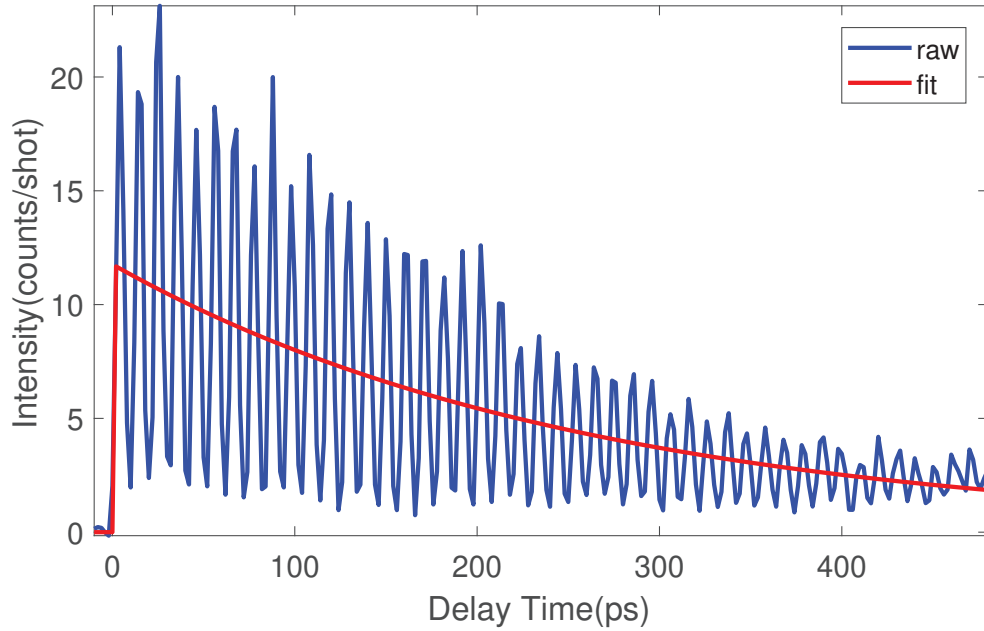


**Figure 4.13:** The blue line is the measured TG signal of uniform amorphous Silicon Nitride at excitation wavelength of 106 nm, and the red line is the fit of the TG signal with exponential decay.

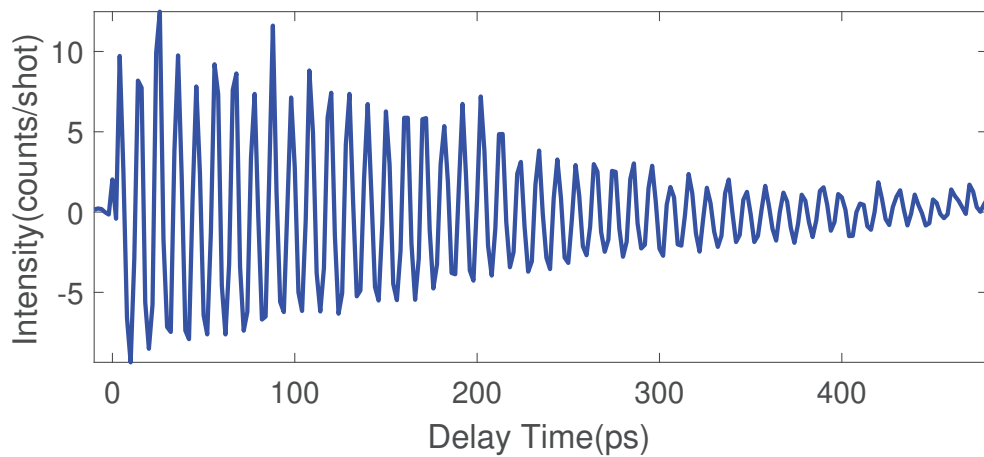


**Figure 4.14:** Pure oscillating signal as obtained after subtraction of the exponential decay from the TG signal.

A Fourier transform is applied to the subtracted data as shown in figure (4.15), from which we find two phonon modes with frequencies  $A=0.096$  THz, and  $B=0.193$  THz. In order to identify the number of independent phonon modes, we have calculated the square of equation (2.21). We solved the squares for equation (2.21) for one phonon mode of frequency  $f_1$ , and it appears that there are two oscillating contributions with frequencies  $f_1$ , and  $2 * f_1$ . In our case, it is  $B=2*A$ , so we can assume that we have only one phonon mode in our system with frequency  $A=0.096$  THz.

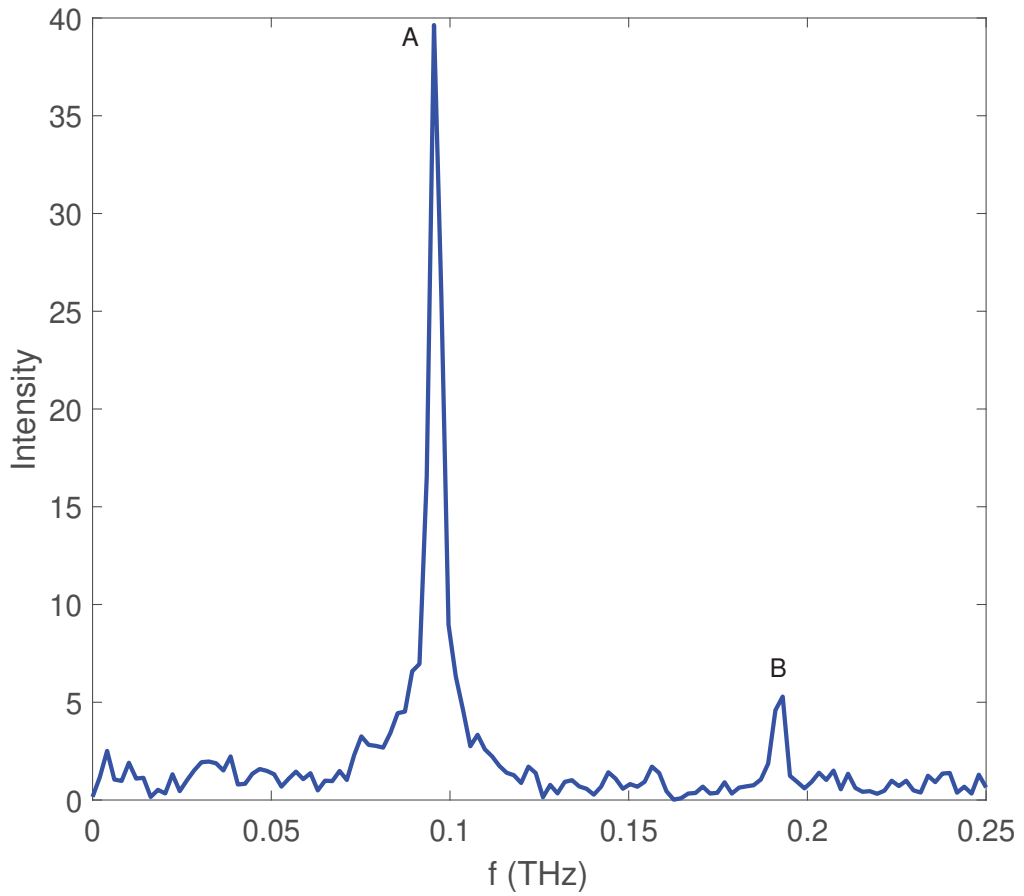


**Figure 4.15:** The Fourier transform of the subtracted data shown in figure (4.14), the peaks of the Fourier transform have the following positions  $A=0.096$  THz, and  $B=0.193$  THz.

The fit of the TG signal with the equation (2.21) is shown in figure (4.16.a). The fitted parameters are the thermal amplitude  $A_{th} = 3.19 \pm 0.02$ , the thermal decay  $\tau_{th} = 564 \pm 12$  ps, the phonon amplitude  $A_1 = 1.67 \pm 0.03$ , the phonon life time  $\tau_1 = 334 \pm 15$  ps, and the phonon frequency  $\nu_1 = 0.09606 \pm 0.00002$  THz. In this

case, no shift was observed between the model and the raw data.

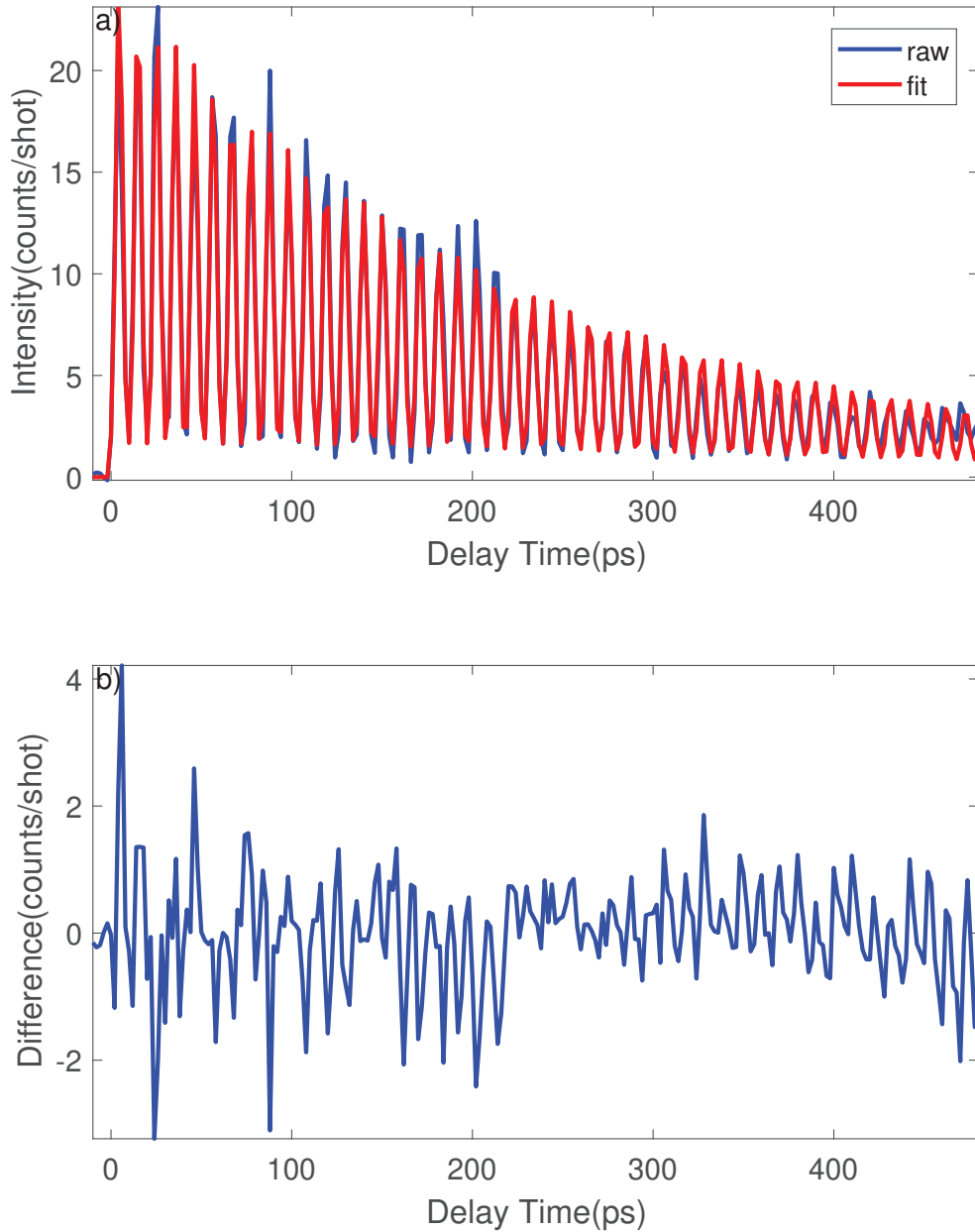


**Figure 4.16:** a) The fitting of TG signal with equation (2.21) of the uniform amorphous Silicon Nitride at phonon wavelength of 106 nm. b) The difference between the raw data and the fitted data.

### 4.2.3 Analysis

We report in table (4.1) the summary of the fitted parameters at the three phonon wavelengths in the uniform amorphous Silicon Nitride

$\lambda$ (nm)	55	84	106
$A_{th}$	$7.97 \pm 0.07$	$4.13 \pm 0.07$	$3.19 \pm 0.02$
$\tau_{th}$ (ps)	$167 \pm 4$	$429 \pm 20$	$564 \pm 12$
$A_1$	$2.43 \pm 0.09$	$3.4 \pm 0.1$	$1.67 \pm 0.03$
$\tau_1$ (ps)	$156 \pm 16$	$172 \pm 10$	$334 \pm 15$
$\nu_1$ (THZ)	$0.19117 \pm$ $0.00008$	$0.11719 \pm$ $0.00005$	$0.09606 \pm$ $0.00002$
$A_2$	$3.8 \pm 0.1$	$0.28 \pm 0.07$	
$\tau_2$ (ps)	$120 \pm 8$	$318 \pm 223$	
$\nu_2$ (THZ)	$0.16648 \pm$ $0.00007$	$0.1571 \pm 0.0002$	

**Table 4.1:** Summary of the fitted parameters of the TG signal of uniform amorphous Silicon nitride membrane. The representation of each symbol is the following,  $\lambda$  phonon wavelength,  $A_{th}$  thermal amplitude,  $\tau_{th}$  thermal decay time,  $A_1$  first phonon amplitude,  $\tau_1$  first phonon life time,  $\nu_1$  first phonon frequency,  $A_2$  second phonon amplitude,  $\tau_2$  second phonon life time, and  $\nu_2$  second phonon frequency. For a phonon wavelength of 106 nm, only one phonon mode is observed.

In order to interpret these results, we have calculated the Lamb dispersions using  $v_L = 11178$  m/sec (longitudinal velocity) and  $v_S = 6275$  m/sec (shear velocity) values calculated from density =  $2.9$  g/cm<sup>3</sup>, Young Modulus =  $270$  GPa, and Poisson ratio =  $0.27$  as given by Norcada for these samples. We have found that our phonon modes velocities, calculated as  $v = \nu * \lambda$ , did not match exactly the branches. Thus, we have optimized the elastic constants in order to have the best match between calculated branches and our phonon phase velocities, as shown in figure (4.17). we obtain  $v_L = 9736$  m/sec and  $v_S = 5465$  m/sec, corresponding to a Young modulus =  $220$  GPa, which is softer than the one reported by Norcada for this sample. This can be understood as due to a large scattering of elastic constant data on SiN<sub>x</sub>, but also to the fact that our measurements correspond to a local sample temperature larger than room temperature, and elastic constants are expected to decrease with temperature. We can calculate the temperature raise in our sample, knowing the fluence on the sample per unit area and the attenuation length at the pump wavelength.

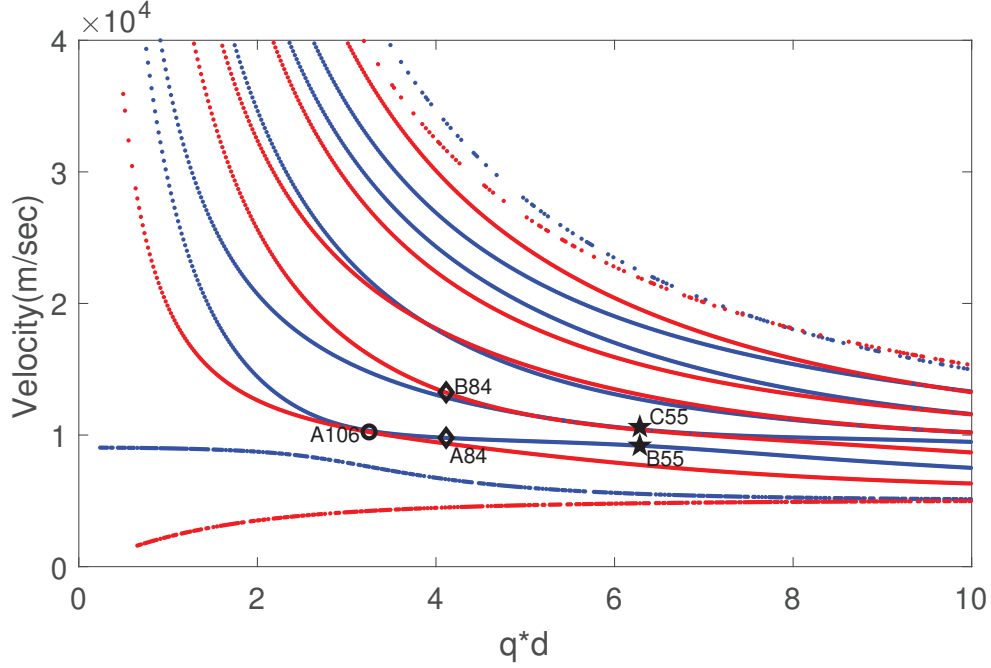


**Figure 4.17:** The Lamb waves dispersion curves are numerically calculated for  $v_l = 9736$  m/sec and  $v_s = 5465$  m/sec of the amorphous silicon nitride membrane to overlap the fitted phase velocities in black. Blue and red lines are symmetric and antisymmetric modes respectively, the black circle corresponds to phonon frequency at 106 nm, the black diamond corresponds to phonon frequencies at 84 nm, and the black pentagram corresponds to phonon frequencies at 55 nm.

The absorbed energy by the silicon nitride based on Beer-Lambert law is estimated as [68],

$$E_{absorbed} = E_{deposited}(1 - \exp(-\alpha d)) \quad (4.1)$$

Where  $E_{deposited}$  is the energy of incident radiation,  $\alpha$  is the absorption coefficient, and  $d$  is the sample thickness. The estimation of the volume that is absorbed by the pulse energy is given by  $d * A_{spot}$ , where  $A_{spot}$  is the spot size of the pump beams. The maximum possible increase of temperature in the sample is estimated as,

$$\Delta T_{max} = \frac{E_{absorbed}}{C \rho d A_{spot}} \quad (4.2)$$

Where  $C$  is the specific heat of Silicon Nitride ( $700 \pm 100$  J/kg.k) [116], and  $\rho$  is the density ( $2.9 \pm 0.1$  g/cm<sup>3</sup>). The calculated fluence and the temperature increase in the sample at different wavelengths are shown in table (4.2). We are globally at 100 °C, so not too much. The elastic constants change very weakly with temperature in the 300-500 K range [68], so we cannot explain with

temperature the difference from the nominal elastic constants. This could be ascribed more probably to a non correct value from literature (measured on the supported thinfilm very likely and not on the membrane which will have some compressive or tensile stress) or to the different elastic properties depending on the specific deposition parameters.

Phonon wavelength (nm)	55	84	106
Pump Wavelength (nm)	26.6	39.9	52.3
Pump intensity ( $\mu J$ )	10.24	19.9	55.55
Pump fluence on the sample ( $\mu J/cm^2$ )	$1.1 \pm 0.2$	$1.0 \pm 0.2$	$1.9 \pm 0.4$
Attenuation length (nm)	50	25	10
$\Delta T_{max}$ ( $^{\circ}C$ )	$60 \pm 10$	$80 \pm 20$	$170 \pm 30$
Temperature ( $^{\circ}C$ )	$90 \pm 10$	$110 \pm 20$	$200 \pm 30$

**Table 4.2:** The calculation of the fluence of the pump beam on the sample, the maximum temperature rise, and the temperature in uniform amorphous Silicon Nitride suspended membrane.

The three phonon frequencies A106, 184 and B55 belong to the same branch, thus they correspond to the very same phonon mode. The fact that they fall on the same branch despite the different temperatures at which they have been measured (see table 4.2) confirms that the elastic constants do not depend much on temperature in this temperature range. It thus make sense to look at the wavevector dependence of the fitted parameters, as they relate to the same phonon mode. The thermal relaxation time is related to phonon wavelength as,

$$\tau_{th}^{-1} = \frac{D_{th}4\pi^2}{L_{TG}^2} \quad (4.3)$$

Where  $D_{th}$  is the thermal diffusivity of the material. In figure (4.18), we report the variation of the inverse of the thermal relaxation time vs wavevector in the logarithmic scale. The thermal diffusivity is the half fitted slope, it is found that the thermal diffusivity from the fitting is  $950 \pm 140 \text{ nm}^2/\text{ns}$ . This value is smaller than literature values obtained by means of macroscopic thermal measurements, which is  $1500 \text{ nm}^2/\text{ns}$  for 600 nm in free-standing SiN thinfilm and  $1478 \text{ nm}^2/\text{ns}$  calculated from thermal conductivity measurement [117]. The differences of thermal diffusivity in comparison with the macroscopic thermal measurements could

mean just that the local thermal diffusivity, at the nm scale, is different from the macroscopic one, but an effect of the actual experimental temperature cannot be excluded. Indeed, in the thesis by A. Milloch, it is reported a strong dependence of the thermal relaxation time on the absorbed energy [68, 118]. Still, as seen, temperature is quite low, so that the thermal relaxation time is not expected to change much because of temperature. We are thus left with the hypothesis that the thermal relaxation time at the nm scale is longer than on a microscopic scale.

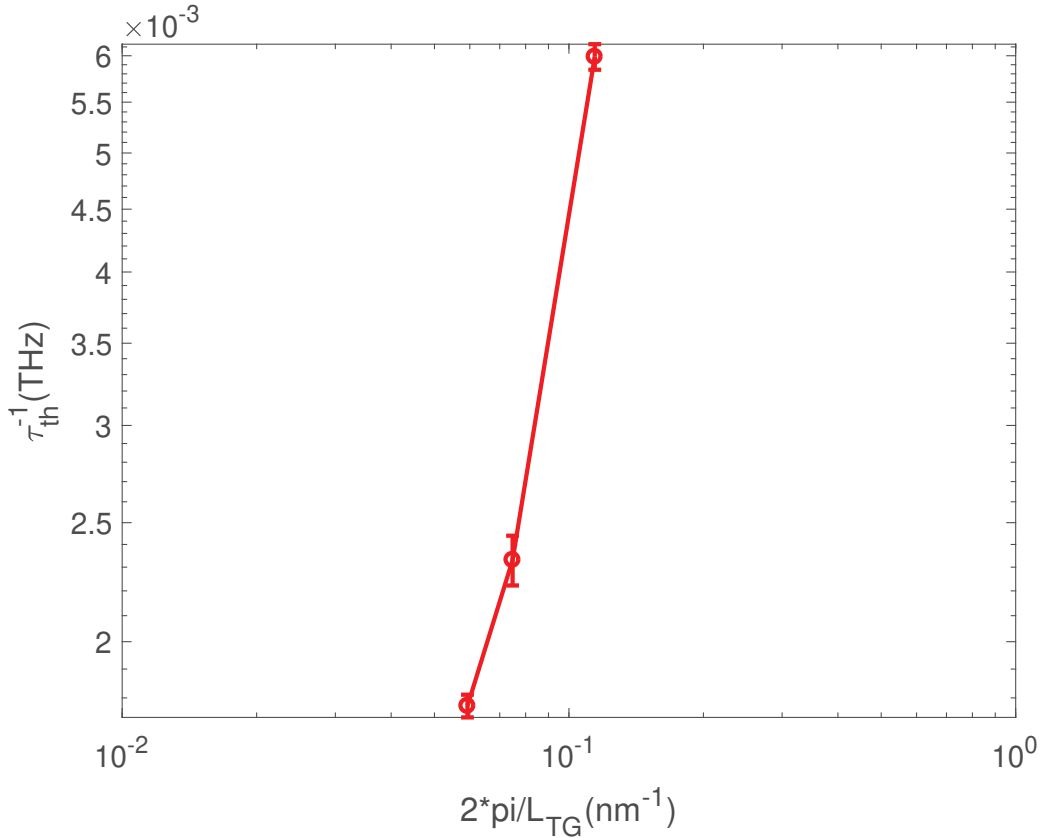


**Figure 4.18:** The variation of the inverse thermal relaxation time vs the wave vector of suspended membrane of amorphous silicon Nitride for the measured transient grating signal at  $L_{TG}=55, 84,$  and  $106$  nm.

We then study the frequency dependence of the phonon lifetime. We report in figure (4.19) the lifetime as a function of  $\omega^{-4}$ . The behavior is quite linear, i.e. phonon lifetime appears to exhibit the  $\omega^{-4}$  behavior. This is proper to the Rayleigh scattering. Such strong dependence on the frequency has been indeed reported in glasses, and ascribed to scattering from disorder, and more specifically from nanometric elastic heterogeneities. Still, this is usually observed at much smaller wavelengths, of the order of 1-10 nm [119]. Finding it at such long wavelengths is something unusual, which requires confirmation. Indeed many are

the sources of uncertainty: 1) for  $\lambda=106$  nm the temperature is much higher. If some anharmonicity is present, then phonon lifetime will also depend on temperature and we would not be measuring the pure wavelength dependence; 2) the fitted phonon lifetime strongly depends on the choice of the model, i.e. how many phonon modes are used for the fit; 3) more wavelengths should be measured to definitely assess the power law

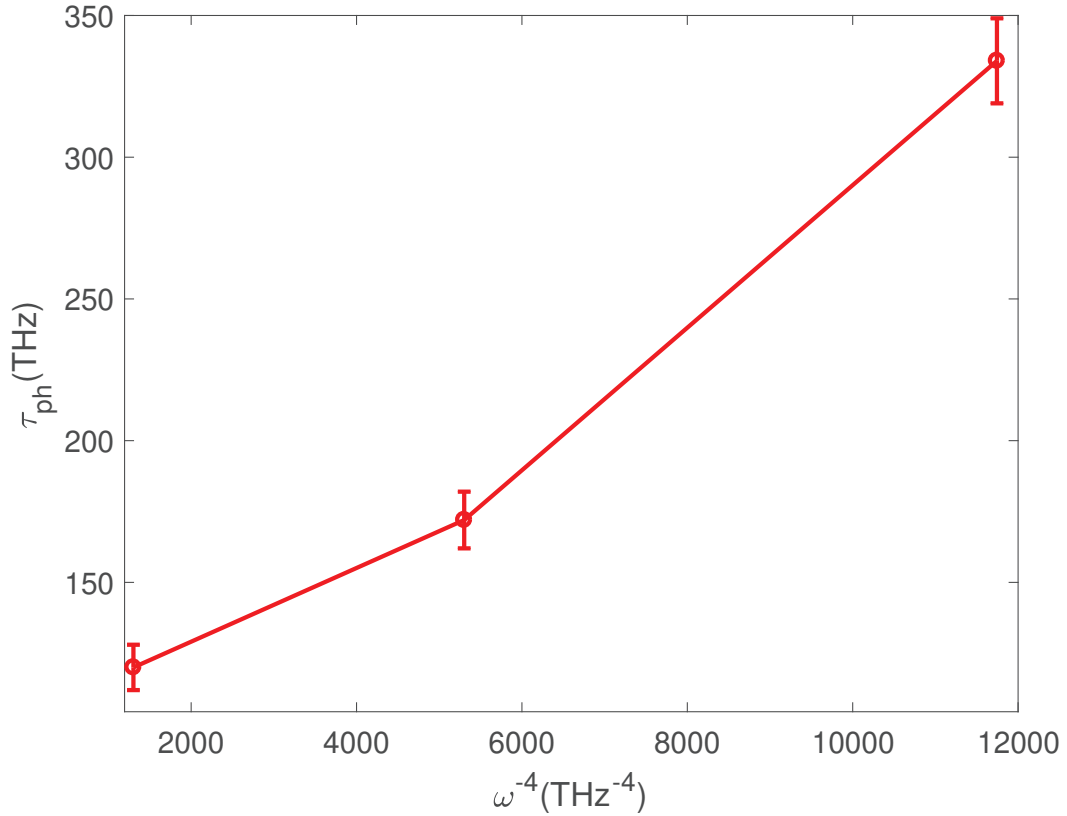


**Figure 4.19:** The variation of the thermal relaxation time vs the phonon frequency power minus four of suspended membrane of amorphous silicon Nitride for the measured transient grating signal at  $L_{TG}=55, 84,$  and  $106$  nm.

### 4.3 Phonon Dynamics in Nanostructured Material

In this section we report results of phonon propagation along the axis of the square lattice, where the distance between two interfaces is 253 nm.

### 4.3.1 Phonon Wavelength at 55 nm

The experimental measured signal at phonon wavelength of 55 nm is shown in figure (4.20).

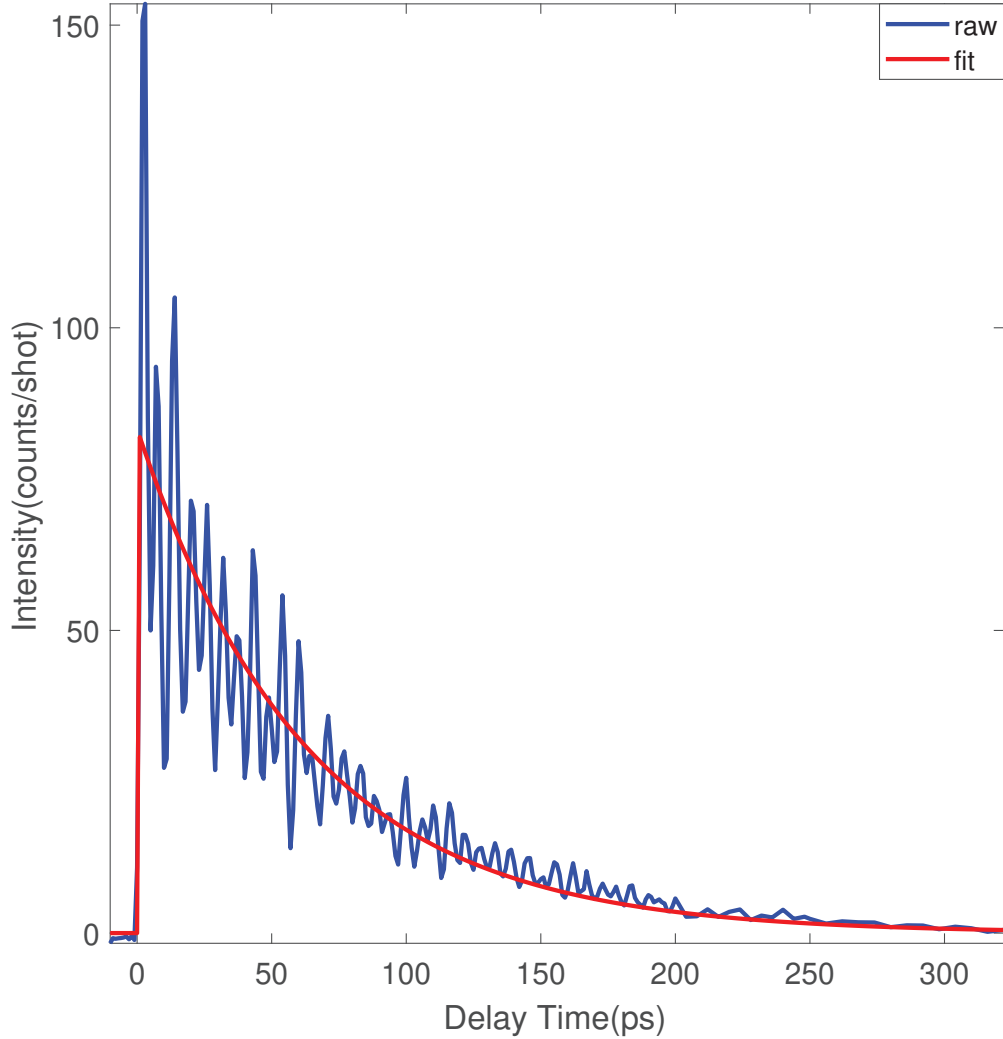


**Figure 4.20:** The blue line is the measured TG signal of the nanostructured amorphous Silicon Nitride at phonon wavelength of 55 nm, and the red line is the fit of the TG signal with exponential decay.

We follow the same procedure described in sections (2.2.2) and (4.2.2) where the fit of the data to exponential decay reported in figure (4.20) give a thermal amplitude  $A_{55nm} = 83 \pm 2$ , and decay time  $B_{55nm} = 63 \pm 2$  ps. The signal subtracted of the exponential behavior is reported in figure (4.21). A Fourier transform is

applied to the subtracted data as shown in figure (4.22), we see four modes in the Fourier transform with frequencies A=0.1051 THz, B=0.1261 THz, C=0.1772 THz, and D=0.1952 THz.

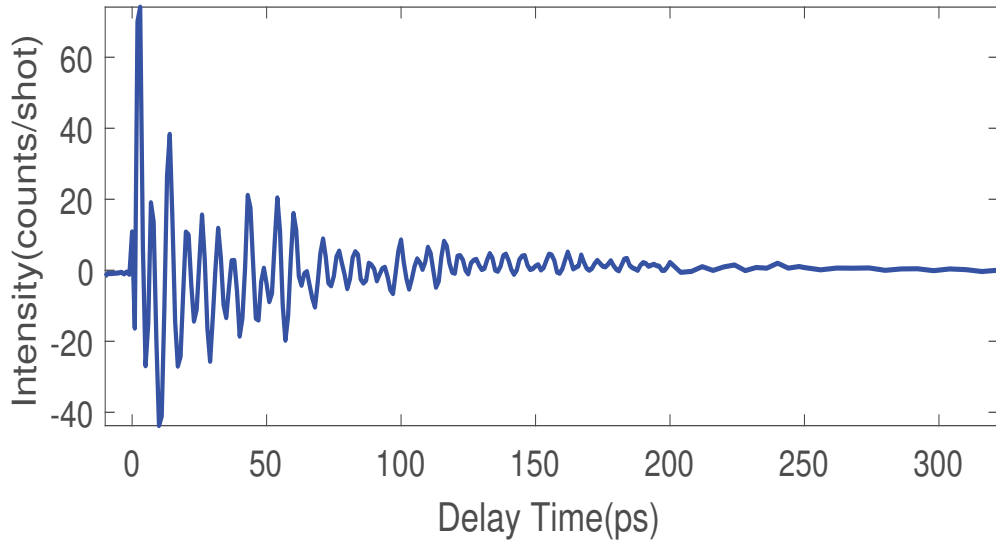


**Figure 4.21:** Pure oscillating signal as obtained after subtraction of the exponential decay from the TG signal.

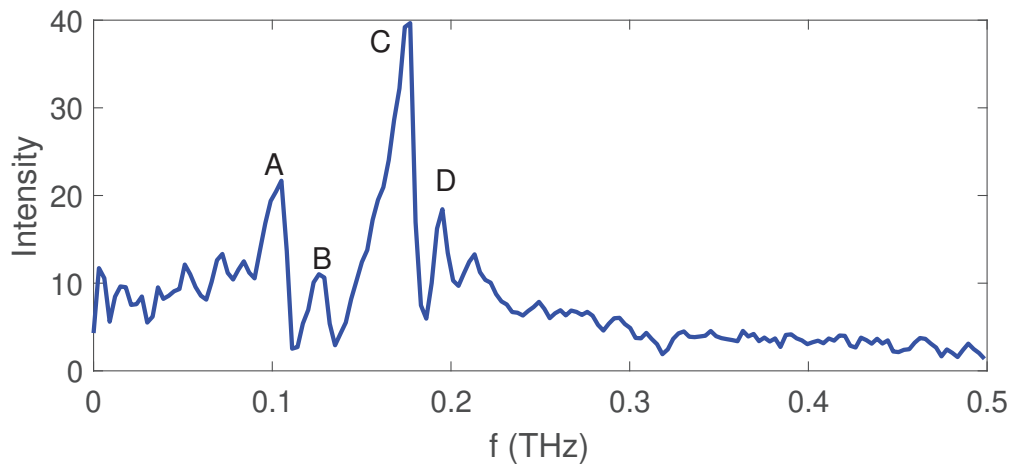


**Figure 4.22:** The Fourier transform of the subtracted data shown in figure (4.21), the peaks of the Fourier transform have the following positions A=0.1051 THz, B= 0.1261 THz, C=0.1772 THz and D=0.1952 THz.

The fit of the TG signal with the equation (2.21) is shown in figure (4.23).

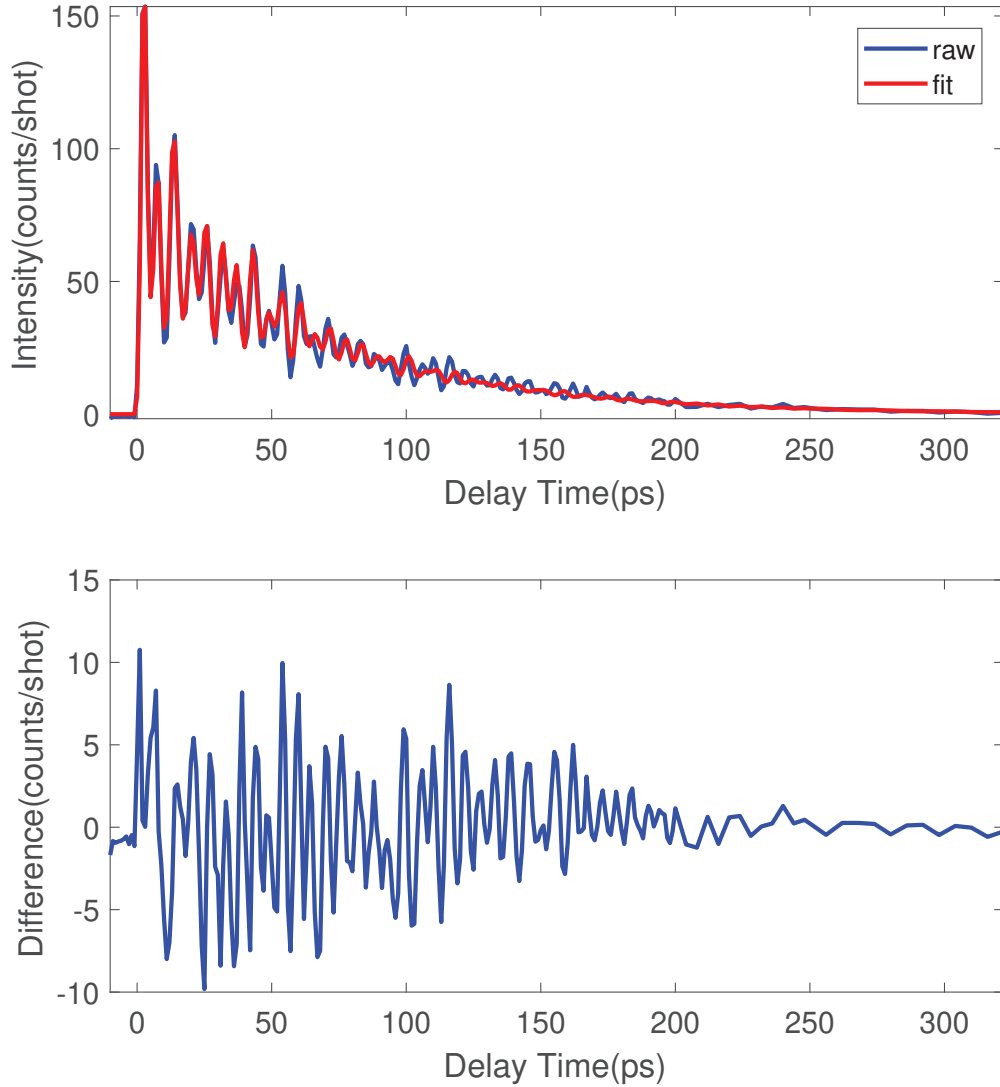


**Figure 4.23:** The top figure is the fitting of TG signal with equation (2.21) of the nanostructured amorphous Silicon Nitride at phonon wavelength of 55 nm, and the low figure is the difference between the raw data and the fitted data.

The fitted parameters are given as following, the thermal amplitude  $A_{th} = 8.67 \pm 0.04$ , the thermal decay  $\tau_{th} = 139 \pm 2$  ps, the first phonon amplitude  $A_1 = 1.6 \pm 0.1$ , the first phonon life time  $\tau_1 = 40 \pm 5$  ps, the first phonon frequency  $\nu_1 = 0.1037 \pm 0.0003$  THz, the second phonon amplitude  $A_2 = 0.41 \pm 0.07$ , the second phonon life time  $\tau_2 = 120 \pm 50$  ps, the second phonon frequency  $\nu_2 = 0.1225 \pm 0.0004$  THz, the third phonon amplitude  $A_3 = 2.4 \pm 0.2$ , the third phonon life time  $\tau_3 = 42 \pm 4$  ps, the third phonon frequency  $\nu_3 = 0.1729 \pm 0.0002$

THz, the fourth phonon amplitude  $A_4 = 2.3 \pm 0.3$ , the fourth phonon life time  $\tau_4 = 11 \pm 2$  ps, and the fourth phonon frequency  $\nu_4 = 0.199 \pm 0.001$  THz. While the short time behavior is well reproduced, for times less than 50 ps, beyond this value the amplitude of the oscillations is underestimated by the fit. This means also that the phonon lifetime will be underestimated. We have tried to change by hand one by one the life time of the four phonons, but this method doesn't help us in improving the quality of the fit. It is possible that more than four phonons need to be considered. However, the fit would become much more complex as the frequencies of additional phonons do not appear clearly from the Fourier transform.

### 4.3.2 Phonon Wavelength at 84 nm

The experimental measured signal at phonon wavelength of 84 nm is shown in figure (4.24). We follow the same procedure described in sections (2.2.2) and (4.2.2) where the fit of the data to exponential decay give a thermal amplitude  $A_{84nm} = 8.2 \pm 0.3$ , and decay time  $B_{84nm} = 132 \pm 8$  ps. The signal after subtraction of the exponential decay is reported in figure (4.25).

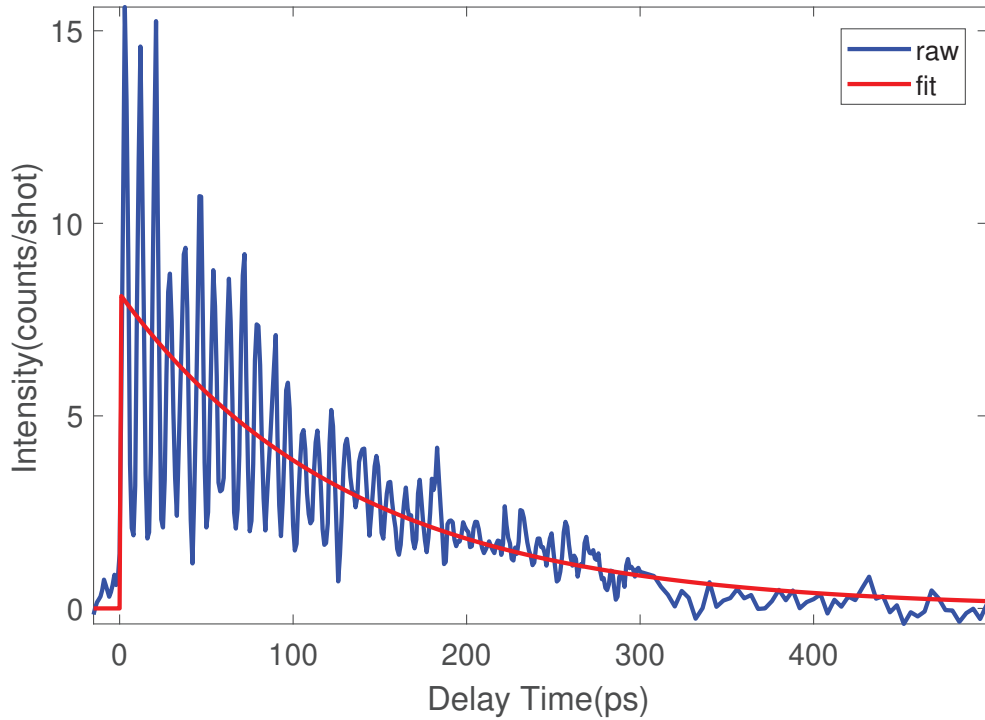


**Figure 4.24:** The blue line is the measured TG signal of nanostructured amorphous Silicon Nitride at phonon wavelength of 84 nm, and the red line is the fit of the TG signal with exponential decay.

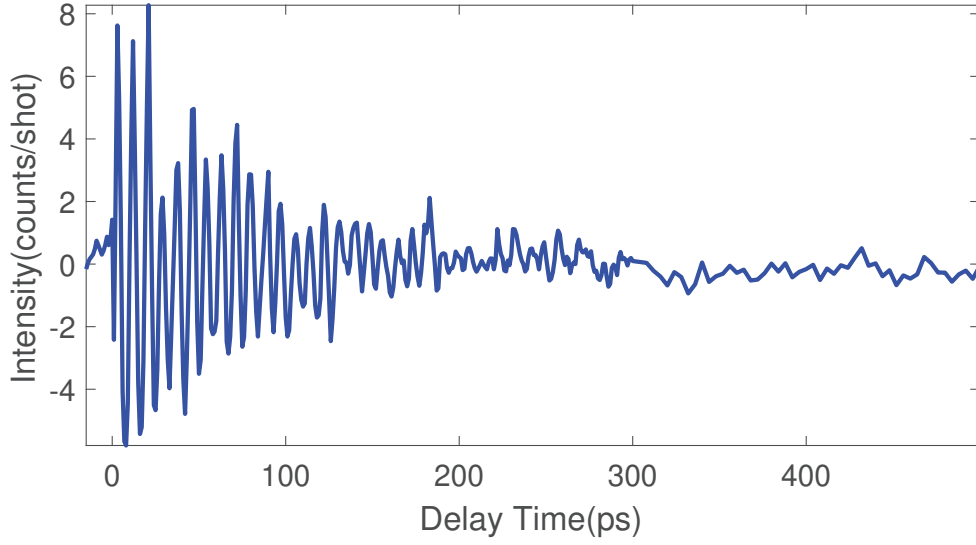


**Figure 4.25:** Pure oscillating signal as obtained after subtraction of the exponential decay from the TG signal.

A Fourier transform is applied to the subtracted data as shown in figure (4.26), we see one mode in the Fourier transform with frequency  $A=0.1182$  THz.

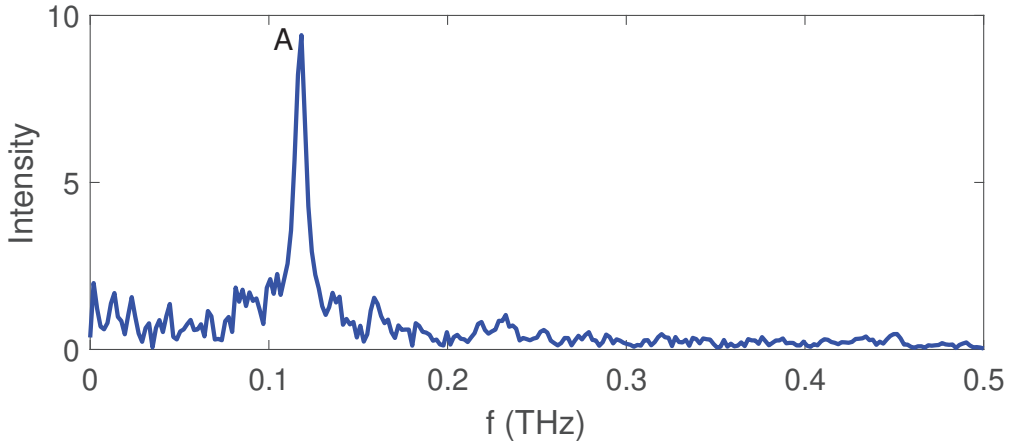


**Figure 4.26:** The Fourier transform of the subtracted data shown in figure (4.25), the peak of the Fourier transform has the following position  $A=0.1182$  THz.

The fit of the TG signal with the equation (2.21) is shown in figure (4.27.a). The fitted parameters are given as following, the thermal amplitude  $A_{th} = 2.69 \pm 0.03$ , the thermal decay  $\tau_{th} = 288 \pm 7$  ps, the phonon amplitude  $A_1 = 1.40 \pm 0.05$ , the life time  $\tau_1 = 104 \pm 6$  ps, and the frequency  $\nu_1 = 0.11770 \pm 0.00009$  THz. The experimental signal is quite well reproduced with this single-phonon fit up to about 300 ps. Beyond this time, the signal was collected with larger

time step, which blurred the fine structure of the oscillations. It does not appear a problem as anyway the signal is here too weak, merging in the background.

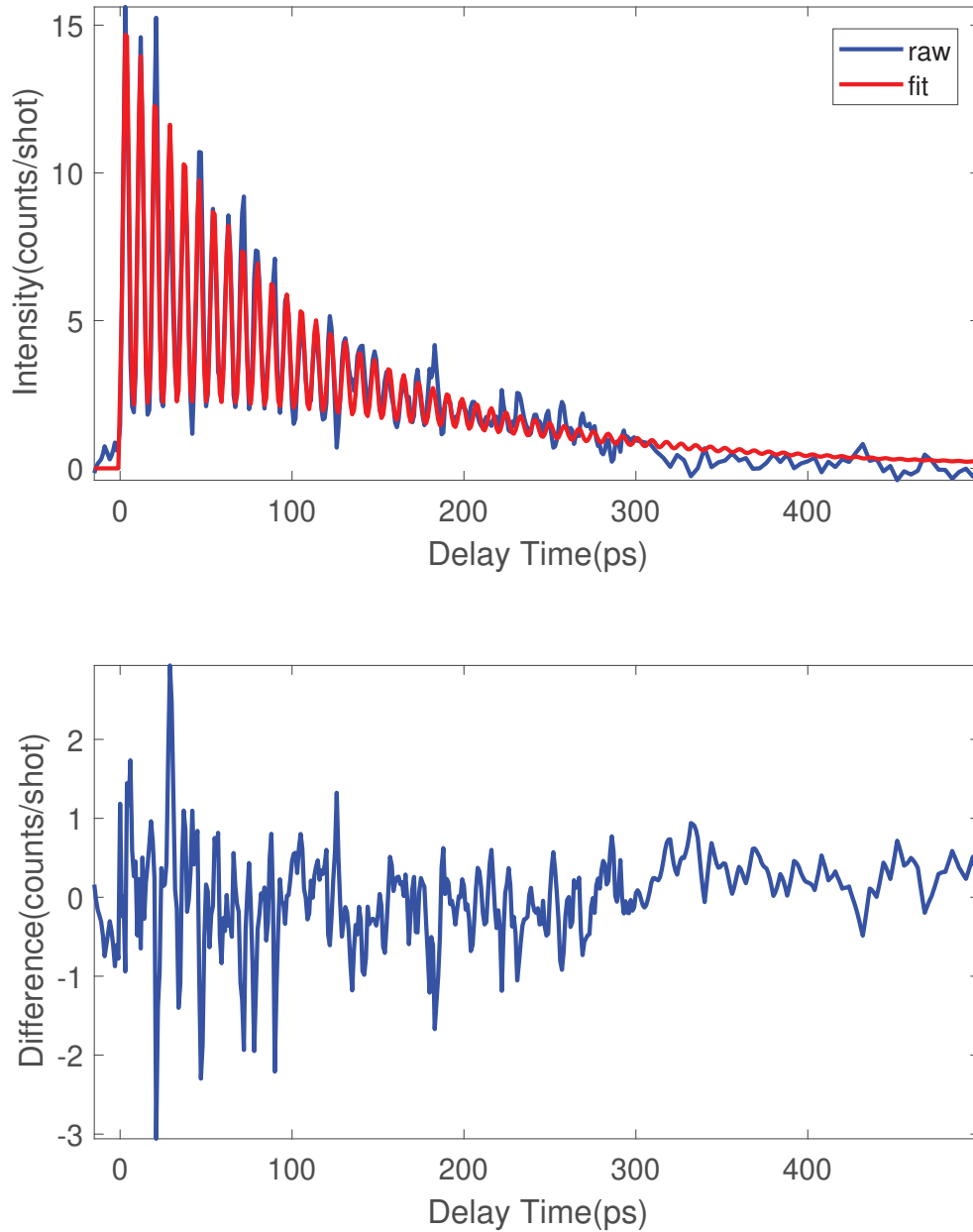


**Figure 4.27:** The top figure is the fitting of TG signal with equation (2.21) of the nanostructured amorphous Silicon Nitride at phonon wavelength of 84 nm, and the low figure is the difference between the raw data and the fitted data.

### 4.3.3 Phonon Wavelength at 106 nm

The experimental measured signal at phonon wavelength of 106 nm is shown in figure (4.28). We follow the same procedure described in sections (2.2.2) and (4.2.2) where the fit of the data to the exponential decay, reported in figure (4.28), give a thermal amplitude  $A_{106nm} = 9.9 \pm 0.4$ , and the decay time  $B_{106nm} = 203 \pm 11$  ps. The signal after subtraction of the exponential behavior is reported in figure (4.29).

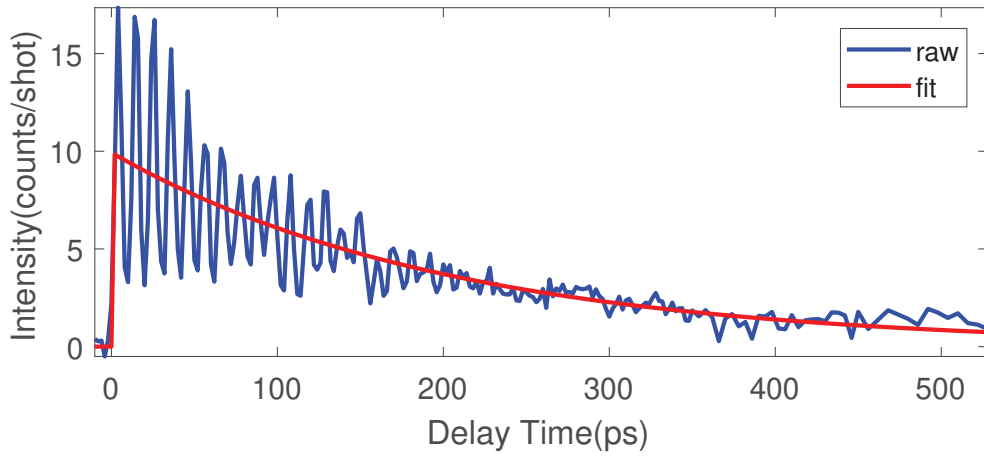


**Figure 4.28:** The blue line is the measured TG signal of nanostructured amorphous Silicon Nitride at phonon wavelength of 106 nm, and the red line is the fit of the TG signal with exponential decay.

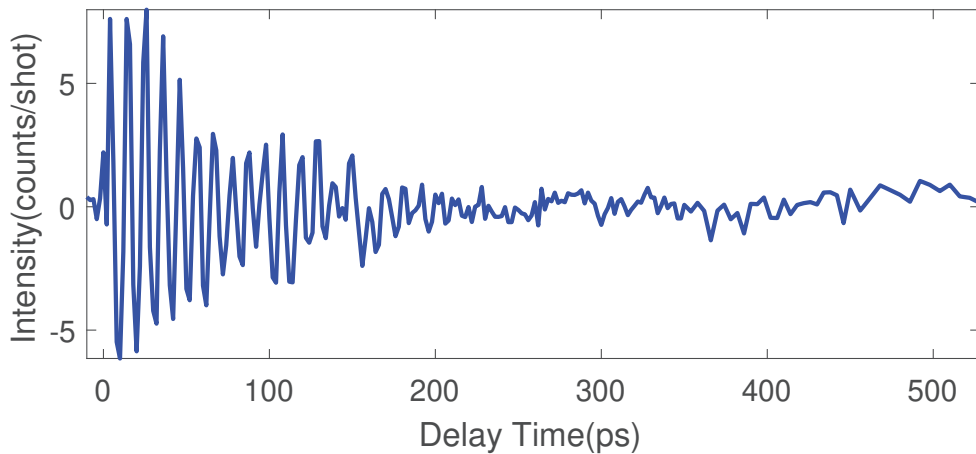


**Figure 4.29:** Pure oscillating signal as obtained after subtraction of the exponential decay from the TG signal.

A Fourier transform is applied to the subtracted data as shown in figure (4.30), we see one mode in the Fourier transform with frequency  $A=0.0963$  THz.

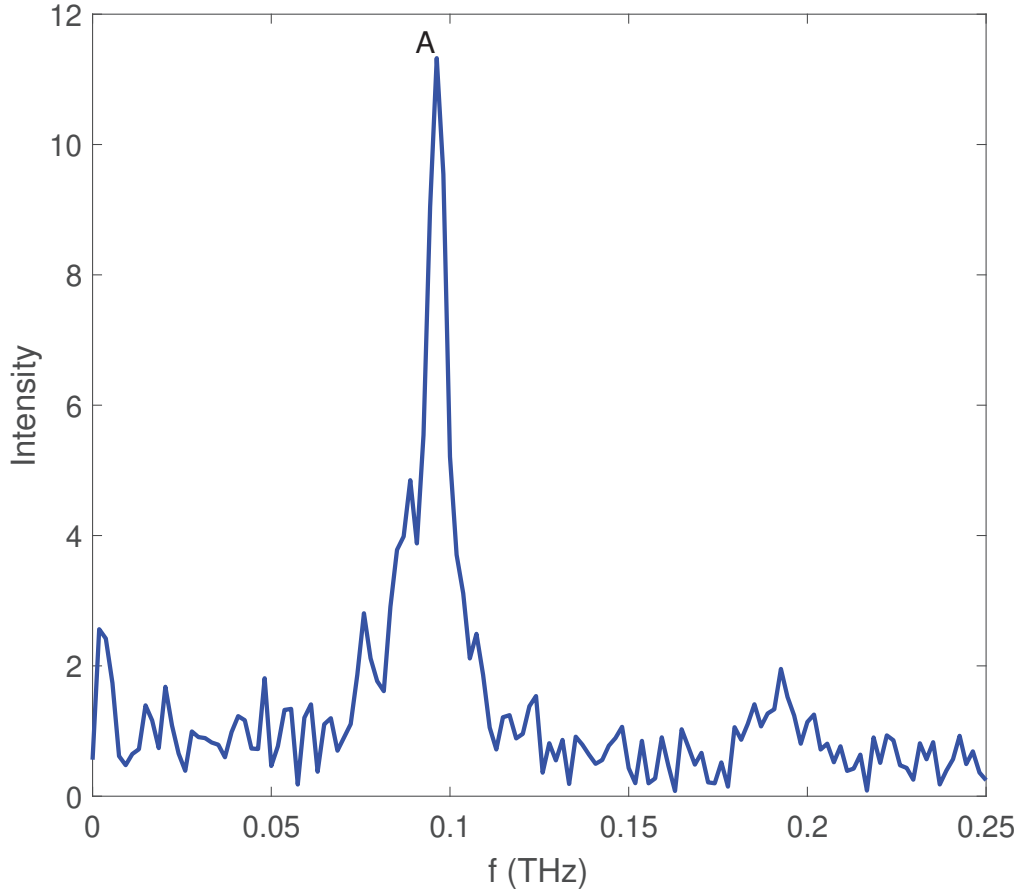


**Figure 4.30:** The Fourier transform of the subtracted data shown in figure (4.29), the peak of the Fourier transform has the following position  $A=0.0963$  THz.

The fit of the TG signal with the equation (2.21) is shown in figure (4.31.a). The fitted parameters are given as following, the thermal amplitude  $A_{th} = 3.00 \pm 0.02$ , the thermal decay  $\tau_{th} = 447 \pm 10$  ps, the phonon amplitude  $A_1 = 1.48 \pm 0.05$ , the life time  $\tau_1 = 91 \pm 5$  ps, and the frequency  $\nu_1 = 0.0963 \pm 0.0001$  THz. Like in the previous case, a fit with a single phonon mode is able to well reproduce the experimental signal. Data at times larger than 250 ps have been collected with a larger time step, loosing the detailed oscillations, which are too weak to be seen over the signal noise.

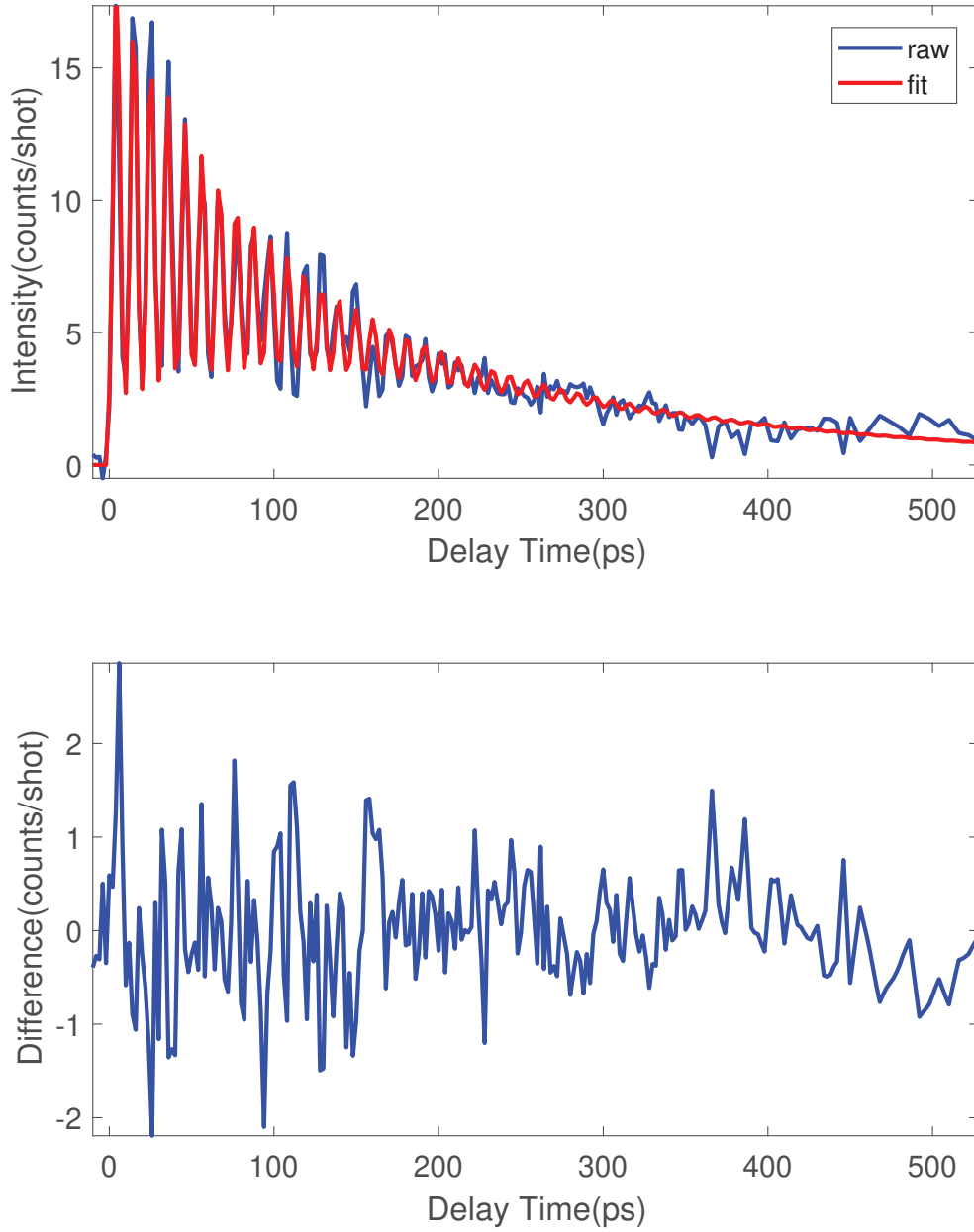


**Figure 4.31:** The top figure is the fitting of the TG signal with equation (2.21) of the nanostructured amorphous Silicon Nitride at phonon wavelength of 106 nm, and the low figure is the difference between the raw data and the fitted data.

### 4.3.4 Analysis

In this section, we want to understand the phonon dynamics in the nanostructured amorphous Silicon Nitride, the fitted parameters are summarized in table (4.3).

$\lambda$ (nm)	55	84	106
$A_{th}$	$8.67 \pm 0.04$	$2.69 \pm 0.03$	$3.00 \pm 0.02$
$\tau_{th}$ (ps)	$139 \pm 2$	$288 \pm 7$	$447 \pm 10$
$A_1$	$1.6 \pm 0.1$	$1.40 \pm 0.05$	$1.48 \pm 0.05$
$\tau_1$ (ps)	$40 \pm 5$	$104 \pm 6$	$91 \pm 5$
$\nu_1$ (THZ)	$0.1037 \pm 0.0003$	$0.11770 \pm 0.00009$	$0.0963 \pm 0.0001$
$A_2$	$0.41 \pm 0.07$		
$\tau_2$ (ps)	$120 \pm 50$		
$\nu_2$ (THZ)	$0.1225 \pm 0.0004$		
$A_3$	$2.4 \pm 0.2$		
$\tau_3$ (ps)	$42 \pm 4$		
$\nu_3$ (THZ)	$0.1729 \pm 0.0002$		
$A_4$	$2.3 \pm 0.3$		
$\tau_4$ (ps)	$11 \pm 2$		
$\nu_4$ (THZ)	$0.199 \pm 0.001$		

**Table 4.3:** Summary of the fitted parameters of the TG signal of nanostructured amorphous Silicon nitride membrane. The representation of each symbol is the following,  $\lambda$  phonon wavelength,  $A_{th}$  thermal amplitude,  $\tau_{th}$  thermal decay time,  $A_n$  the  $n^{th}$  phonon amplitude,  $\tau_n$  the  $n^{th}$  phonon life time, and  $\nu_n$  the  $n^{th}$  phonon frequency.

Preliminary calculations of phonon dispersions in the nanostructured material have been done by one of our collaborators by means of Finite Element Modelling, but only at low frequency the branch folding is well visible. At our experimental frequencies the calculations only show an almost continuum of optic modes, as a result of the multiple branch foldings. Surprisingly, if we use the simple calculation of Lamb dispersions for a homogeneous sample, as shown in figure (4.32), we can find a good match for all measured modes with a Young modulus of 230 GPa, comparable to the one found in the homogeneous sample. This is possibly because our wavelengths correspond to phonons beyond the Brillouin Zone border. We go on with the hypothesis then that we are observing the very same modes as in the homogeneous sample, which allow us to compare them one by one between the two samples. It is important to notice that due to the porosity, the effective density for the temperature raise calculation is 80% of the one of the homogeneous sample, leading to a temperature about 20% higher than in the homogeneous sample. Still, looking to the calculated temperatures, within exper-

imental uncertainty, the temperature difference can be neglected. Moreover, we have already seen that phonon frequencies are not very sensitive to temperature in the homogeneous sample. This seems to be confirmed in the nanostructured sample.

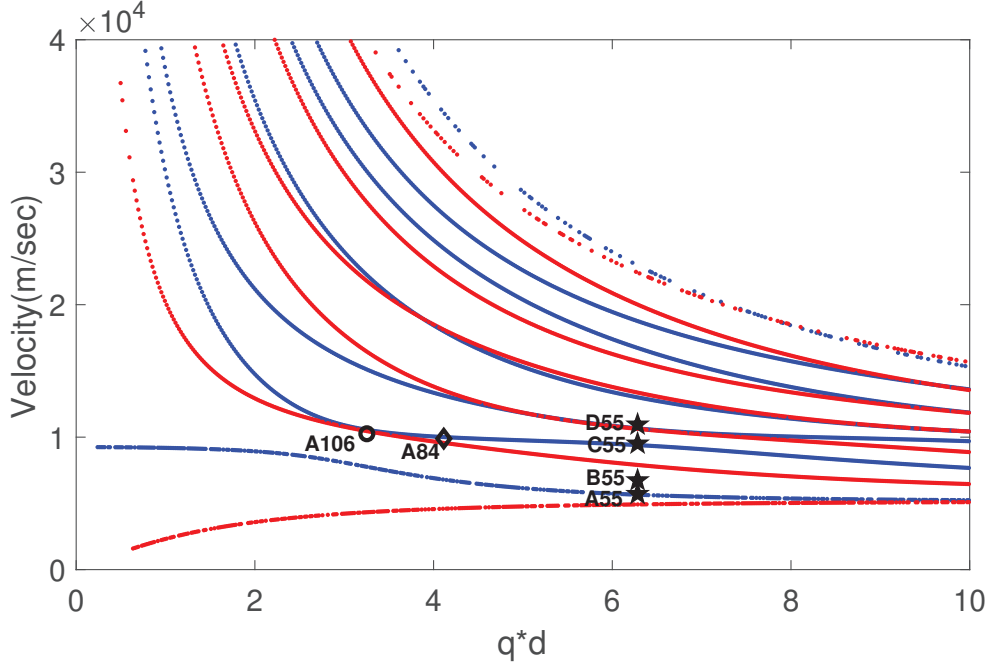


**Figure 4.32:** The Lamb waves dispersion curves are numerically calculated for  $v_l = 10131$  m/sec and  $v_s = 5687$  m/sec of the amorphous silicon nitride membrane to overlap the fitted phase velocities in black. Blue and red lines are symmetric and antisymmetric modes respectively, the black circle corresponds to phonon frequency at 106 nm, the black diamond corresponds to phonon frequencies at 84 nm, and the black pentagram corresponds to phonon frequencies at 55 nm.

In figure (4.33) we report the variation of the inverse of the thermal relaxation time vs the wavevector in the logarithmic scale. The thermal diffusivity is the half fitted slope, it is found that the thermal diffusivity from the fitting is  $850 \pm 220$  nm<sup>2</sup>/ns. This value is 10% smaller than in the homogeneous sample, although they are indistinguishable within error bars. The calculated fluence and the temperature increase in the sample at different wavelength is shown in table (4.4). A smaller value, if confirmed by further experiments, could indicate that at tens of nm scale heat diffusion is slightly slower and thus less efficient in presence of the nanostructure. Further studies are needed to establish the dependence of thermal relaxation time on the lengthscale at a given temperature.

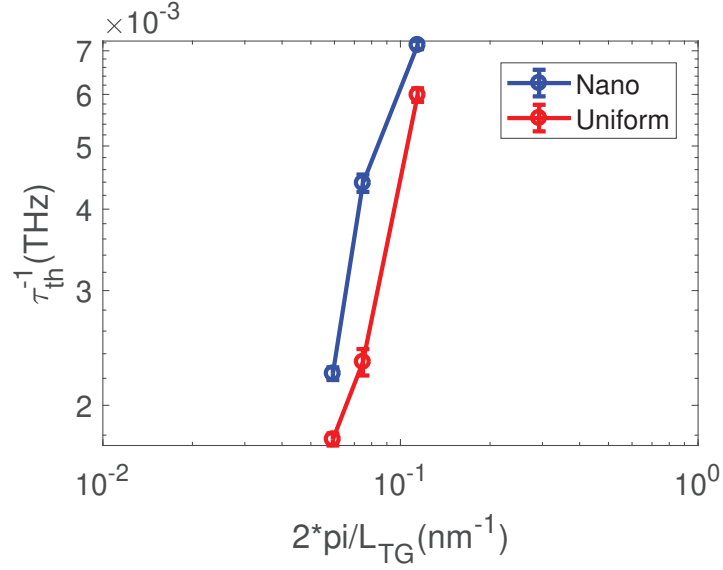


**Figure 4.33:** The variation of the inverse thermal relaxation time vs the wave vector of suspended membrane of the nanostructured (blue line) and uniform (red line) amorphous Silicon Nitride for the measured transient grating signal at  $L_{TG}=55, 84,$  and  $106$  nm.

Phonon wavelength (nm)	55	84	106
Pump Wavelength (nm)	26.6	39.9	52.3
Pump intensity ( $\mu J$ )	12	12.6	55.8
Pump fluence on the sample	$1.6 \pm 0.3$	$0.8 \pm 0.2$	$2.4 \pm 0.5$
$\Delta T_{max}$ ( $^{\circ}C$ )	$90 \pm 20$	$60 \pm 10$	$200 \pm 40$
Temperature ( $^{\circ}C$ )	$120 \pm 20$	$90 \pm 10$	$240 \pm 40$

**Table 4.4:** The calculation of the fluence of the pump beam on the sample, the maximum temperature rise, and the temperature in nanostructured amorphous Silicon Nitride suspended membrane.

We look now to the effect of the nanostructuration on phonon lifetime. To this aim, we report in figure (4.34.a) the phonon life time of the three phonons A106, A84, and B55 belonging to the second antisymmetric branch and one phonon C55 belonging to the third symmetric or antisymmetric branch for both the uniform and nanostructured samples. So, we observe an important reduction of the lifetime, which is of about a factor of 3 for the second antisymmetric branch, but

becomes as large as a factor of 10 for the phonon of the third symmetric or antisymmetric branch. Such a reduction can of course be ascribed to an additional scattering from interfaces, but it could also be the effect of temperature. Still, as said, the temperature difference between the two samples is within experimental uncertainty, thus we can neglect it and conclude that it is indeed the nanostructure which causes the lifetime reduction. From figure (4.34.a), it seems that the effect is stronger for larger wavelengths, and that the nanostructure flattens the wavelength dependence of the lifetime. The percentage of the phonon life time in nanostructured material with respect to the phonon life time in uniform material is shown in figure (4.34.b). It can be seen that the reduction is not uniform over a single phonon branch, but depends on the wavevector. A stronger effect is seen in the third symmetric or antisymmetric branch. The phonon of this branch could belong both to a symmetric and antisymmetric branch. The symmetry could thus play a role on the phonon lifetime reduction. Deeper studies are needed to understand how lifetime is reduced depending on the phonon branch and its symmetry. Finally, we need to remind that the fit of the phonon life time is strongly affected by the number of phonons added to the fitted TG signal, adding a larger uncertainty to the reported values..

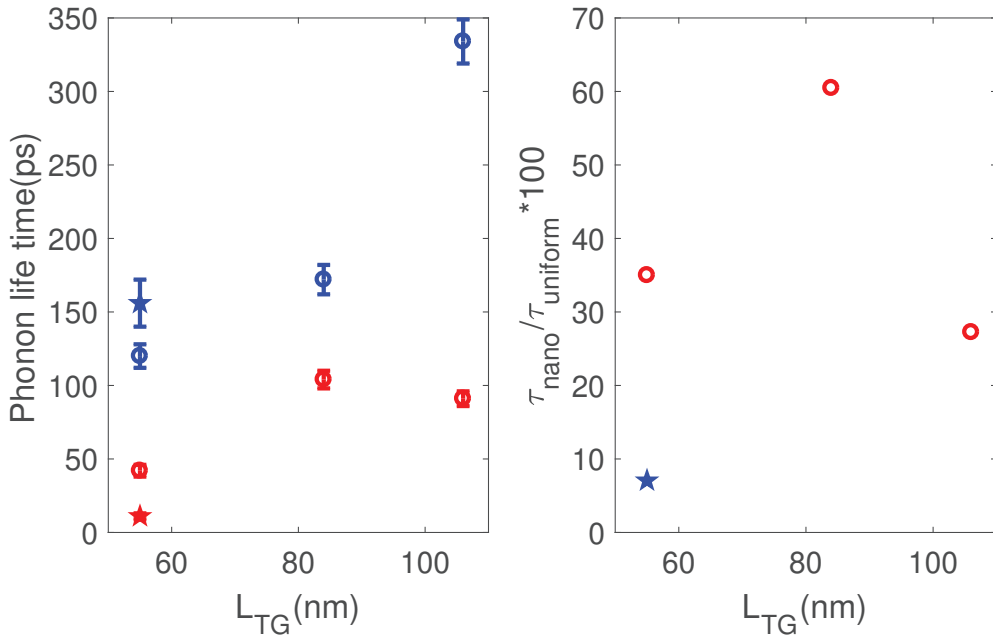


**Figure 4.34:** a) A comparison between the phonon life time vs phonon wavelength between the uniform sample (blue data) and the sample with nanostructuration (red data). b) The percentage of the phonon life time in nanostructured material with respect to the phonon life time in uniform material. The data with circle shape belong to the second antisymmetric branch, and the data with pentagram shape belong to the third symmetric or antisymmetric branch.

# Chapter 5

## Conclusions and Perspectives

In this thesis, using the thin film laser flash experiment, we have performed thermal conductivity measurements at a wide temperature range on amorphous Silicon Nitride grown by PECVD at different deposition temperatures. We have understood the sensitivity of this experiment depending on the thickness, the material of the thin film, and the material of the substrate. The thermal conductivity of the PECVD amorphous Silicon nitride at room temperature seems to be higher with respect to the increase of the deposition temperature which is mostly related to the increase of the Si-N bond content in the material. This observation helps in manipulating the thermal conductivity of the amorphous Silicon Nitride depending on the needed thermal property for a given application. Moreover, We have discovered an irreversible change of thermal conductivity independent of the deposition temperature at  $\sim 500$  K with a deep minimum of thermal conductivity around 673 K, then it increases to the unperturbed value. This behavior is explained by the release of the hydrogen at these temperatures [112].

There are several aspects of this project that could be tackled in the future. One possibility is performing hydrogen effusion measurements to our PECVD  $\text{SiN}_x$  to confirm the release of hydrogen at the temperature of our minimum, also it would be beneficial to study the effect of power of PECVD on the thermal conductivity measurements since Wan et al. have shown the dependence of the Si-N bond on the power of PECVD [120]. This may allow to access on a wide range of thermal conductivity values in amorphous  $\text{SiN}_x$ . Moreover, the challenge of coating the nanostructured amorphous  $\text{SiN}_x$  with a gold layer that does not fill the nanopores can be inspected. This is essential to allow the measurement of the thermal conductivity by the thin film laser flash experiment. Also, this will require a modification of the fitting model of the experiment to take into account the nanostructured material. In the low temperature measurement, the presence of a maximum at 250 K is still under investigation, this can be due to the activation of scattering mechanisms at this temperature which should be confirmed by measuring the stoichiometry and the bond organization in the material.

To understand the phonon dynamics at the nanoscale, we have measured the transient grating signal at three different phonon wavelength of 55, 84, and 106 nm on the uniform and the nanostructured LPCVD amorphous Silicon Nitride. For having a better understanding of the thermal relaxation time, it is useful to measure at larger wavelengths and at different temperatures to see the effect of the increase of temperature on the measurement, also study the effect of the pump intensity on the thermal relaxation time at different phonon wavelengths gives an indication about the effect of the maximum temperature rise on the measurement. In the phonon lifetime study, it is better to have more measurements at different phonon wavelengths for good visualization of the dependence of the phonon life time on the phonon frequency. From a general view, the phonon life time in the nanostructured material is reduced with respect to the phonon life time in the uniform material. Further studies of the phonon life time on the material with different nanostructuration periodicity in a wide range of phonon wavelengths at different temperatures can build a larger understanding of the dependence of the phonon life time on the nanostructuration.

# Appendix A

## Background Image Code

```
1 function y=modified_background(xa,yb,a,b,im,scale)
2
3 % xa center of the ellipse
4 % yb center of the ellipse
5 % width of the ellipse is 2*a
6 % height of the ellipse is 2*b
7 % im is the chosen image to create its background
8 % scale is an option if the the final im needed to be
   scaled
9
10 m=length(im(:,1));% number of rows mean height
11 n=length(im(1,:));% number of column means width
12
13 % This double is to choose the ROI
14 for i=1:m
15     for j=1:n
16
17         if ((j-xa)^2/a^2+(i-yb)^2/b^2<=1)
18             roi(i,j)=0;
19             roit(i,j)=1;
20         else
21             roi(i,j)=1;
22             roit(i,j)=0;
23         end
24     end
25 end
26 end
27
28 backgrd=im.*roi;
```

```

29
30 for i=1:m
31     count=0;
32     sumd=0;
33     for j=1:n
34
35         if (backgrd(i ,j)==0)
36
37             count=count+1;
38
39         end
40
41     end
42
43     if (count~=0)
44
45         for j=1:n
46
47             sumd=sumd+backgrd(i ,j);
48
49         end
50
51         average=sumd/(n-count);
52
53         for j=1:n
54
55             if (backgrd(i ,j)==0)
56                 newbackgrd(i ,j)=average;
57             else
58                 newbackgrd(i ,j)=backgrd(i ,j);
59             end
60
61         end
62
63     elseif (count==0)
64
65         for j=1:n
66
67             newbackgrd(i ,j)=backgrd(i ,j);
68
69         end
70     end
71 end

```

```
72
73 end
74
75 signalsubbkg=im-newbackgrd;
76 y=(signalsubbkg/scale)+newbackgrd;
77
78 end
```

# Bibliography

- [1] C. Holman, "Sources of air pollution," in *Air pollution and health*, pp. 115–148, Elsevier, 1999.
- [2] A. Fujishima, T. N. Rao, and D. A. Tryk, "Titanium dioxide photocatalysis," *Journal of photochemistry and photobiology C: Photochemistry reviews*, vol. 1, no. 1, pp. 1–21, 2000.
- [3] B. F. Bessac and S.-E. Jordt, "Sensory detection and responses to toxic gases: mechanisms, health effects, and countermeasures," *Proceedings of the American Thoracic Society*, vol. 7, no. 4, pp. 269–277, 2010.
- [4] J. Low, B. Cheng, and J. Yu, "Surface modification and enhanced photocatalytic CO<sub>2</sub> reduction performance of TiO<sub>2</sub>: a review," *Applied Surface Science*, vol. 392, pp. 658–686, 2017.
- [5] A. Fujishima and K. Honda, "Electrochemical photolysis of water at a semiconductor electrode," *nature*, vol. 238, no. 5358, pp. 37–38, 1972.
- [6] S. Malato, P. Fernández-Ibáñez, M. I. Maldonado, J. Blanco, and W. Gernjak, "Decontamination and disinfection of water by solar photocatalysis: recent overview and trends," *Catalysis today*, vol. 147, no. 1, pp. 1–59, 2009.
- [7] Y. Boyjoo, H. Sun, J. Liu, V. K. Pareek, and S. Wang, "A review on photocatalysis for air treatment: From catalyst development to reactor design," *Chemical engineering journal*, vol. 310, pp. 537–559, 2017.
- [8] M. N. Chong, B. Jin, C. W. Chow, and C. Saint, "Recent developments in photocatalytic water treatment technology: a review," *Water research*, vol. 44, no. 10, pp. 2997–3027, 2010.
- [9] G. K. Mor, O. K. Varghese, M. Paulose, K. Shankar, and C. A. Grimes, "A review on highly ordered, vertically oriented TiO<sub>2</sub> nanotube arrays: Fabrication, material properties, and solar energy applications," *Solar Energy Materials and Solar Cells*, vol. 90, no. 14, pp. 2011–2075, 2006.

- [10] X. Zhang and C. P. Grigoropoulos, “Thermal conductivity and diffusivity of free-standing silicon nitride thin films,” *Review of scientific instruments*, vol. 66, no. 2, pp. 1115–1120, 1995.
- [11] R. M. De La Rue and C. Seassal, “Photonic crystal devices: some basics and selected topics,” *Laser & Photonics Reviews*, vol. 6, no. 4, pp. 564–597, 2012.
- [12] L. Zhou, D. F. Swearer, C. Zhang, H. Robotjazi, H. Zhao, L. Henderson, L. Dong, P. Christopher, E. A. Carter, P. Nordlander, *et al.*, “Quantifying hot carrier and thermal contributions in plasmonic photocatalysis,” *Science*, vol. 362, no. 6410, pp. 69–72, 2018.
- [13] H. Luo, A. Gravouil, V. Giordano, and A. Tanguy, “Thermal transport in a 2d nanophononic solid: Role of bi-phasic materials properties on acoustic attenuation and thermal diffusivity,” *Nanomaterials*, vol. 9, no. 10, p. 1471, 2019.
- [14] G. Chen, *Nanoscale energy transport and conversion: a parallel treatment of electrons, molecules, phonons, and photons*. Oxford University Press, 2005.
- [15] S. H. Simon, *The Oxford solid state basics*. Oxford University Press, 2013.
- [16] G. P. Srivastava, *The physics of phonons*. Routledge, 2019.
- [17] D. Royer and E. Dieulesaint, *Elastic waves in solids II: generation, acousto-optic interaction, applications*. Springer Science & Business Media, 1999.
- [18] B. D. Rouhani and E. Khourdifi, “Localised and extended acoustic waves in superlattices light scattering by longitudinal phonons,” in *Light Scattering in Semiconductor Structures and Superlattices*, pp. 139–158, Springer, 1991.
- [19] I. Psarobas, N. Papanikolaou, N. Stefanou, B. Djafari-Rouhani, B. Bonello, and V. Laude, “Enhanced acousto-optic interactions in a one-dimensional phoxonic cavity,” *Physical Review B*, vol. 82, no. 17, p. 174303, 2010.
- [20] S. G. Johnson, M. Ibanescu, M. Skorobogatiy, O. Weisberg, J. Joannopoulos, and Y. Fink, “Perturbation theory for maxwell’s equations with shifting material boundaries,” *Physical review E*, vol. 65, no. 6, p. 066611, 2002.
- [21] B. Djafari-Rouhani, S. El-Jallal, and Y. Pennec, “Phoxonic crystals and cavity optomechanics,” *Comptes Rendus Physique*, vol. 17, no. 5, pp. 555–564, 2016.

- [22] J. Chan, A. H. Safavi-Naeini, J. T. Hill, S. Meenehan, and O. Painter, “Optimized optomechanical crystal cavity with acoustic radiation shield,” *Applied Physics Letters*, vol. 101, no. 8, p. 081115, 2012.
- [23] A. Gaucher, A. Cattoni, C. Dupuis, W. Chen, R. Cariou, M. Foldyna, L. Lalouat, E. Drouard, C. Seassal, P. Roca i Cabarrocas, *et al.*, “Ultrathin epitaxial silicon solar cells with inverted nanopyramid arrays for efficient light trapping,” *Nano letters*, vol. 16, no. 9, pp. 5358–5364, 2016.
- [24] Y. Shi, W. Li, A. Raman, and S. Fan, “Optimization of multilayer optical films with a memetic algorithm and mixed integer programming,” *ACS Photonics*, vol. 5, no. 3, pp. 684–691, 2017.
- [25] C. Zhu, W. Zhou, J. Fang, Y. Ni, L. Fang, C. Lu, Z. Xu, and Z. Kang, “Enhancement of fluorescent emission in photonic crystal film and application in photocatalysis,” *Nanotechnology*, vol. 29, no. 4, p. 045601, 2017.
- [26] L. Yang, N. Yang, and B. Li, “Extreme low thermal conductivity in nanoscale 3d si phononic crystal with spherical pores,” *Nano letters*, vol. 14, no. 4, pp. 1734–1738, 2014.
- [27] M. Ghasemi Baboly, S. Alaie, C. Reinke, I. El-Kady, and Z. C. Leseman, “Ultra-high frequency, high q/volume micromechanical resonators in a planar aln phononic crystal,” *Journal of Applied Physics*, vol. 120, no. 3, p. 034502, 2016.
- [28] T. Damart, V. Giordano, and A. Tanguy, “Nanocrystalline inclusions as a low-pass filter for thermal transport in a-si,” *Physical Review B*, vol. 92, no. 9, p. 094201, 2015.
- [29] J. Callaway, “Model for lattice thermal conductivity at low temperatures,” *Physical Review*, vol. 113, no. 4, p. 1046, 1959.
- [30] S. Pailhès, V. M. Giordano, P.-F. Lory, M. De Boissieu, and H. Euchner, “X-rays and neutrons spectroscopy for the investigation of individual phonons properties in crystalline and amorphous solids,” in *Nanostructured Semiconductors*, pp. 517–563, Jenny Stanford Publishing, 2017.
- [31] K. Termentzidis, *Nanostructured semiconductors: amorphization and thermal properties*. CRC Press, 2017.
- [32] M. Biercuk, M. C. Llaguno, M. Radosavljevic, J. Hyun, A. T. Johnson, and J. E. Fischer, “Carbon nanotube composites for thermal management,” *Applied physics letters*, vol. 80, no. 15, pp. 2767–2769, 2002.

- [33] K. Termentzidis, V. M. Giordano, M. Katsikini, E. Paloura, G. Pernot, M. Verdier, D. Lacroix, I. Karakostas, and J. Kioseoglou, “Enhanced thermal conductivity in percolating nanocomposites: a molecular dynamics investigation,” *Nanoscale*, vol. 10, no. 46, pp. 21732–21741, 2018.
- [34] K. Ruan, Y. Guo, Y. Tang, Y. Zhang, J. Zhang, M. He, J. Kong, and J. Gu, “Improved thermal conductivities in polystyrene nanocomposites by incorporating thermal reduced graphene oxide via electrospinning-hot press technique,” *Composites Communications*, vol. 10, pp. 68–72, 2018.
- [35] L. Yanqing, *Thermal engineering in an epitaxial nanostructured germanium semiconductor*. PhD thesis, PhD thesis, 2015.
- [36] X. Yang, L. Tang, Y. Guo, C. Liang, Q. Zhang, K. Kou, and J. Gu, “Improvement of thermal conductivities for pps dielectric nanocomposites via incorporating nh<sub>2</sub>-poss functionalized nbn fillers,” *Composites Part A: Applied Science and Manufacturing*, vol. 101, pp. 237–242, 2017.
- [37] C.-W. Nan, R. Birringer, D. R. Clarke, and H. Gleiter, “Effective thermal conductivity of particulate composites with interfacial thermal resistance,” *Journal of Applied Physics*, vol. 81, no. 10, pp. 6692–6699, 1997.
- [38] R. Yang, G. Chen, and M. S. Dresselhaus, “Thermal conductivity modeling of core-shell and tubular nanowires,” *Nano letters*, vol. 5, no. 6, pp. 1111–1115, 2005.
- [39] A. Minnich and G. Chen, “Modified effective medium formulation for the thermal conductivity of nanocomposites,” *Applied Physics Letters*, vol. 91, no. 7, p. 073105, 2007.
- [40] J.-B. Vaney, A. Piarristeguy, V. Ohorodniichuck, O. Ferry, A. Pradel, E. Aleno, J. Monnier, E. B. Lopes, A. Gonçalves, G. Delaizir, *et al.*, “Effective medium theory based modeling of the thermoelectric properties of composites: comparison between predictions and experiments in the glass-crystal composite system si 10 as 15 te 75-bi 0.4 sb 1.6 te 3,” *Journal of Materials Chemistry C*, vol. 3, no. 42, pp. 11090–11098, 2015.
- [41] A. Tlili, V. Giordano, Y. Beltukov, P. Desmarchelier, S. Merabia, and A. Tanguy, “Enhancement and anticipation of the ioffe-regel crossover in amorphous/nanocrystalline composites,” *Nanoscale*, 2019.
- [42] M.-S. Jeng, R. Yang, D. Song, and G. Chen, “Monte carlo simulation of the thermal conductivity and phonon transport in nanocomposites,” in *ASME 2005 Pacific Rim Technical Conference and Exhibition on Integration and Packaging of MEMS, NEMS, and Electronic Systems collocated with the*

*ASME 2005 Heat Transfer Summer Conference*, pp. 2207–2215, American Society of Mechanical Engineers Digital Collection, 2005.

- [43] L. Yang, N. Yang, and B. Li, “Reduction of thermal conductivity by nanoscale 3d phononic crystal,” *Scientific reports*, vol. 3, no. 1, pp. 1–5, 2013.
- [44] B. A. Auld, *Acoustic fields and waves in solids*. 1973.
- [45] M. H. Sadd, *Elasticity: theory, applications, and numerics*. Academic Press, 2009.
- [46] S. Palaz, H. Koc, A. M. Mamedov, and E. Ozbay, “Topological insulators: Electronic band structure and spectroscopy,” in *IOP Conference Series: Materials Science and Engineering*, vol. 175, p. 012004, IOP Publishing, 2017.
- [47] G. Carlotti, “Elastic characterization of transparent and opaque films, multilayers and acoustic resonators by surface brillouin scattering: a review,” *Applied Sciences*, vol. 8, no. 1, p. 124, 2018.
- [48] G. Carlotti, G. Socino, H. Xia, Z. Li, W. Zhang, X. Qu, K. Chen, and X. Zhang, “Study of amorphous silicon nitride films by brillouin spectroscopy,” *MRS Online Proceedings Library Archive*, vol. 336, 1994.
- [49] B. Graczykowski, M. Sledzinska, F. Alzina, J. Gomis-Bresco, J. Reparaz, M. Wagner, and C. S. Torres, “Phonon dispersion in hypersonic two-dimensional phononic crystal membranes,” *Physical Review B*, vol. 91, no. 7, p. 075414, 2015.
- [50] M. R. Wagner, B. Graczykowski, J. S. Reparaz, A. El Sachat, M. Sledzinska, F. Alzina, and C. M. Sotomayor Torres, “Two-dimensional phononic crystals: Disorder matters,” *Nano letters*, vol. 16, no. 9, pp. 5661–5668, 2016.
- [51] A. Iskandar, A. Gwiazda, Y. Huang, M. Kazan, A. Bruyant, M. Tabbal, and G. Lerondel, “Modification of the phonon spectrum of bulk si through surface nanostructuring,” *Journal of Applied Physics*, vol. 120, no. 9, p. 095106, 2016.
- [52] D. G. Cahill, “Analysis of heat flow in layered structures for time-domain thermoreflectance,” *Review of scientific instruments*, vol. 75, no. 12, pp. 5119–5122, 2004.
- [53] A. Feldman, “Algorithm for solutions of the thermal diffusion equation in a stratified medium with a modulated heating source,” *High Temperatures. High Pressures*, vol. 31, no. 3, pp. 293–298, 1999.

- [54] M. Noginov, G. Zhu, and V. Gavrilenko, “Sensitized nonlinear emission of gold nanoparticles,” *Optics express*, vol. 15, no. 24, pp. 15648–15655, 2007.
- [55] P. Raad, P. Komarov, and M. Burzo, “technical brief: thermo-reflectance thermography for submicron temperature measurements,” *Electronics Cooling*, vol. 14, no. 1, p. 28, 2008.
- [56] S.-M. Lee and D. G. Cahill, “Heat transport in thin dielectric films,” *Journal of applied physics*, vol. 81, no. 6, pp. 2590–2595, 1997.
- [57] A. Al Mohtar, G. Tessier, R. Ritasalo, M. Matvejeff, J. Stormonth-Darling, P. Dobson, P.-O. Chapuis, S. Gomès, and J.-P. Roger, “Thickness-dependent thermal properties of amorphous insulating thin films measured by photoreflectance microscopy,” *Thin Solid Films*, vol. 642, pp. 157–162, 2017.
- [58] D. M. Hamby, “A review of techniques for parameter sensitivity analysis of environmental models,” *Environmental monitoring and assessment*, vol. 32, no. 2, pp. 135–154, 1994.
- [59] H. S. Carslaw and J. C. Jaeger, “Conduction of heat in solids,” *Oxford: Clarendon Press, 1959, 2nd ed.*, p. 282, 1959.
- [60] D. Maillet, S. André, J. Batsale, A. Degiovanni, and C. Moyne, “Solving the heat equation through integral transforms,” *Edition Wiley*, 2000.
- [61] H. S. Carslaw and J. C. Jaeger, “Conduction of heat in solids,” *Oxford: Clarendon Press, 1959, 2nd ed.*, 1959.
- [62] P. Jiang, X. Qian, and R. Yang, “Tutorial: Time-domain thermoreflectance (tdtr) for thermal property characterization of bulk and thin film materials,” *Journal of Applied Physics*, vol. 124, no. 16, p. 161103, 2018.
- [63] R. N. Bracewell, “The fourier transform and its applications, mcgraw-hill series in electrical and computer engineering. circuits and systems,” 2000.
- [64] Y. Ohson, G. Wu, J. Dryden, F. Zok, and A. Majumdar, “Optical measurement of thermal contact conductance between wafer-like thin solid samples,” 1999.
- [65] C. Masciovecchio, A. Battistoni, E. Giangristostomi, F. Bencivenga, E. Principi, R. Mincigrucci, R. Cucini, A. Gessini, F. D’Amico, R. Borghes, *et al.*, “Eis: the scattering beamline at fermi,” *Journal of synchrotron radiation*, vol. 22, no. 3, pp. 553–564, 2015.
- [66] R. W. Boyd in *Nonlinear Optics (Fourth Edition)* (R. W. Boyd, ed.), Academic Press, fourth edition ed., 2020.

- [67] F. Bencivenga, S. Baroni, C. Carbone, M. Chergui, M. Danailov, G. De Ninno, M. Kiskinova, L. Raimondi, C. Svetina, and C. Masciovecchio, “Nanoscale dynamics by short-wavelength four wave mixing experiments,” *New Journal of Physics*, vol. 15, no. 12, p. 123023, 2013.
- [68] A. Milloch, *Nanoscale Thermoelasticity in Mechanically Confined Systems*. PhD thesis, University of Trieste, 2020.
- [69] K. A. Nelson, R. D. Miller, D. Lutz, and M. Fayer, “Optical generation of tunable ultrasonic waves,” *Journal of Applied Physics*, vol. 53, no. 2, pp. 1144–1149, 1982.
- [70] J. Knoester and S. Mukamel, “Transient gratings, four-wave mixing and polariton effects in nonlinear optics,” *Physics reports*, vol. 205, no. 1, pp. 1–58, 1991.
- [71] F. Bencivenga, R. Mincigrucci, F. Capotondi, L. Foglia, D. Naumenko, A. Maznev, E. Pedersoli, A. Simoncig, F. Caporaletti, V. Chiloyan, *et al.*, “Nanoscale transient gratings excited and probed by extreme ultraviolet femtosecond pulses,” *Science advances*, vol. 5, no. 7, p. eaaw5805, 2019.
- [72] R. Mincigrucci, L. Foglia, D. Naumenko, E. Pedersoli, A. Simoncig, R. Cucini, A. Gessini, M. Kiskinova, G. Kurdi, N. Mahne, *et al.*, “Advances in instrumentation for fel-based four-wave-mixing experiments,” *Nuclear Instruments and Methods in Physics Research Section A: Accelerators, Spectrometers, Detectors and Associated Equipment*, vol. 907, pp. 132–148, 2018.
- [73] A. Maznev, F. Bencivenga, A. Cannizzo, F. Capotondi, R. Cucini, R. Duncan, T. Feurer, T. Frazer, L. Foglia, H.-M. Frey, *et al.*, “Generation of coherent phonons by coherent extreme ultraviolet radiation in a transient grating experiment,” *Applied physics letters*, vol. 113, no. 22, p. 221905, 2018.
- [74] F. Bencivenga, R. Cucini, F. Capotondi, A. Battistoni, R. Mincigrucci, E. Giangrisostomi, A. Gessini, M. Manfredda, I. Nikolov, E. Pedersoli, *et al.*, “Four-wave mixing experiments with extreme ultraviolet transient gratings,” *Nature*, vol. 520, no. 7546, p. 205, 2015.
- [75] P. Ruello and V. E. Gusev, “Physical mechanisms of coherent acoustic phonons generation by ultrafast laser action,” *Ultrasonics*, vol. 56, pp. 21–35, 2015.
- [76] D. Schick, M. Herzog, H. Wen, P. Chen, C. Adamo, P. Gaal, D. G. Schlom, P. G. Evans, Y. Li, and M. Bargheer, “Localized excited charge carriers generate ultrafast inhomogeneous strain in the multiferroic bifeo 3,” *Physical review letters*, vol. 112, no. 9, p. 097602, 2014.

- [77] A. Cameron, P. Riblet, and A. Miller, "Spin gratings and the measurement of electron drift mobility in multiple quantum well semiconductors," *Physical review letters*, vol. 76, no. 25, p. 4793, 1996.
- [78] J. F. Nye *et al.*, *Physical properties of crystals: their representation by tensors and matrices*. Oxford university press, 1985.
- [79] V. Gusev, P. Picart, D. Mounier, and J.-M. Breteau, "On the possibility of ultrashort shear acoustic pulse excitation due to the laser-induced electrostrictive effect," *Optics communications*, vol. 204, no. 1-6, pp. 229–236, 2002.
- [80] H. J. MARIS, "6 - interaction of sound waves with thermal phonons in dielectric crystals," in *Principles and Methods* (W. P. MASON and R. THURSTON, eds.), vol. 8 of *Physical Acoustics*, pp. 279–345, Academic Press, 1971.
- [81] Y.-X. Yan and K. A. Nelson, "Impulsive stimulated light scattering. i. general theory," *The Journal of chemical physics*, vol. 87, no. 11, pp. 6240–6256, 1987.
- [82] Y.-X. Yan, L.-T. Cheng, and K. A. Nelson, "The temperature-dependent distribution of relaxation times in glycerol: Time-domain light scattering study of acoustic and mountain-mode behavior in the 20 mhz–3 ghz frequency range," *The Journal of chemical physics*, vol. 88, no. 10, pp. 6477–6486, 1988.
- [83] A. R. Duggal and K. A. Nelson, "Picosecond–microsecond structural relaxation dynamics in polypropylene glycol: impulsive stimulated light-scattering experiments," *The Journal of chemical physics*, vol. 94, no. 12, pp. 7677–7688, 1991.
- [84] M. Duffy and W. Kern, "Preparation, properties and applications of chemically vapor deposited silicon nitride films," *RCA Revicew*, vol. 31, no. 4, pp. 742–753, 1970.
- [85] A. Sinha, H. Levinstein, T. Smith, G. Quintana, and S. Haszko, "Reactive plasma deposited si-n films for mos-lsi passivation," *Journal of the Electrochemical Society*, vol. 125, no. 4, p. 601, 1978.
- [86] S. Hasegawa, Y. Amano, T. Inokuma, and Y. Kurata, "Relationship between the stress and bonding properties of amorphous sin x: H films," *Journal of applied physics*, vol. 72, no. 12, pp. 5676–5681, 1992.
- [87] D. B. and J. Regolini and P. Morin, "Hydrogen desorption and diffusion in pecvd silicon nitride. application to passivation of cmos active pixel sensors," *Microelectronic Engineering*, vol. 84, p. 2169, 2007.

- [88] L. Wang, W. Xie, D. V. Thourhout, Y. Zhang, H. Yu, and S. Wang, “Non-linear silicon nitride waveguides based on a pecvd deposition platform,” *Opt. Express*, vol. 26, p. 9645, 2018.
- [89] A. F. Braña, H. Gupta, R. K. Bommali, P. Srivastava, S. Ghosh, and R. P. Casero, “Enhancing efficiency of c-si solar cell by coating nano structured silicon rich silicon nitride films,” *Thin Solid Films*, vol. 662, pp. 21–26, sep 2018.
- [90] N. Ibaraki and H. Fritzsche, “Properties of amorphous semiconducting a- s i: H a- si n x: H multilayer films and of a- si n x: H alloys,” *Physical Review B*, vol. 30, no. 10, p. 5791, 1984.
- [91] A. Lowe, M. Powell, and S. Elliott, “The electronic properties of plasma-deposited films of hydrogenated amorphous sin x ( $0 < x < 1.2$ ),” *Journal of applied physics*, vol. 59, no. 4, pp. 1251–1258, 1986.
- [92] S. Hasegawa, M. Matsuda, and Y. Kurata, “Si-h and n-h vibrational properties in glow-discharge amorphous sin x: H films ( $0 < x < 1.55$ ),” *Applied physics letters*, vol. 57, no. 21, pp. 2211–2213, 1990.
- [93] S. Hasegawa, M. Matsuda, and Y. Kurata, “Bonding configuration and defects in amorphous sin x: H films,” *Applied physics letters*, vol. 58, no. 7, pp. 741–743, 1991.
- [94] A. Stoffel, A. Kovacs, W. Kronast, and B. Müller, “Lpcvd against pecvd for micromechanical applications,” *Journal of Micromechanics and Microengineering*, vol. 6, no. 1, p. 1, 1996.
- [95] N. Jehanathan, *Thermal stability of plasma enhanced chemical vapor deposited silicon nitride thin films*. University of Western Australia, 2007.
- [96] S. Bae, D. G. Farber, and S. J. Fonash, “Characteristics of low-temperature silicon nitride (sinx: H) using electron cyclotron resonance plasma,” *Solid-State Electronics*, vol. 44, no. 8, pp. 1355–1360, 2000.
- [97] M. T. Soh, N. Savvides, C. A. Musca, M. P. Martyniuk, and L. Faraone, “Local bonding environment of plasma deposited nitrogen-rich silicon nitride thin films,” *Journal of applied physics*, vol. 97, no. 9, p. 093714, 2005.
- [98] A. E. Kaloyeros, F. A. Jové, J. Goff, and B. Arkles, “Silicon nitride and silicon nitride-rich thin film technologies: Trends in deposition techniques and related applications,” *ECS Journal of Solid State Science and Technology*, vol. 6, no. 10, p. P691, 2017.

- [99] A. E. Kaloyeros, Y. Pan, J. Goff, and B. Arkles, “Review—silicon nitride and silicon nitride-rich thin film technologies: State-of-the-art processing technologies, properties, and applications,” *ECS Journal of Solid State Science and Technology*, vol. 9, p. 063006, aug 2020.
- [100] M. C. Wingert, J. Zheng, S. Kwon, and R. Chen, “Thermal transport in amorphous materials: a review,” *Semiconductor Science and Technology*, vol. 31, no. 11, p. 113003, 2016.
- [101] A. Griffin Jr, F. Brotzen, and P. Loos, “The effective transverse thermal conductivity of amorphous  $\text{Si}_3\text{N}_4$  thin films,” *Journal of applied physics*, vol. 76, no. 7, pp. 4007–4011, 1994.
- [102] A. Sikora, H. Ftouni, J. Richard, C. Hébert, D. Eon, F. Omnes, and O. Bourgeois, “Highly sensitive thermal conductivity measurements of suspended membranes (sin and diamond) using a  $3\omega$ -völklein method,” *Review of Scientific Instruments*, vol. 83, no. 5, p. 054902, 2012.
- [103] A. Sikora, H. Ftouni, J. Richard, C. Hébert, D. Eon, F. Omnès, and O. Bourgeois, “Erratum: “highly sensitive thermal conductivity measurements of suspended membranes (sin and diamond) using a  $3\omega$ -völklein method” [rev. sci. instrum. 83, 054902 (2012)],” *Review of Scientific Instruments*, vol. 84, no. 2, p. 029901, 2013.
- [104] A. Jain and K. E. Goodson, “Measurement of the thermal conductivity and heat capacity of freestanding shape memory thin films using the  $3\omega$  method,” *Journal of Heat Transfer*, vol. 130, no. 10, 2008.
- [105] M. P. Hughey and R. F. Cook, “Massive stress changes in plasma-enhanced chemical vapor deposited silicon nitride films on thermal cycling,” *thin solid films*, vol. 460, no. 1-2, pp. 7–16, 2004.
- [106] M. Maeda and M. Itsumi, “Thermal dissociation process of hydrogen atoms in plasma-enhanced chemical vapor deposited silicon nitride films,” *Journal of applied physics*, vol. 84, no. 9, pp. 5243–5247, 1998.
- [107] H. Stein, V. Wells, and R. Hampy, “Properties of plasma-deposited silicon nitride,” *Journal of the Electrochemical Society*, vol. 126, no. 10, p. 1750, 1979.
- [108] W.-S. Liao, C.-H. Lin, and S.-C. Lee, “Oxidation of silicon nitride prepared by plasma-enhanced chemical vapor deposition at low temperature,” *Applied Physics Letters*, vol. 65, pp. 2229–2231, oct 1994.

- [109] B. Walmsley, Y. Liu, X. Hu, M. Bush, K. Winchester, M. Martyniuk, J. Dell, and L. Faraone, “Effects of deposition temperature on the mechanical and physical properties of silicon nitride thin films,” *Journal of applied physics*, vol. 98, no. 4, p. 044904, 2005.
- [110] L. Gong, Y. Wang, X. Cheng, R. Zhang, and H. Zhang, “A novel effective medium theory for modelling the thermal conductivity of porous materials,” *International Journal of Heat and Mass Transfer*, vol. 68, pp. 295–298, jan 2014.
- [111] N. Jehanathan, M. Saunders, Y. Liu, and J. M. Dell, “Crystallization and compositional changes in amorphous PECVD SiN<sub>x</sub> thin films,” in *International Conference on Smart Materials and Nanotechnology in Engineering*, SPIE, jul 2007.
- [112] S. Jafari, J. Hirsch, D. Lausch, M. John, N. Bernhard, and S. Meyer, “Composition limited hydrogen effusion rate of a-sinx: H passivation stack,” in *AIP Conference Proceedings*, vol. 2147, p. 050004, AIP Publishing LLC, 2019.
- [113] J. L. Niedziela, D. Bansal, A. F. May, J. Ding, T. Lanigan-Atkins, G. Ehlers, D. L. Abernathy, A. Said, and O. Delaire, “Selective breakdown of phonon quasiparticles across superionic transition in CuCrSe<sub>2</sub>,” *Nature Physics*, vol. 15, pp. 73–78, oct 2018.
- [114] R. G. Ross, “Thermal conductivity and disorder in nonmetallic materials,” *Physics and Chemistry of Liquids*, vol. 23, no. 4, pp. 189–210, 1991.
- [115] V. Murashov and M. A. White, “Thermal conductivity of insulators and glasses,” in *Thermal Conductivity*, pp. 93–104, Springer, 2004.
- [116] C. H. Mastrangelo, Y.-C. Tai, and R. S. Muller, “Thermophysical properties of low-residual stress, silicon-rich, lpcvd silicon nitride films,” *Sensors and Actuators A: Physical*, vol. 23, no. 1-3, pp. 856–860, 1990.
- [117] H. Ftouni, C. Blanc, D. Tainoff, A. D. Fefferman, M. Defoort, K. J. Lulla, J. Richard, E. Collin, and O. Bourgeois, “Thermal conductivity of silicon nitride membranes is not sensitive to stress,” *Physical Review B*, vol. 92, no. 12, p. 125439, 2015.
- [118] A. Milloch, R. Mincigrucci, F. Capotondi, D. De Angelis, L. Foglia, G. Kurdi, D. Naumenko, E. Pedersoli, J. S. Pelli-Cresi, A. Simoncig, *et al.*, “Nanoscale thermoelasticity in silicon nitride membranes: Implications for thermal management,” *ACS Applied Nano Materials*, vol. 4, no. 10, pp. 10519–10527, 2021.

- [119] G. Monaco and V. M. Giordano, “Breakdown of the debye approximation for the acoustic modes with nanometric wavelengths in glasses,” *Proceedings of the national Academy of Sciences*, vol. 106, no. 10, pp. 3659–3663, 2009.
- [120] Y. Wan, K. R. McIntosh, and A. F. Thomson, “Characterisation and optimisation of pecvd sinx as an antireflection coating and passivation layer for silicon solar cells,” *AIP Advances*, vol. 3, no. 3, p. 032113, 2013.